Radio-frequency discharge power measurement with emphasis on collisionless electron heating in capacitive sheaths

D. Gahan

August 2, 2006

RADIO-FREQUENCY DISCHARGE POWER MEASUREMENT WITH EMPHASIS ON COLLISIONLESS ELECTRON HEATING IN CAPACITIVE SHEATHS

A thesis for the degree of

PHILOSOPHIAE DOCTOR

Presented to

DUBLIN CITY UNIVERSITY

By

David Gahan
School of Physical Sciences
Dublin City University

Research Supervisors:
Dr. Mike B. Hopkins and
Prof. Miles M. Turner

External Examiner: Dr. Mark D. Bowden
Internal Examiner: Dr. Paul Swift

June 2006

Declaration

I hereby certify that this material which I now submit for assessment on the programme of study leading to the award of Philosophiae Doctor is entirely my own work and has not been taken from the work of others save and to the extent that such work has been cited and acknowledged within the text of this work.

David Gahan, 19th June 2006

Abstract

Many of today's processing plasma tools are operated at low pressures to achieve high etch directivity and reduce side erosion on the wafer. At these pressures electron-neutral collisions are rare and the electrons cannot gain energy through the Ohmic heating process. Instead the heating mechanism is attributed to a stochastic process between the electrons and the sheath electric field. Theoretical models of this stochastic process include the hard wall approximation and the pressure heating effect. The former is inconsistent with electron current conservation at the sheath whilst the later shows a difference in power absorption when electron loss to the electrodes is considered.

This thesis examines the effects of electron current on power coupling in a capacitive sheath by controlling this current with an additional DC bias applied to an rf biased electrode. Experimental and particle-in-cell model results for a low pressure argon plasma are compared and presented. Results show that the electron power absorption is more effective when the electron conduction current is removed, as predicted by the earlier theoretical work.

The model also shows a high harmonic content on the sheath voltage which is attenuated by removing the electron current. These high frequency harmonics are measured in the experiment, with an unbiased probe connected to a spectrum analyzer, and their correlation with the electron current is in agreement with the model results. It is found that the high frequency oscillations do not contribute to the power absorption in an average sense.

Finally a novel rf power sensor is presented and compared with an industrial standard power meter. The design incorporates directional coupler and

I-V probe techniques to determine the power. This sensor is found to out perform the standard meter over a wide range of conditions. Its ability to measure the power at the fundamental as well as harmonic frequencies makes it a particularly useful plasma diagnostic.

Acknowledgements

Foremost, I would like to thank my supervisor Dr. Mike Hopkins, without whose help, encouragement and vision this research would never have reached this stage. For that I will always be grateful.

I would like to thank Dr. Bert Ellingboe and Professor Miles Turner for the conception of this project and for their guidance in the early stages of my research and for always being available to discuss results and ideas. I would especially like to thank Dr. Felipe Sobéron for providing the PIC model results used throughout this thesis.

I have also benefited greatly from many discussions with my fellow students Derek, Angus, Shane, Chanel, Peter, Taghrid, Niall, Cezar and Muhammad. Others who have contributed in different ways to my PhD success include Samantha, Sarah, Des, Paul, Vic, Stuart, Ronan, Jim, Lutfi, and Shantanu. Thanks also to students and staff, past and present, who I haven't mentioned, that have made my research experience such an enjoyable one.

My final acknowledgements must go to my family. Their constant support

and encouragement has helped in ways that I probably don't even realise.

Contents

1 Introduction **16**

1.1 Radio-frequency (rf) discharges 18

1.1.1 Capacitive rf discharges 18

1.1.2 Inductive rf discharges 19

1.2 The capacitive rf sheath 21

1.3 Collisionless electron heating 22

1.4 Experimental evidence of collisionless heating 24

1.5 Simulations 28

1.6 Research goals and thesis outline 30

2 Experimental setup and electrical diagnostics **33**

2.1 Reactor geometry 34

2.2 RF power coupling 34

2.3 Vacuum system 36

2.4 Radio-frequency biassed electrode 37

2.4.1 RF bias circuit 37
2.4.2 DC bias circuit 40
2.5 Current and voltage probes 41
2.5.1 Probe propagation delays 41
2.5.2 Characterization of parasitic impedance 42
2.6 Electrostatic probes 46
2.6.1 Wire loop probe 46
2.6.2 Langmuir and 50Ω probes 47
2.7 Summary 48

3 Collisionless heating and a test of the pressure heating formulation 50

3.1 Fermi acceleration 50
3.2 Fermi acceleration applied to capacitive discharges 51
3.3 Collisionless heating through Fermi acceleration 52
3.3.1 Liebermans calculation 52
3.3.2 Revised calculation 54
3.4 Pressure heating 55
3.4.1 The pressure heating equation 56
3.4.2 Approximate solution 58
3.4.3 Power deposition for a specified sheath density profile . 59
3.5 Experimental test of the pressure heating model 62
3.6 Electrical Measurements 64
3.6.1 Current and voltage waveforms 64
3.6.2 Bias voltage distribution 68
3.6.3 Instantaneous power absorption 71
3.6.4 Average power absorption 73
3.7 Summary 79

4 Electrical analysis of the sheath: A comparison with PIC simulations 81
4.1 Introduction . . . 81
4.2 The particle-in-cell model . . . 82
4.3 Cycle averaged ion and electron conduction currents . . . 84
4.4 Phase resolved electron conduction current . . . 86
4.5 Power absorption . . . 89
4.6 High frequency sheath potential oscillations . . . 93
4.7 Summary . . . 96

5 A novel wide-band rf power sensor 102
5.1 Plasma discharge power measurement . . . 102
5.2 Standard directional power meter . . . 103
5.3 Associated errors . . . 106
5.3.1 Error due to directivity . . . 106
5.3.2 Error due to test port mismatch . . . 107
5.4 A new design . . . 107
5.4.1 Mechanical design . . . 107
5.4.2 Theory of operation . . . 109
5.5 Sensor calibration . . . 110
5.5.1 Propagation delay . . . 110
5.5.2 Signal amplitude scaling . . . 114
5.6 Sensor accuracy . . . 116
5.7 Comparison with standard wattmeter . . . 118
5.8 Summary . . . 120

6 Conclusion 122
6.1 The experimental technique . . . 123

6.2 Collisionless electron power absorption 124
6.3 Discharge power measurement 126

List of Figures

1.1 Schematic of a typical capacitive discharge. 18

1.2 Schematic of an inductively coupled plasma discharge. 20

1.3 Effective collision frequency versus pressure for a mercury discharge driven at 40.8 MHz. The solid line is the collision frequency due to Ohmic heating alone (after [1]) 24

1.4 The ratio between total and collisional rf power transferred to the bulk plasma electrons versus argon pressure (after [2]) . . 25

1.5 Evolution of the electron probability function (EEPF) $g_p(\varepsilon)$ with pressure in argon (after [2]) 27

2.1 Schematic of the ARIS device showing source and diffusion regions. 35

2.2 Schematic of the biassed electrode system, showing both the rf power coupling circuit and the additional dc biassing circuit. 38

2.3 Equivalent circuit model of the electrode system and bias circuitry. C_{block} and C_{shunt} are blocking and shunt capacitors respectively. $C_{electrode}$ is the electrode capacitance to ground and L_{filter} blocks rf current reaching the dc supply. I_s and I_p are the stray and plasma rf current respectively and I_{dc} is the dc current drawn by the dc supply. 39
2.4 The equivalent circuit as seen by the rf generator. 39
2.5 The equivalent circuit as seen by the dc bias supply. 41
2.6 Voltage and current probe phase errors 43
2.7 Schematic of the wire loop probe construction showing the 50 Ω vacuum feed-through. 46

3.1 Comparison between the instantaneous power, calculated at various times in the rf cycle, from the PIC simulation (solid line) and from the analytic model (dashed line). The analytic solution uses the density profile obtained from the PIC simulation (after [3]). 61
3.2 Schematic of experimental apparatus showing the inductive source, the biased electrode and the electrical probe diagnostics. L_1 and C are used to step up the electrode voltage. C also ensures capacitive coupling of the rf supply. L_2 blocks rf signals from reaching the dc source and R is a 10Ω resistor used for sensing the net DC current. 63
3.3 Typical electrode voltage waveform and its frequency spectrum. 65
3.4 Typical plasma current waveform and its frequency spectrum. 66

3.5 Equivalent circuit model of the discharge. Z_{ps} and Z_{gs} are the power sheath and ground sheath impedances respectively with the accompanying voltage drops V_{ps} and V_{gs}. R_p is the plasma bulk resistance, V_p the plasma potential measured with the wire loop probe, and V_e the applied electrode voltage. 68

3.6 Plasma potential waveform along with its frequency spectrum. Plasma conditions as described in the text. 70

3.7 Instantaneous power signal obtained from the product of the current and voltage waveforms in figure 3. 72

3.8 A schematic of the sheath structure showing the ion density (solid) along with the electron density (dashed) at one time (s(t)) in the rf cycle. 0 is the ion sheath edge and s_m is at the electrode - the maximum sheath width. 74

3.9 Langmuir probe measurements taken ≈ 10 cm from the electrode. The electron density, electron temperature, plasma potential and floating potential remain approximately constant as a function of DC bias applied to the electrode. The vertical dashed line denotes the electrode self bias. 75

3.10 The absolute value of dc current to the electrode as a function of dc bias imposed on the electrode for an inductive source power of 500W, with no rf bias applied. 76

3.11 Average power absorbed as a function of increasing negative dc bias. The first point on the graph corresponds to the self biased situation. Triangles represent the total power, while square and circle represent the ion and electron power respectively. 78

3.12 Comparison of the current waveform at self bias (solid) with the current signal at the last point on figure 9 (dashed). A scaled down image of the electrode voltage is superimposed (dot) in the background to highlight the electron collection phase of the rf cycle. 79

4.1 Electron (absolute value) and ion cycle average current density (A/m^2) as a function of DC bias. 85

4.2 Current waveform for the self biased case (solid), large negative bias case (large dash) and the approximate self biased electron current (small dash). 87

4.3 Electron and displacement current density (A/m^2) at the electrode for a self biased electrode (a) and a negatively biased electrode (b); profiles shown over two periods. 88

4.4 Electron conduction current waveforms as a function of DC bias from a) the experiment and b) the PIC simulation. 90

4.5 a) Total power dissipated in the sheath (triangle) as a function of DC bias, separated into the ion power (diamond) and the total electron power (square). b) Cycle average power absorption (kW/m^2) associated with the electron, ion, displacement and total current as a function of DC bias. 91

4.6 Voltage amplitude of harmonics of the space potential in the sheath as a function of DC bias from a) the experiment and b) the simulation. Filled triangle, diamond, box and star corresponding to second, third, fourth and fifth harmonics respectively and unfilled triangle, diamond, box and star corresponding to sixth, seventh, eight and ninth harmonics respectively. . 94

4.7 Electron density (a) and space potential (b) for a self biased electrode; profiles shown over two periods. 99

4.8 Electron density (a) and space potential (b) for a negatively biased electrode; profiles shown over two periods. 100

4.9 $J \cdot E$ product density plot for a self biased electrode (a) and for a negatively biased electrode (b); profiles shown over two periods. Dark areas denote power absorption by the electrons, light areas denote power loss. 101

5.1 Schematic of a standard power meter structure with its equivalent sensing circuit. 104

5.2 Schematic of sensor construction. The rf connectors are female N-type and the output connectors are female SMA. 108

5.3 The sensing elements' equivalent circuit showing the opposite orientation of the two mutual inductances (loops). 109

5.4 Setup for phase calibration showing the use of the "dummy line" to find the phase at the sensing element location 111

5.5 Reference voltage probe phase calibration 112

5.6 Phase errors associated with sensor cabling and oscilloscope input impedance. Circles represent the measured data while the dashed line is a 6_{th} order polynomial fit. 113

5.7 Sensor output signals as a function of frequency. Circles and triangles represent measured data, while dashed lines represent 4th polynomial fits to the data. 115

5.8 Normalized frequency response of our sensor compared to an industrial standard wattmeter, over the frequency range specified for the wattmeter. 118

5.9 Comparison of load SWR measurements for a fixed dummy load of 50 Ω in parallel with a 376 pF capacitor for varying frequency 119

List of symbols

A	area (m^{-2})
d	distance (m)
D	diffusion coefficient (m^2s^{-1}); D_a ambipolar diffusion coefficient; drift energy flux (Wm^{-2})
e	absolute electron charge ($\simeq 1.6 \times 10^{19}$ C)
E	electric field (Vm^{-1}); energy (J or eV)
f	frequency (Hz); distribution function ($m^{-2}s$)
H	magnetic field strength (Am^{-1})
I	current (A)
j	$(-1)^{1/2}$
J	current density (Am^{-2})
k	Boltzmann's constant ($\simeq 1.381 \times 10^{-23}$ JK^{-1})
l	length (m)

continued on next page

continued from previous page

m	mass (kg); m_e electron mass ($\simeq 9.1 \times 10^{-31}$ kg); m_i ion mass
n	particle number density (m^{-3}); n_e electron density; n_i ion density; n_g neutral gas density
P	power (W)
p	pressure (Torr)
q	electric charge (C)
Q	heat flux (Wm^{-2})
s	sheath position (m)
S	energy flux (Wm^{-2})
t	time (s)
T	temperature (K or Volts)
u	velocity (ms^{-1}); average velocity; u_B Bohm velocity
v	velocity (ms^{-1})
V	electric potential (V)
$\mathcal{W}$	super-particle weighting factor
x	rectangular coordinate
Γ	particle flux ($\mathrm{m}^{-2}\mathrm{s}^{-1}$)
δ	Dirac delta function; small quantity
Δ	Δt PIC timestep; Δx PIC cell size
ϵ_0	vacuum permittivity ($\simeq 8.8 \times 10^{-12}$ Fm^{-1})
ζ	small displacement (m)
η	normalized potential
θ	angle (rad)
λ	mean free path (m); λ_i ion mean free path; λ_D electron Debye length (m)

continued on next page

continued from previous page

μ_0	permeability of free space ($4\pi \times 10^{-7}$Hm^{-1})
ν	collision frequency (Hz)
ρ	charge density (Cm^{-3})
σ	cross section (m^{-2}); electrical conductivity (Ω^{-1}m^{-1})
τ	normalized temperature
ϕ	angle (rad)
Φ	potential (V)
ω	angular frequency (rad s^{-1}); ω_{pe} electron plasma frequency; ω_{pi} ion plasma frequency

CHAPTER 1

Introduction

Recent decades have seen rapid advancement in plasma processing technology [4, 5], which impacts and is vitally important to several of the largest manufacturing industries in the world. At the forefront is the electronics industry, where plasma based processes are essential to the production of microelectronic integrated circuits. Other industries which rely heavily on the plasma processing of materials include aerospace, automotive, steel manufacturing, biomedical engineering, and industrial waste management. Plasma research is directed towards understanding the fundamental mechanisms involved in such processes, to enhance our ability to use plasmas efficiently.

The aim of this research is to investigate phenomena associated with the most important regions of capacitively coupled, radio-frequency (rf) driven plasmas - the rf sheaths. The sheaths are important in any type of discharge as they form the boundary between the plasma and any surface in contact

with it. In capacitive discharges the sheath is especially interesting as it is in this region that electrons gain sufficient energy to sustain the plasma at low pressures.

The sheath is also the region in which most of the electric fields exist in a capacitive plasma. This electric field points from the plasma to the electrode, accelerating ions towards the electrode (or any material placed on the electrode for processing) while confining electrons in the bulk. The recent trend has been to operate capacitive discharges at low pressures where the ion mean free path becomes large compared to the sheath dimensions. The lack of ion collisions in the sheath allows better control over the ion energy reaching the surface. At these low operating pressures electron collisions in the bulk also become rare. Electron energy gain through the normal Ohmic heating mechanism is no longer capable of sustaining the discharge. However, there is an effective stochastic or collisionless heating mechanism that imparts energy to the electrons, thus maintaining the discharge. Exactly how electrons gain energy through this collisionless heating mechanism has been discussed since the 70's [6, 7] and is still an on going topic of debate. As yet a globally accepted model that accurately describes the phenomenon has not been given.

The goal of this research is to experimentally investigate one of the most resent theories [8] put forward to describe collisionless electron heating. The main objective is to confirm certain predictions of this model to verify its correctness. A new experimental system is presented which allows this investigation. The advantage of this system is that conditions can be imposed on the capacitive sheath that have not been investigated previously.

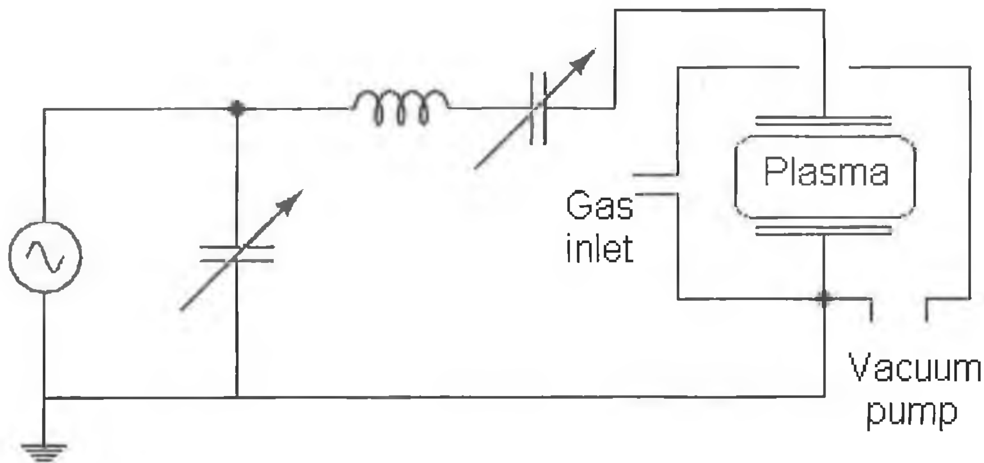

Figure 1.1: *Schematic of a typical capacitive discharge.*

1.1 Radio-frequency (rf) discharges

The most commonly used frequency of excitation in processing plasmas is 13.56 MHz. This frequency and its harmonics have been allotted by international communications authorities to avoid interference with existing communication systems. At these frequencies the electrons are able to respond to the oscillating electric field but the ions, being much heavier, respond only to a time averaged electric field.

1.1.1 Capacitive rf discharges

Laboratory plasmas are formed by confining a volume of gas in a chamber and feeding electrical energy to it. In a capacitive discharge [9] an rf voltage/current is applied between two electrodes (one of which is usually grounded) mounted in a vacuum chamber, which subsequently causes a current to flow through the neutral gas. The neutral gas atoms get excited and ionized by the electrons accelerated in the electric fields. This ionized state of

the gas is termed a plasma. The rf power that sustains the plasma is coupled through a matching unit which maximizes the power transfered from source to discharge. In figure 1.1 a typical capacitive discharge is shown. Many different gases are used to supply the ions, ranging from the noble gases like Argon and Helium to complex mixtures, depending on the application. Operating pressures range from milliTorr to Torr and electrode voltages range from hundreds to thousands of volts. Charge particle densities in the plasma are of the order of $10^{14} - 10^{17}$ m^{-3}. One of the main features of the capacitive rf discharge is the absence of thermal equilibrium between the particles. Ions are generally assumed to be at room temperature while the electrons can have temperatures ranging from 1-5 eV which they gain from interaction with the sheath electric fields. The temperature difference arises because the electrons are confined in the plasma by the sheaths, and at the same time they don't loose energy in elastic collisions as energy transfer is proportional to the mass ratio of the colliding species.

1.1.2 Inductive rf discharges

The inductively coupled rf discharge [7] uses a different method of coupling rf power to the plasma. Instead of electrodes in direct contact with the plasma, an induction coil couples the power through a dielectric window. A schematic of the configuration used in this work is given in figure 1.2. The oscillating rf current in the antenna has an associated oscillating magnetic field which penetrates the dielectric window to the plasma. This oscillating magnetic field induces an electric field in the plasma by Faraday's law

$$\nabla \times E = -\mu_0 \frac{\partial H}{\partial t} \qquad (1.1)$$

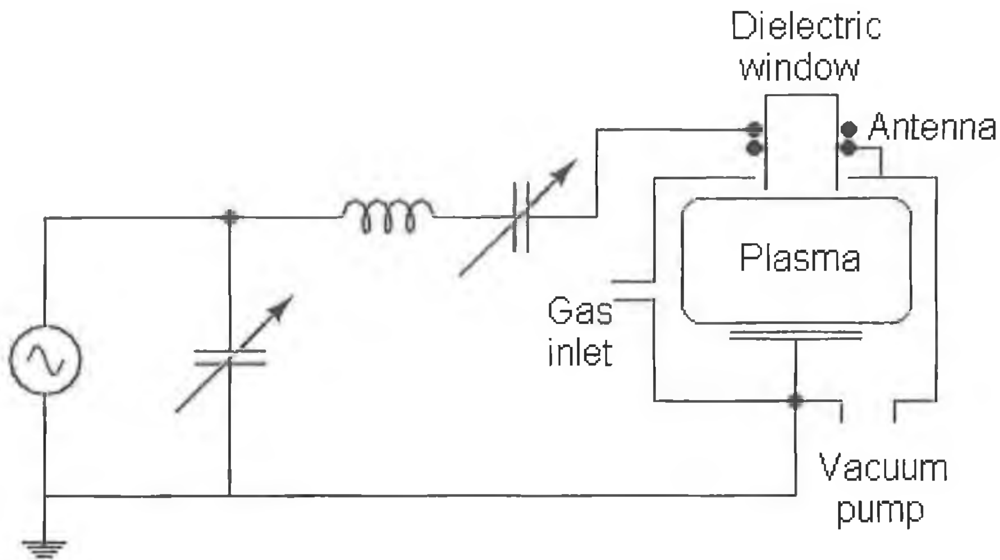

Figure 1.2: *Schematic of an inductively coupled plasma discharge.*

where μ_0 is the permeability of free space, and E and H are the electric and magnetic field vectors respectively.

At low densities the antenna behaves as an electrode. The discharge is initially triggered in capacitive mode due to the high antenna voltage. When the plasma density reaches a sufficient level the power coupling switches to the inductive mode. Inductive discharges have the advantage that higher plasma densities can be achieved at lower pressure compared to capacitive discharges.

An electrode is usually introduced into the inductive system for processing applications. The electrode is generally biassed with an rf voltage to control the ion energy reaching the substrate. This provides a means of independently controlling the ion flux (controlled by the inductive source) and the ion impact energy (controlled by the biassed electrode sheath), which is a fundamental limitation of capacitively coupled systems. This idea has been

implemented in this work, not to control ion energy to a substrate, but to investigate power coupling through the single capacitive rf sheath associated with the biassed electrode.

1.2 The capacitive rf sheath

The sheath forms the interface between the plasma and the electrodes in a capacitive electropositive discharge. In this region a high intensity electric field exists and points from the plasma to the electrode. To understand how a sheath is formed we consider what happens when a grounded conducting surface is exposed to a plasma. Due to the higher thermal velocity of the electrons a negative charge initially builds up at the surface. This leads to a breaking of quasi-neutrality in the vicinity of the surface with an excess positive charge. An electric field is now formed pointing from the plasma to the surface confining electrons in the plasma and accelerating ions to the surface. The sheath region continues to grow until equilibrium is reached and the electron and ion fluxes are balanced.

The sheath motion becomes complicated in our situation since the electrode is driven with an rf voltage. The sheath front is not static but oscillates in time. A schematic of the rf sheath structure is given in figure 3.8 which has been used in many theoretical investigations of the sheath dynamics [3, 10, 11]. The ions respond only to the time averaged electric field while the electrons oscillate back and forth following the motion of the sheath edge. The ion density profile is represented by the solid line which drops as shown, from the ion sheath edge at 0 to the electrode at s_m. This decay is caused by the ions being accelerated in the sheath electric field. The electrons being much lighter than the ions are able to follow the oscillating electric field.

The electron density profile follows the ion density profile, to preserve quasi-neutrality, from 0 to the instantaneous sheath edge $s(t)$ (shown for one point in the rf cycle) represented by the dashed line. The electron density quickly drops to zero at the electrode side of the instantaneous sheath edge. A complete mathematical description of the rf sheath is given by Lieberman in reference [10].

1.3 Collisionless electron heating

In order to sustain a plasma discharge it is necessary to have electrons with sufficient energy to ionize the neutral gas atoms. Two types of heating can be identified depending largely on the operating pressure of the discharge.

At high pressure where the electron mean free path is small compared to the discharge dimensions the electrons gain their energy through momentum transfer with the heavy neutral atoms. This process is well understood [4] and the time averaged power per unit area, P_{Ohm}, deposited in the plasma is

$$P_{Ohm} = \frac{1}{2}\bar{J}^2 Re(\sigma_p^{-1}), \tag{1.2}$$

where $\bar{J}$ is the current density, $\sigma_p = \epsilon_0\omega_{pe}^2/(j\omega + \nu_m)$ is the plasma conductivity, ω is the driving frequency, ν_m is the collision frequency for momentum transfer, ω_{pe} is the electron plasma frequency and ϵ_0 is the permittivity of free space.

At low pressure when the electron mean free path becomes greater than the discharge dimensions power can not be transferred through collisions. However an effective collisionless heating mechanism does exist whereby electrons gain energy through interaction with the electric fields in the sheath region. This collisionless heating phenomenon has been an active area of

research for more than 50 years but as yet a globally accepted model of the interaction between plasma electrons and rf sheath that gives rise to collisionless heating has not been established. In the early literature [12–14] the phenomenon of collisionless heating was described by the Fermi acceleration [15] mechanism. Electrons traveling from the bulk plasma collide with the moving sheath edge and gain or loose energy depending on whether the sheaths motion is towards or opposite to that of the electrons. This collision is assumed to be elastic such that

$$u_r = -u_i + 2u_s \tag{1.3}$$

where u_i is the incident velocity of an electron, u_s is the velocity of the sheath front at the time of the collision and u_r is the velocity of the electron after reflection. Because head on collisions are more probable a net energy gain is expected. In recent years the validity of the Fermi acceleration mechanism as applied to capacitive discharges has been called into question.

Another mechanism, initially proposed by Surrendra and Graves [16], is described as a pressure heating effect caused by the constant compression and rarefaction of the electron population in the sheath vicinity, as the sheath electric field expands and contracts. This idea was developed [8, 17] using computer simulations and in the later almost perfect agreement has been found between particle-in-cell (PIC) simulations and an analytical solution of the pressure heating equation. Although certain assumptions have been called into question concerning this analytical solution [18], it does show that the loss of electrons at the end of the rf cycle is an important effect that must be considered in any model attempting to describe the collisionless heating mechanism.

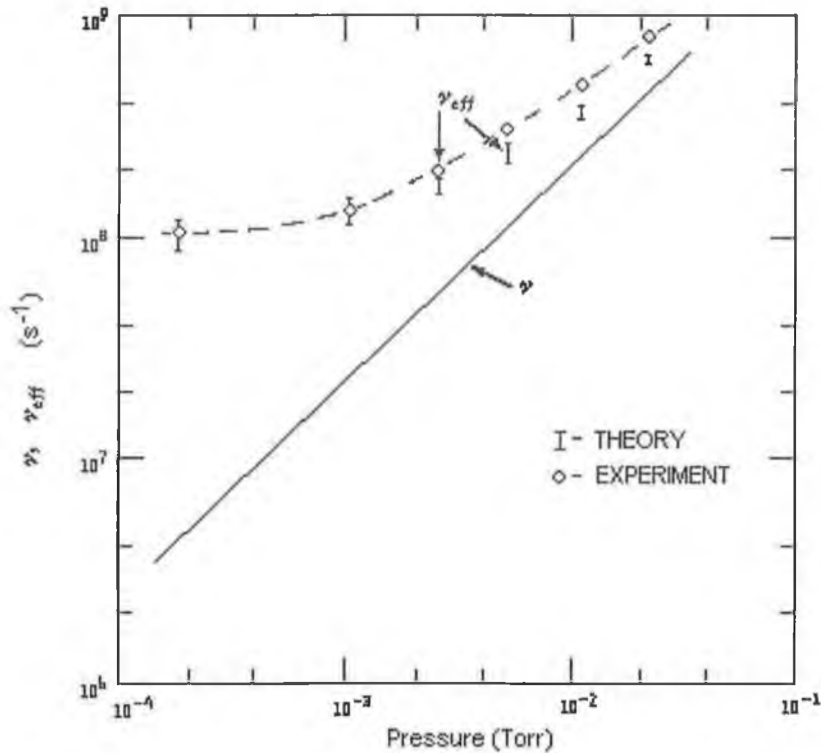

Figure 1.3: *Effective collision frequency versus pressure for a mercury discharge driven at 40.8 MHz. The solid line is the collision frequency due to Ohmic heating alone (after [1])*

1.4 Experimental evidence of collisionless heating

To date their has been very little experimental investigation of the collisionless heating phenomenon. The experimental work that has been carried out has mostly been to show that the phenomenon exists and under what conditions it is dominant over the Ohmic heating, rather than to elucidate the exact mechanism by which it operates. Most of the experimental work on collisionless heating reported has been by Godyak and co-workers. The early

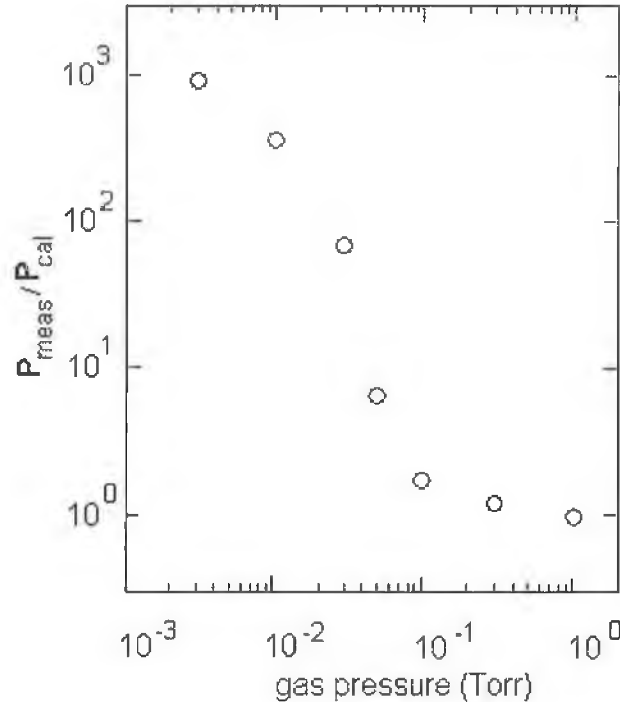

Figure 1.4: *The ratio between total and collisional rf power transferred to the bulk plasma electrons versus argon pressure (after [2])*

experiments [1, 13, 14, 19] were performed in a parallel plate capacitive rf discharge symmetrically driven at 40 – 110 MHz in mercury vapor. Electrical measurement of the current-voltage characteristics and rf power, as well as measurement of the plasma density and electron temperature were taken simultaneously at pressures ranging from 2×10^{-4} to 1×10^{-1} Torr. The effective collision frequency, ν_{eff}, was calculated [1] from the power absorbed per unit area

$$P_{abs} = \frac{1}{2}\frac{|\tilde{J}_{rf}|^2}{e^2 n} m\nu_{eff} l \tag{1.4}$$

where $|\tilde{J}_{rf}|$ is the discharge current density, e is the electronic charge, n the electron density, m the electron mass and l is the length of the discharge. The

effective collision frequency, obtained from the experiment, as a function of mercury pressure is shown in figure 1.3. If only Ohmic heating were present then ν_{eff} would follow the solid line. At lower pressures in the experiments an asymptotic leveling of ν_{eff} is indicative of stochastic heating. It has been noted [7] however that the good agreement between theory and experiment in figure 1.3 is somewhat fortuitous since uniform sheath has been used in the theoretical calculation while the power absorbed by the ions in the sheath has been neglected in the measurements.

Later experimental work by Godyak and co-workers [2, 20, 21] is concentrated on the study of symmetrically driven rf discharges in argon gas at 13.56 MHz. The discharge had a length of 6.7 cm and a diameter of 14.3 cm and approximated a plane parallel configuration. Measurements were made of the various electrical and plasma parameters. The ion power absorbed in the sheaths was also accounted for in these measurements. The Ohmic power dissipation was calculated from (1.4). A plot of the ratio of total electron power dissipated (P_{meas}) to ohmic power dissipated (P_{cal}) as a function of pressure is given in figure 1.4. The total electron power dissipated is calculated as the difference between the total power dissipated and the power absorbed by the ions. At high pressure the ratio is almost unity illustrating the dominance of the Ohmic heating process. At the lowest pressure the ratio increases by nearly three orders of magnitude and is attributed to the stochastic heating which sustains the discharge in the absence of collisions. The evolution of this heating mode transition is shown in figure 1.5. The electron energy probability function (EEPF [1]) $g_p(\varepsilon)$ is plotted for various argon pressures. At high pressure the distribution is Druyvesteyn-like, typical

[1] The EEPF is defined such that a plot of $\ln g_p$ versus ε is a straight line for a Maxwellian distribution.

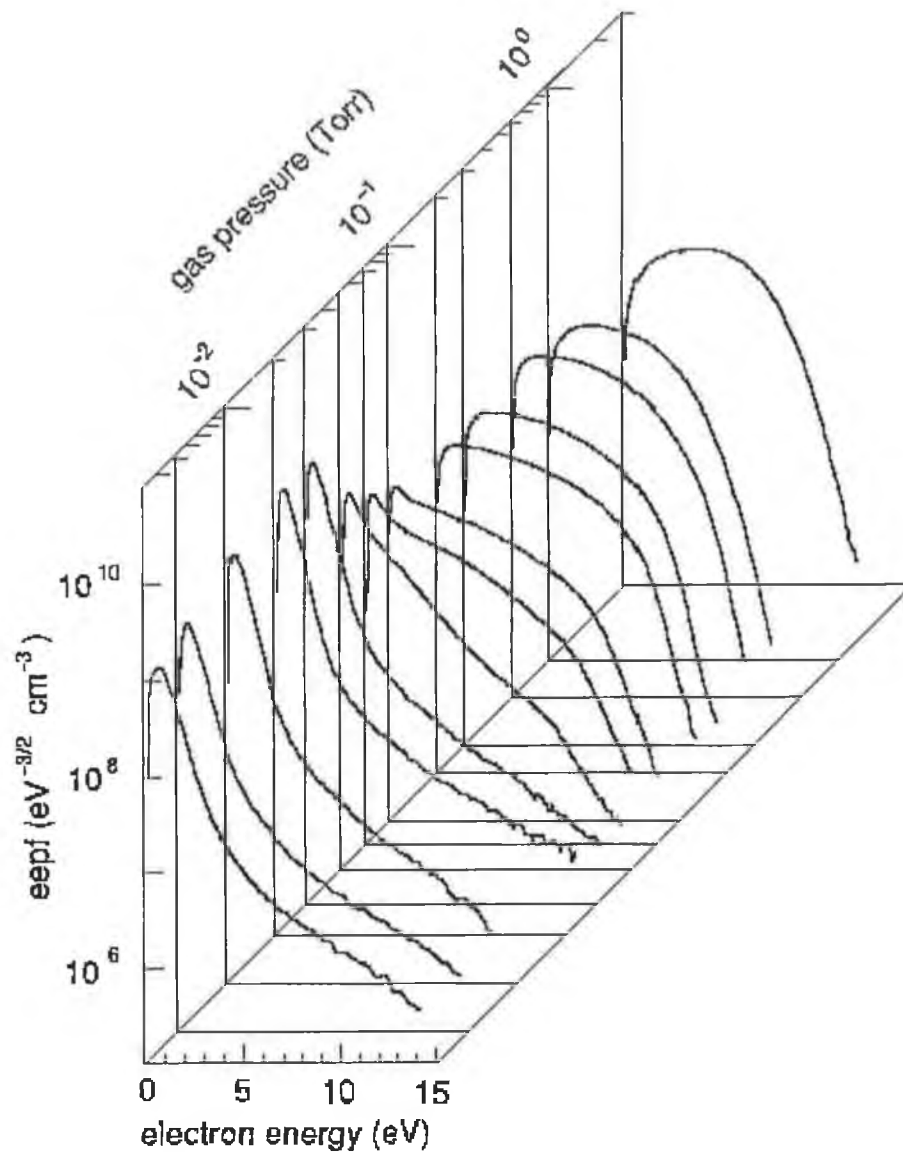

Figure 1.5: *Evolution of the electron probability function (EEPF) $g_p(\varepsilon)$ with pressure in argon (after [2])*

of collisional argon discharges. At low pressure the distribution switches to a bi-Maxwellian where stochastic heating dominates. The majority of the electrons are characterized by a low temperature Maxwellian distribution. They are confined in the bulk plasma and do not have sufficient energy to reach the oscillating sheaths to gain energy stochastically. The higher energy electrons interact with the sheaths, effectively bouncing back and forth between them, gaining energy in the process. This group of electrons constitute the second Maxwellian distribution with higher energy.

1.5 Simulations

Monte Carlo and PIC simulations [22] of low pressure capacitive discharges also confirm the existence of collisionless electron heating in the oscillating sheaths [11, 23–28]. The collisionless heating in [23] was found to be due to electron reflection from the oscillating sheath edge. In the same work EEPF's with high energy tails were found and attributed to collisionless heating. Low pressure fluid simulations have also been performed [29] using a helium-like model gas, the results of which are compared with PIC simulations of the same system. The main difference being that the fluid model does not contain the collisionless heating physics. The fluid model subsequently underestimates the electron power absorption relative to the PIC result.

Vahedi and co-workers [30] have made comparisons with the experimental work of Godyak and Piejak [21] using PIC simulations. A similar transition in the shape of the EEPF from Druyvesteynian (at higher pressure) to bi-Maxwellian (at lower pressure) was observed. Surrendra and Dalvie [31] obtain results using a PIC simulation that suggest that electron heating could be separated into two terms - Ohmic heating and pressure heating respec-

tively. The later being essentially the collisionless heating term. Vender and Boswell [32] use a PIC simulation to show that the intensity of ionization is greater near the sheath when it expands compared to when it collapses, following the presence of hot electrons. They also highlight the importance of electron inertia, power loss to the electrodes and the lack of self-consistency associated with models of the electron-sheath interaction. Detailed comparisons with the experimental results of Godyak using various simulation techniques has been performed by Surendra [33]. Monte-Carlo simulations using a analytic expression for the electric field with which the electrons interact have also been performed [23, 26], enabling the calculation of collisionless power transferred to the electrons.

One of the most interesting developments on the collisionless electron heating phenomenon was the transition from the Fermi mechanism explanation to the pressure heating one. Initially, using a full capacitive discharge PIC simulation, Surendra [34] suggests that heating could be due to electron acoustic waves driven by the pressure gradient between the sheath and plasma bulk. In a later paper [31] it was found that pressure terms, calculated from a self-consistent[2] PIC simulation, could account for almost all of the observed power deposition. Turner [17] went on to show, using a PIC simulation without electric fields, that the heating was not much diminished from a PIC simulation with electric fields present. This implied that the oscillating sheath edge was not crucial to the heating mechanism. He proposed that the electron population in the sheath vicinity was heated and cooled as the sheaths expand and contract with net heating expected - so called pressure heating.

[2]In the present context the term "self-consistent" means that the solution of the electric field and particle motion is done simultaneously.

The most recent attempt to obtain a valid analytic solution for the pressure heating mechanism was by Gozadinos [3, 8]. To make comparisons with this analytic solution a PIC simulation of only the plasma sheath was used. This technique models a single electrode, at one side of the simulation area, in contact with an infinite bulk plasma on the other side. This method allows the sheath region to be analyzed in more detail compared to the standard PIC implementation at the same computational cost. The subsequent comparisons of the collisionless heating between PIC and model show exceptionally good agreement, both in a time average sense as well as the phase resolved case.

1.6 Research goals and thesis outline

The motivation for the work presented in this thesis is to achieve better understanding of the collisionless heating mechanism that sustains capacitive rf discharges at low pressure. The primary aim being to develop an experimental technique to enable testing of collisionless heating theory and in general to characterize the capacitive rf sheath in terms of electrical measurements.

In chapter 2 the entire experimental system is described in detail. The rf, dc biased electrode technique used throughout this research is introduced. The method is based on a large volume plasma in contact with a planar electrode similar to particle-in-cell simulations based on the same principles. The plasma is sustained separately so that the rf sheath at the electrode is decoupled from the plasma parameters. Thus the electrode sheath conditions can be altered without influencing the plasma bulk so that only the effect of the imposed conditions are measured. This would not be possible if measurements were made at the electrode of a standard parallel plate reactor.

In chapter 3 a detailed electrical examination of the electrode sheath is presented. The voltage across and the current through the capacitive sheath are determined using a in-depth probe calibration procedure. A reliable calculation of the power absorbed is thus obtained. One prediction of a previous theoretical model is that electron loss to the electrode has a significant bearing on the power absorption measurement. This idea is tested using an external dc bias to repel previously escaping electrons back to the plasma hence removing the contribution of electron loss from the power measurement. The finding is that the removal of electron loss to the electrode is indeed accompanied with a significant change in the power absorbed, in agreement with the theoretical model mentioned. The current waveforms are examined with and without external bias and the only significant difference is isolated at the electron loss phase of the rf cycle, validating our result.

In chapter 4 a method to extract the electron conduction current is given. A detailed comparison of the electrical measurement and the PIC measurements is made. Excellent qualitative agreement is found in terms of current and voltage measurements and the power absorbed by both the ions and electrons in the sheath. The PIC separates the collisionless power from the electron loss power as a function of applied dc bias. It is found that the collisionless component remains constant while the electron loss component decreases confirming the experimental results. High frequency oscillations in the sheath potential are monitored (as a function of dc bias) with a 50Ω probe and spectrum analyzer. These oscillations are also investigated using the PIC. The amplitude of these oscillations decrease, in both experiment and model, with increasing bias. The power absorbed however remains constant indicating that these oscillations do not contribute to the overall power dissipation.

In chapter 5 an in-line sensor with 50Ω characteristic impedance to accurately measure power dissipated in a matched or unmatched load is presented. It is designed with a view to being implemented a rf discharge diagnostic. The physical construction and calibration technique are explained. The design is a wide band, hybrid directional coupler/current-voltage sensor suitable for fundamental and harmonic power measurements. A comparison with a standard watt-meter shows that this in-line sensor is significantly more accurate at higher frequencies and at increased mismatch conditions.

Finally, conclusions to this work are drawn in chapter 6. The major findings are discussed and suggestions for further work are made.

CHAPTER 2

Experimental setup and electrical diagnostics

The experimental reactor used in this thesis (Applied Radio-frequency Ion Source or ARIS) was designed for the study of low temperature plasma chemistry [35]. It is an inductively coupled rf discharge ignited in a small source region. The source is open at one end to a much larger chamber into which the plasma flows. This larger chamber region is fitted with numerous vacuum ports through which the plasma is easily accessed with diagnostic probes. The source region is also fitted with an axial dc magnetic field that can be used to excite helicon discharges. For the experiments presented here the discharge has been run in the inductive power coupling mode.

2.1 Reactor geometry

The reactor consists of two distinct regions as shown in figure 2.1. The source region is made from a dielectric tube with an external diameter of 100 mm, wall thickness 10 mm and length 150 mm. The rf power is coupled to this region with a two turn antenna which encompasses the source tube. The whole region is also surrounded with an aluminium electrostatic shield to prevent rf radiation escaping. The aluminium shield still permits the application of the dc magnetic field if desired.

One end of the source tube is open to the diffusion region where the plasma expands. The diffusion region is made from stainless steel. It has an internal diameter of 410 mm and is 290 mm long. It is closed at both ends with either stainless steel or aluminium end plates depending on the application. The source tube attaches to one end through an aperture with a diameter equal to the outer diameter of the source tube. The electrostatic shield mounts directly to this plate to hold the source in place.

2.2 RF power coupling

Radio frequency current at 13.56 MHz is driven through the antenna with an RFPP (Radio-Frequency Power Products) 3 kW generator. The antenna impedance is matched to the generator output impedance (50 Ω), using a matching network, to achieve maximum power transfer.

The matching box is situated to allow direct connection of the antenna to the output capacitor of the match network. This minimizes ohmic power loss at the antenna side of the matching network. The match box is used in automatic matching mode so that the power delivered to the discharge is held constant.

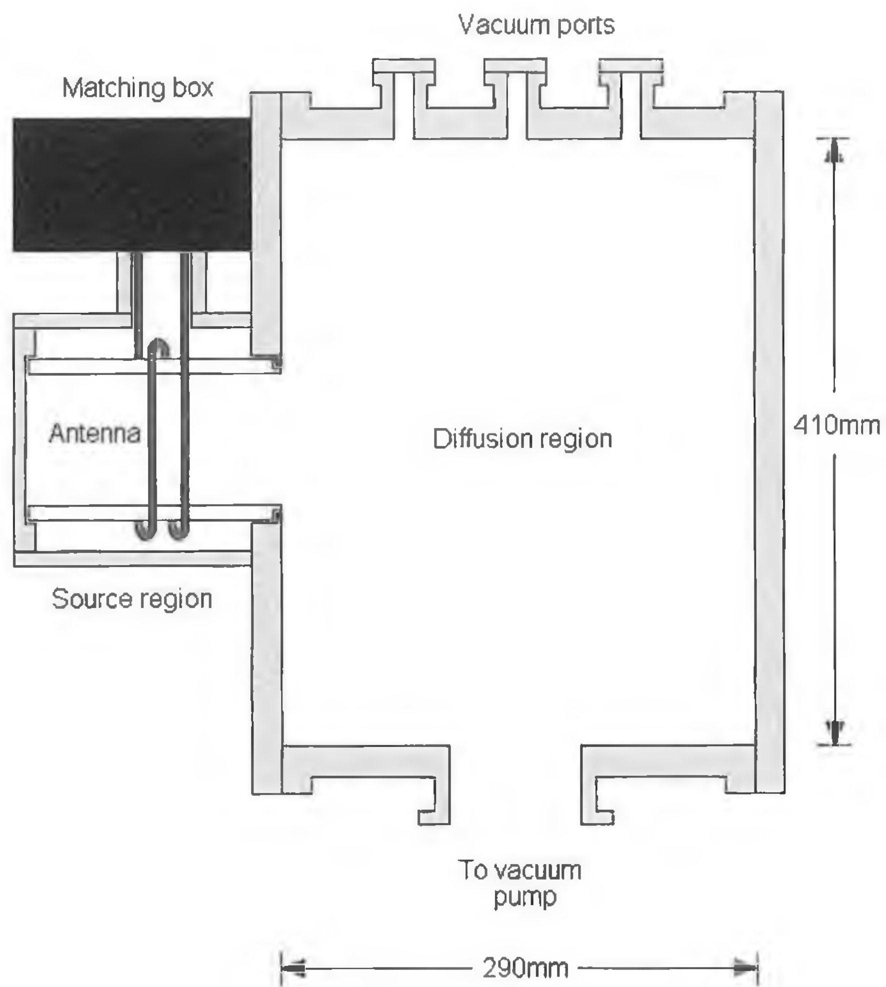

Figure 2.1: *Schematic of the ARIS device showing source and diffusion regions.*

The source needs to be air cooled as some of the rf power is dissipated in the antenna itself. At high frequencies the resistance of the antenna increases due to the skin effect and is accompanied with power dissipation. Ion bombardment of the source walls also leads to heating of the source region.

The discharge is ignited initially in capacitive mode by the large rf voltage on the antenna. When the plasma density increases sufficiently the discharge moves to an inductive mode and is sustained by the time varying magnetic field associated with the rf currents through the antenna.

2.3 Vacuum system

The gas used in all experiments is Argon. Gas is fed to the large chamber using a mass flow controller rated at 100 SCCM and pumped with a turbomolecular pump backed with a rotary pump.

The base pressure of the system is $\approx 1 \times 10^{-6}$ mbar, but the experimental operating pressure was held around 1×10^{-3} mbar $\approx$ 1 mTorr. This operating pressure is required to ensure a collisionless sheath at the rf biassed electrode described in the next section. Initial plasma density and electron temperature measurements were taken in the vicinity of the electrode and found to be approximately $4x10^{15}m^{-3}$ and 4 eV respectively. Thus the mean free path (λ) for electron-neutral momentum transfer is about 20 cm. This is close to the chamber dimensions and much larger than the sheath width at the driven electrode which was found to be no more than 5 mm. Generally, the gas flow is held constant and the pressure is adjusted using a large gate valve mounted between the turbo pump and the chamber.

2.4 Radio-frequency biassed electrode

An electrode is mounted on the end plate of the inductively coupled plasma reactor. The electrode is excited with an rf voltage which is capacitively coupled from a separate generator (and at a different frequency) to that powering the inductive source. No matching network is used to enhance power coupling through this electrode. Instead an inductive coil is placed in series with the blocking capacitor to step up the voltage at the electrode surface. This method allows relatively large exciting voltages on the electrode for relatively low output power levels of the rf generator. Additionally, as there is only small amounts of power coupled through the electrode, the plasma created by the inductive source remains unperturbed. A dc supply is incorporated to allow control of the electron current reaching the electrode surface.

The electrode is a 60 mm copper disc mounted in a PTFE (PolyTetraFluoroEthylene or teflon) holder which prevents plasma formation behind the electrode. A schematic detailing the mounting of the electrode and the biassing circuitry is given in figure 2.2. An equivalent circuit model of the system showing both the rf and dc current paths is given in figure 2.3.

2.4.1 RF bias circuit

The rf bias circuit has two important functions, to capacitively couple the rf power to the discharge and to step up the rf voltage at the electrode surface. Capacitive coupling is easily achieved by placing a blocking capacitor in series with the rf generator. To understand how the voltage amplification is achieved the circuit can be examined from the point of view of the rf generator as shown in figure 2.4. The impedance of the dc bias circuit is designed

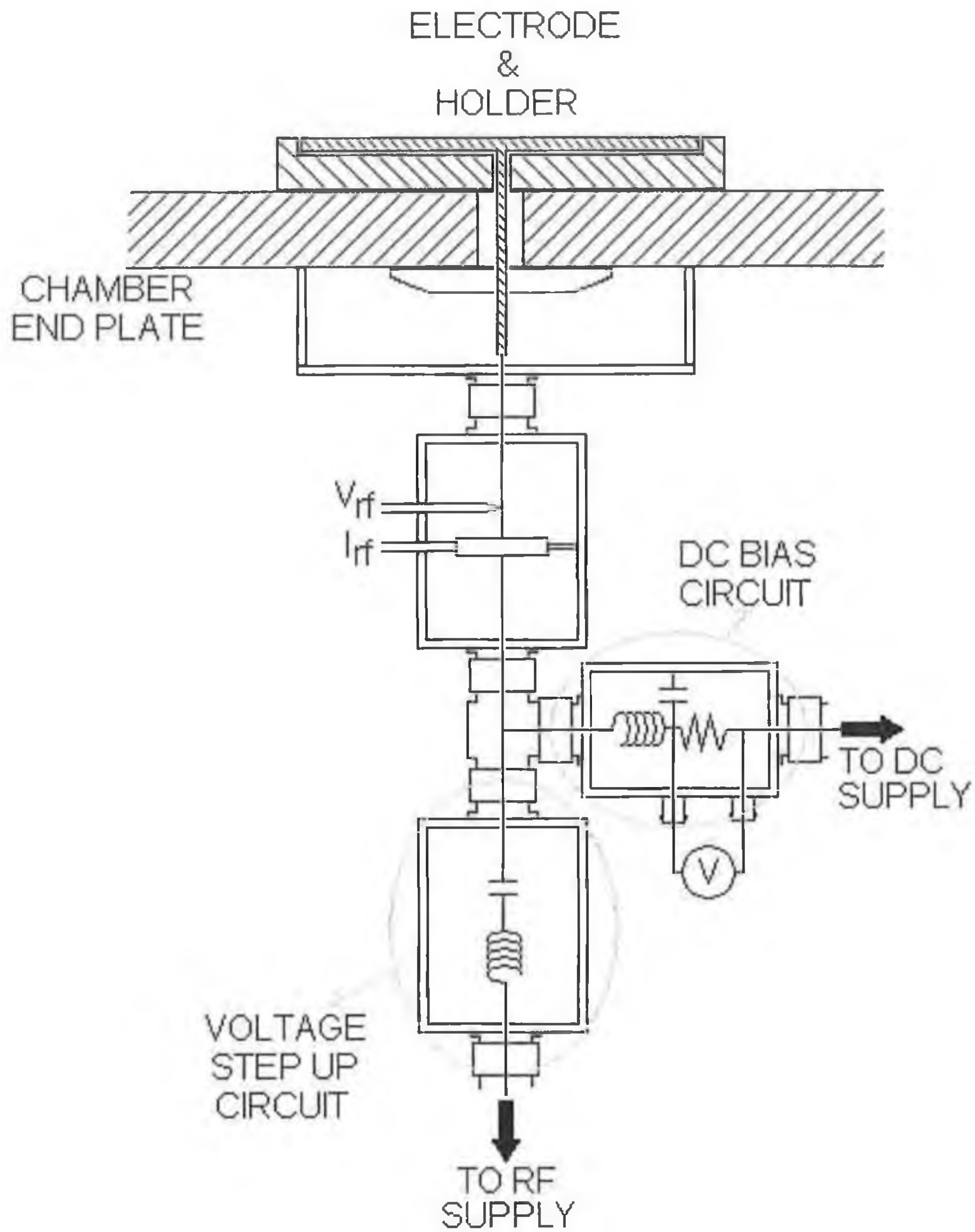

Figure 2.2: *Schematic of the biassed electrode system, showing both the rf power coupling circuit and the additional dc biassing circuit.*

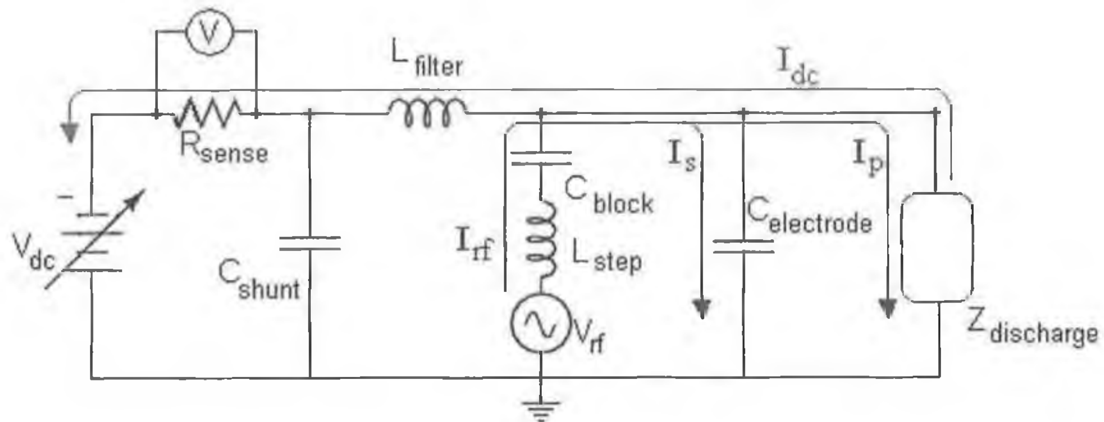

Figure 2.3: *Equivalent circuit model of the electrode system and bias circuitry. C_{block} and C_{shunt} are blocking and shunt capacitors respectively. $C_{electrode}$ is the electrode capacitance to ground and L_{filter} blocks rf current reaching the dc supply. I_s and I_p are the stray and plasma rf current respectively and I_{dc} is the dc current drawn by the dc supply.*

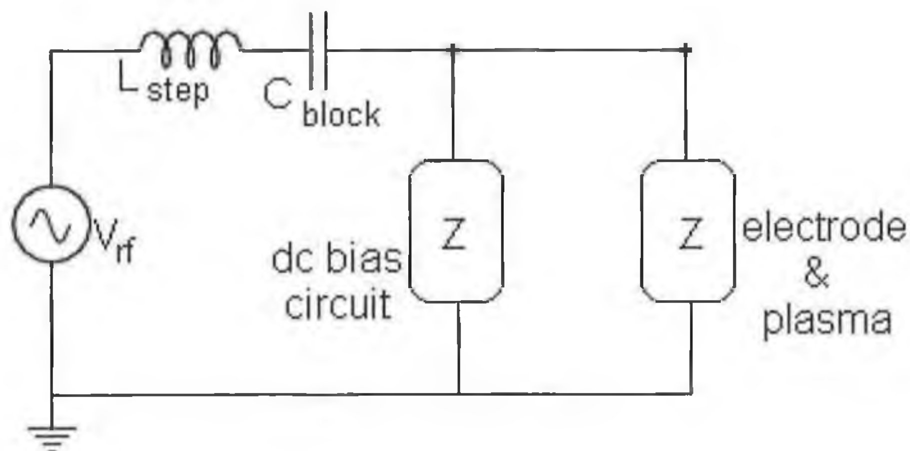

Figure 2.4: *The equivalent circuit as seen by the rf generator.*

to be very high at the applied frequency and so can be ignored as there is almost zero rf current through it. The impedance of the electrode/discharge combination is mainly capacitive. The blocking capacitor has been chosen so that the total capacitive reactance in the circuit is almost equal to the inductive reactance of the step up coil. This leads to a resonance effect allowing large rf currents to flow in the circuit, as the total impedance becomes small. However as the components alone have quite large impedances they must individually have quite large voltage drops to maintain the large current through the circuit. A large rf voltage can be obtained at the electrode surface for low level applied rf power.

2.4.2 DC bias circuit

The dc bias circuit allows an additional negative dc voltage be applied to the electrode. This enables one to control the amount of electrons reaching the surface of the electrode. A circuit model from the point of view of the dc power supply is given in figure 2.5. The inductor (L_{filter}) is chosen to have high impedance at the rf bias frequency and harmonics thereof. This prevents rf current flowing through the dc supply. In the event that some rf current passes through the inductor a very low impedance (0.1 μF) shunt capacitor (C_{shunt}) will conduct it safely away to ground. The sense resistor is used to monitor the dc current reaching the electrode when the negative bias is applied. It is also used to indicate the self bias level of the electrode due to the applied rf signal i.e. when the voltmeter reads zero there is no net dc current flow.

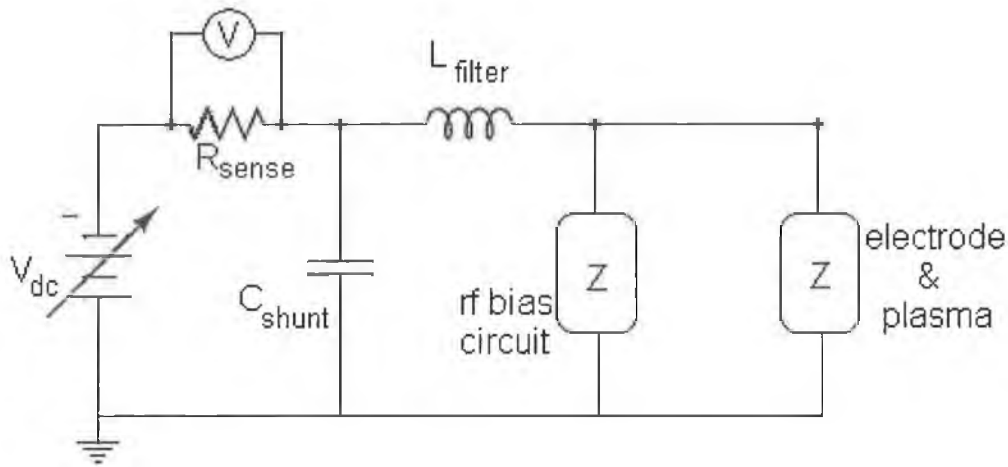

Figure 2.5: *The equivalent circuit as seen by the dc bias supply.*

2.5 Current and voltage probes

Proprietary current and voltage probes are mounted on the power feed line as close to the electrode as possible. The characterization of the power coupling through the plasma sheath is reliant on accurate measurement of the rf current and voltage and their relative phase at the electrode surface. The founding of the Gaseous Electronics Conference (GEC) Reference cell programme [36] has led to the development of accurate techniques [37, 38] for monitoring discharge electrode voltages and plasma currents and are adopted here.

2.5.1 Probe propagation delays

First propagation delays associated with probe cables are accounted for using a method prescribed by Sobolewski [37]. A cable time delay Δt will shift the phase of a signal at frequency f by an amount $\Delta\theta$, where $\Delta\theta = (360^o)f\Delta t$. The phase error of the voltage probe is measured by connecting the probe

tip directly to one channel of an oscilloscope and connecting the output to a second channel. By applying sinusoidal signals at varying frequencies to the probe tip and measuring the phase difference between the two oscilloscope channels a plot of phase error as a function of frequency can be made. The time delay is then obtained from the slope. The time delay associated with the current probe is indirectly calculated by measuring the phase of the voltage relative to the current (impedance phase) in purely capacitive, inductive and resistive loads. The measured phase is compared to the expected values (-90°, $+90^o$, and 0° respectively) and again the phase error as a function of frequency is used to obtain the time delay. The phase error as a function of frequency for both probes is given in figure 2.6. A discrete Fourier transform algorithm is then employed to correct the phase error of the relevant frequency components of the captured signals.

2.5.2 Characterization of parasitic impedance

Secondly, the network of parasitic impedances that exist between the measurement point and the electrode surface is accounted for. This method is described elsewhere [37] and only a brief description is given here. We define the voltage at the powered electrode relative to the grounded walls as $V_e(t)$ and the current flowing through the electrode to the plasma as $I_e(t)$. In contrast, the voltage and current at the measurement point are defined as $V_m(t)$ and $I_m(t)$ respectively. $V_e(t)$ and $I_e(t)$ differ from $V_m(t)$ and $I_m(t)$ for a number of reasons. Some of the measured current leaks away due to parasitic capacitance to ground, and some of the measured voltage is dropped across parasitic inductance and resistance of the power feed cable. Other authors have used an inductive shunt circuit [37, 39, 40] between the measurement point and electrode to remove the stray capacitance to ground. This is neces-

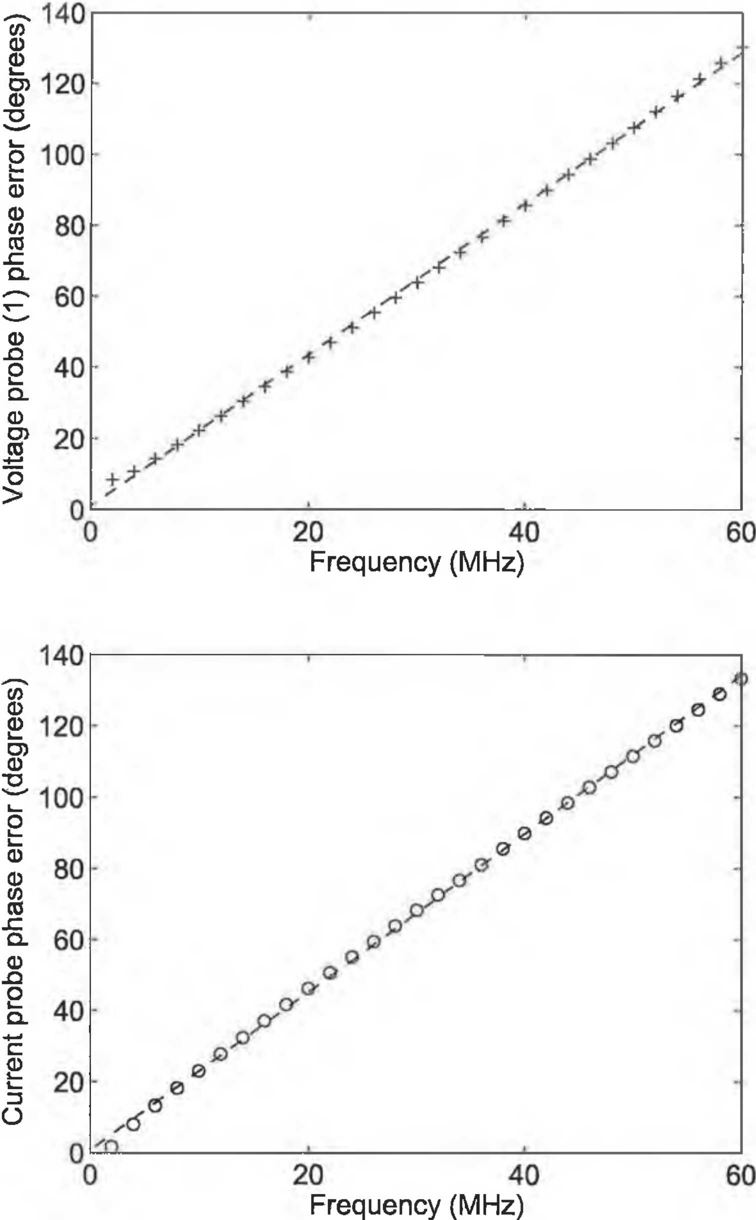

Figure 2.6: *Voltage and current probe phase errors*

sary when the stray capacitance is large (hundreds of pico-Farads) and most of the current is coupled directly to ground rather than through the plasma. In this situation it is difficult to extract the small plasma current with good accuracy. Our system has been designed with minimal electrode capacitance to ground ($\approx 20\ pF$). This avoids the necessity of a shunt circuit as the plasma current is sufficiently large, with respect to the ground current, to determine accurately.

The impedance of the parasitic components vary with frequency and so Fourier analysis is necessary. In the frequency domain the signals $V_e(t)$, $I_e(t)$, $V_m(t)$ and $I_m(t)$ are defined simply as V_e, I_e, V_m, and I_m respectively. The system of parasitics is treated as a two-port network [37] with arbitrary component values and with two inputs (V_m, I_m) and two outputs (V_e, I_e). The inputs and outputs are related by the transmission matrix

$$\begin{bmatrix} V_m \\ I_m \end{bmatrix} = \begin{bmatrix} a & b \\ c & d \end{bmatrix} \begin{bmatrix} V_e \\ I_e \end{bmatrix}, \tag{2.1}$$

where a, b, c, and d are the complex frequency dependant transmission parameters that fully characterize the network of parasitics assuming a linear, reciprocal network. As a result only three of the transmission parameters are independent as the determinant of the transmission matrix for a reciprocal network is unity,

$$ad - bc = 1. \tag{2.2}$$

Rearranging (2.1) gives,

$$\begin{bmatrix} V_e \\ I_e \end{bmatrix} = \begin{bmatrix} d & -b \\ -c & a \end{bmatrix} \begin{bmatrix} V_m \\ I_m \end{bmatrix}. \tag{2.3}$$

Solving (2.3) for open and short circuit measurements yields

$$a = \left(\frac{V_m}{V_e}\right)_{I_e=0}, \tag{2.4}$$

$$c = \left(\frac{I_m}{V_e}\right)_{I_e=0}, \tag{2.5}$$

and

$$\frac{b}{d} = \left(\frac{V_m}{I_m}\right)_{V_e=0}. \tag{2.6}$$

These four transmission parameters are then determined (as a function of frequency) by mounting a second phase calibrated voltage probe on the electrode surface with no plasma present. This probe measures V_e for the open circuit condition and verifies that $V_e = 0$ for the short circuit condition. V_m and I_m are measured with the same I-V probes used when the plasma is present. A correction is required because of the non-zero current flowing for the condition $I_e = 0$. There is no significant capacitance between the front of the electrode and ground because of the large size of vacuum vessel, but there is capacitance associated with the voltage probe. This capacitance, 8pF for the probe used, conducts some displacement current which must be included. A second set of transmission parameters are defined (a', b', c' and d') for the network which include the probe capacitance C_P and is related to the original matrix by

$$\begin{bmatrix} a & b \\ c & d \end{bmatrix} = \begin{bmatrix} a' & b' \\ c' & d' \end{bmatrix} \begin{bmatrix} 1 & 0 \\ i\omega C_P & 1 \end{bmatrix}. \tag{2.7}$$

where the second matrix on the right hand side is the transmission matrix of the probe capacitance alone. The parameters a, b, c, and d are still calculated as described above but the electrode voltage and current are not calculated from (2.3). They are calculated from the result of substituting (2.7) into (2.3) which gives

$$\begin{bmatrix} V_e \\ I_e \end{bmatrix} = \begin{bmatrix} d & -b \\ -c + (i\omega C_P)d & a - (i\omega C_P)b \end{bmatrix} \begin{bmatrix} V_m \\ I_m \end{bmatrix} \tag{2.8}$$

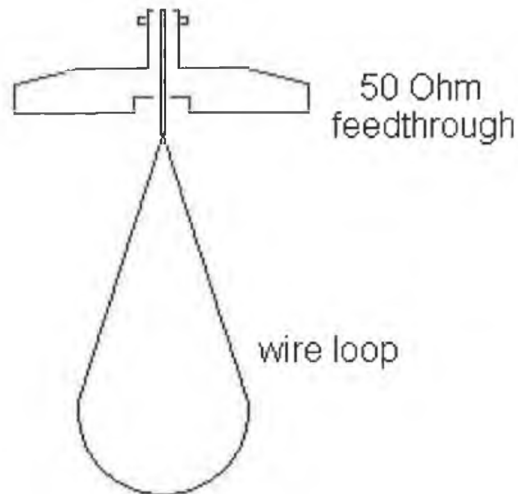

Figure 2.7: *Schematic of the wire loop probe construction showing the* 50 Ω *vacuum feed-through.*

2.6 Electrostatic probes

2.6.1 Wire loop probe

The dc and rf components of the plasma potential are monitored with a floating wire loop probe. The wire loop is mounted about 10 cm from the rf biassed electrode and rests in the same plane. It consists of a 0.3 mm diameter tungsten wire of length 70 cm which is formed into an elliptical shape. The large length of wire ensures a small sheath impedance while being only minimally intrusive. This is true because the radius of the probe wire is smaller than the mean free path of the electrons at our low operating pressures and therefore there is no significant distortion of the plasma about the wire.

The probe wire is attached to a metal pin on the vacuum side of the feed-through and fed to a BNC connector on the outside. A schematic of

the probe construction is given in figure 2.7. The probe output is then terminated to ground through an attenuating voltage probe with 8 pF input capacitance in parallel with a 10 MΩ resistance. The probe output is dc coupled to a digital oscilloscope to view both the rf and dc components of the plasma potential. The measured signals are not exactly the dc and rf components of the plasma potential but only proportional to them. The dc component actually approximates the floating potential which differs from the dc plasma potential by the dc voltage drop across the probe sheath. Similarly the measured rf component is not exactly the rf plasma potential. It is slightly smaller due to the finite ratio of the probe impedance to that of the sheath - the two components of the probe rf voltage divider circuit. In general the actual dc plasma potential is calculated from the "knee" of a compensated Langmuir probe characteristic [41], while a method discussed by Godyak [42] using a similar probe construction to the one described here allows the actual rf plasma potential to be calculated. This is not necessary in the present work as the probe is only used to indicate any changes in the plasma potential which would be noted as a change in either component of the measured signal.

2.6.2 Langmuir and 50Ω probes

The Langmuir probe system consists of a Scientific Systems probe and home made bias electronics to obtain the I-V trace [35]. Passive rf compensation is incorporated to make the probe tip follow the rf plasma potential oscillation. The compensation consists of inductors tuned to have high impedance at the fundamental plasma excitation frequency and harmonics thereof, which in this case is 13.56 MHz. The dc bias voltage is swept from -100 V to +100 V with a sweep rate of 100 Hz and the dc current at each bias is recorded

using a data acquisition card and PC. The I-V trace is averaged over many sweeps and the resulting traces are analyzed in the usual way to obtain values for the electron density, electron temperature, floating potential and plasma potential.

The 50Ω probe consists of a semi-rigid co-axial cable with 50Ω characteristic impedance shielded in a ceramic case. The probe tip (0.3 mm diameter and made from molybdenum) is attached to the inner conductor and protrudes from the ceramic to contact the plasma. At the point of exit from the reactor the semi-rigid cable is connected to a more standard flexible 50Ω cable to transfer the signals to a spectrum analyzer with 50Ω input impedance and bandwidth of 2 GHz. This probe is mounted very close to the sheath edge and used to monitor high frequency sheath potential oscillations.

2.7 Summary

In summary the experiment and all diagnostics have been detailed. The geometry and operation of the reactor used to generate the discharge has been outlined. The reactor itself is an inductively coupled system made of a source region and a diffusion region. The plasma is ignited in a high density source region and subsequently diffuses into a much larger cylindrical chamber where various diagnostics are mounted. The gas used is argon at a pressure of about 1 mTorr for all experiments presented. The rf power is set to a constant value of 500 W at a frequency of 13.56 MHz.

The inductive reactor is used to maintain the plasma only, while all results have been taken using an independently rf driven electrode mounted far from the inductive source. The electrode is driven at a separate frequency from the inductive source so as to avoid interference effects such as beating. Power

coupled through the resulting capacitive sheath in front of the electrode is analyzed using current and voltage probes mounted near the electrode. A thorough description of the calibration procedure for these probes has been given to account for phase error and parasitic impedance. Also, the circuitry needed to apply both rf signals and dc bias levels to the electrode have been explained. This circuitry is important so that the rf supply does not affect the dc supply and vise versa.

The wire loop probe, Langmuir probe and 50Ω probe construction, mounting and operation is detailed. The wire loop probe provides information on the amplitude of the rf plasma potential in the bulk. The langmuir probe provides measurements of the dc plasma potential, electron temperature, and electron density near the sheath. These measurements are used as input parameters to a PIC simulation used for comparison in chapter 4. The 50Ω probe is used to monitor high frequency sheath potential oscillations the results of which are presented in chapter 4.

CHAPTER 3

Collisionless heating and a test of the pressure heating formulation

3.1 Fermi acceleration

In the sheath region of capacitive rf discharges the electric fields which develop have strong spatial and temporal variation compared to the plasma bulk. It is therefore expected that it is in the sheath region that collisionless heating occurs, as has been shown in the experimental and theoretical work already discussed. The dynamics of the interaction between electrons and the sheath electric field is of crucial importance to the understanding of the power transfer mechanism.

It has been suggested that the model of Fermi acceleration [15] can be applied to this situation. This model treats a particle bouncing elastically between a fixed and oscillating wall or two oscillating walls. On collision

with the wall the particle gains or looses energy according to (1.3). Fermi's argument was that because head on collisions were more probable the particle will on average gain energy if there is no phase correlation between the collisions. It is easy to see how this model can be applied to capacitive discharges where the particle is analogous to an electron and the wall analogous to the oscillating sheath edge. A lot of the early work [43–46] was concerned with finding the conditions under which phase correlation could be lost to permit electron heating in this manner. This work is reviewed thoroughly in [7, 47, 48].

3.2 Fermi acceleration applied to capacitive discharges

As the sheath width of a capacitive discharge oscillates it disperses the velocity of electrons reflected from it. This idea was first proposed [49] to explain the Maxwellian electron distribution found in a dc glow discharge[1] at low pressure with negligible electron-electron collisions. High frequency oscillations were found to exist at the sheath edge even though it was a dc driven discharge.

Afterwards Pavkovich and Kino [50] showed that electron reflection in an rf sheath is accompanied by power absorption. The first explicit application of Fermi acceleration to the collisionless heating mechanism was by Godyak [12]:

> *"In an oscillating double sheath, the potential distribution, and thus the coordinate of the electron-reflection point depend on the*

[1]This idea is commonly referred to as "Langmuir's paradox".

time, and the reflection is analogous to that of solid particles from a vibrating wall. On the average particles acquire energy in this case (the Fermi acceleration mechanism)."

Using this theory he went on to calculate the electron power deposition using a dc sheath potential with a small sinusoidal oscillation. These ideas were advanced by a number of authors [13, 14, 51, 52]. Lieberman [10] proposed an almost fully self-consistent model of the plasma sheath and hence determined the collisionless electron power deposition through the Fermi mechanism.

3.3 Collisionless heating through Fermi acceleration

The resistance of the capacitive rf sheath in the absence of collisions is due to the collisionless heating of electrons. An electron reflected from the sheath undergoes a change in energy, increasing if the electron and sheath collide head on and decreasing if they collide when traveling in the same direction. For an ensemble of electrons encountering the sheath the net effect, as discussed, is an energy gain.

3.3.1 Liebermans calculation

Using figure 3.8 the collisionless power dissipated through the Fermi mechanism has been calculated. An electron traveling from the bulk plasma is reflected back to the bulk when it collides with the sheath edge. Assuming that electrons are incident normal to the sheath edge $s(t)$, with a velocity u, and that the sheath velocity is $u_s(t)$ then the reflected electron velocity u_r is $u_r = -u + 2u_s$. The electron velocity distribution at s is $f_s(u,t)$ normalized

to

$$\int_{-\infty}^{\infty} f_s(u,t)du = n_i(s(t)) = n_s(t). \tag{3.1}$$

The flux of electrons Γ_s onto the sheath edge is

$$\Gamma_s = \int_0^{\infty} u f_s(u,t)du. \tag{3.2}$$

The number of electrons per unit area that collide with the sheath in a time interval dt and velocity interval du is given by

$$(u - u_s)f_s(u,t)dudt, \tag{3.3}$$

which gives a power transfer dP per unit area of

$$dS = \frac{1}{2}m(u_r^2 - u^2)(u - u_s)f_s(u,t)du. \tag{3.4}$$

Using $u_r = -u + 2u_s$ and integrating over all incident velocities gives

$$S(t) = -2m \int_{u_s}^{\infty} u_s(u - u_s)^2 f_s(u,t)du. \tag{3.5}$$

In the absence of the plasma electric field the electron velocity distribution at the ion sheath edge is Maxwellian $g_0(u)$. Accounting for the oscillation of the electrons in the time varying electric field the distribution becomes $f_0(u,t) = g_0(u - u_{e,0})$, where $u_{e,0}$ is the drift velocity of the plasma electrons at the ion sheath edge. The velocity distribution at the instantaneous sheath edge f_s is approximated as

$$f_s = \frac{n_s}{n_0} g_0(u - u_{e,0}), \tag{3.6}$$

where $u > 0$. Substituting (3.6) into (3.5) gives the time varying power absorption

$$S(t) = -2m \int_{u_s - u_{e,0}}^{\infty} u_s n_s[u'^2 - 2u'(u_s - u_{e,0})] + (u_s - u_{e,0})^2] g_0(u')du' \tag{3.7}$$

where u' has been substituted for $u - u_{e,0}$. Using the analytic expression calculated [10] for the sheath velocity the average power $\bar{S}$ is found to be

$$\bar{S} = \frac{3\pi}{32} H m n_0 \bar{u} u_{e,0}^2. \tag{3.8}$$

Here m is the electron mass, n_0 is the electron density at the ion sheath edge, $\bar{u}$ is the mean electron speed and $H = J_0^2/(\pi \varepsilon_0 k T \omega^2 n_0)$ is a dimensionless parameter.

3.3.2 Revised calculation

It was later pointed out [31, 53] that in the previous calculation current conservation has been neglected and in fact when this is included the observed heating vanishes. The problem arises with the approximation of the distribution function at the electron sheath edge $f_s = \frac{n_s}{n_0} g_0(u - u_{e,0})$. The inconsistency lies with the use of $u_{e,0}$ (the drift velocity at the ion sheath edge) instead of $u_{e,s}$ which is the drift velocity at the electron sheath edge. Equating convection current to displacement current at the electron sheath edge gives

$$-e n_e u_{e,s} = -e n_i u_s = J_0 sin(\omega t), \tag{3.9}$$

where n_i is the ion density at the electron sheath edge. As quasi-neutrality still holds at the electron sheath edge $u_{e,s}$ must be equal to u_s. In other words the electrons at the electron sheath edge must have a drift velocity equal to the sheath velocity $u_{e,s} = u_s$. The corrected electron velocity distribution is therefore

$$f_s = \frac{n_s}{n_0} g_0(u - u_s). \tag{3.10}$$

Substituting (3.10) into (3.5) gives

$$S(t) = -2m \int_0^\infty \frac{n_s}{n_0} u_s u'^2 g(u') du, \tag{3.11}$$

where $u' = u - u_s$. Using $-n_s u_s = n_0 \tilde{u}_0 sin(\omega t)$, where $\tilde{u}_0$ is the amplitude of the drift velocity in the bulk plasma, the result is, after carrying out the integration,

$$\bar{S} = 2n_0 \tilde{u}_0 kT_e sin(\omega t). \tag{3.12}$$

It is clear that averaging (3.12) over an rf cycle yields zero net heating. This implies that in order for power transfer through this mechanism to occur, then deviations from the hard wall approximation must exist, or alternatively the distribution function at the electron sheath edge is not a drifting Maxwellian. In [53] a direct calculation of (3.5) has been performed using electron distributions, taken from PIC simulations, at the electron sheath edge for one hundred evenly spaced time intervals in the sheath rf cycle. Again it was shown that the net heating averaged to almost zero with the conclusion again being that the collisionless heating could not be explained through the Fermi acceleration mechanism.

3.4 Pressure heating

Turner proposed that the collisionless heating of electrons in capacitive discharges could be described as pressure heating. As the sheaths expand and contract they alternatively heat and cool the electron population in the sheath vicinity. This produces non-equilibrium thermal disturbances and if there is dissipative processes the net work done is not necessarily zero [17, 54]. An analytical model was developed using the moments of the Boltzman equation [31], however the complexity of this model makes it difficult for comparison with experiments and simulation. Later Gozadinos *et al* developed an analytic model also based on the moment equations which is directly comparable with PIC simulations of the heating in the sheath.

3.4.1 The pressure heating equation

In one dimension the plasma electrons can be described by the collisionless Vlasov equation

$$\frac{\partial f}{\partial t} + v\frac{\partial f}{\partial x} - \frac{eE}{m}\frac{\partial f}{\partial v} = 0. \tag{3.13}$$

Multiplying by increasing powers of the velocity and integrating over velocity space, the three velocity moments describing species, momentum and energy conservation are found to be

$$\frac{\partial n}{\partial t} + \frac{\partial nu}{\partial x} = 0, \tag{3.14}$$

$$m\frac{\partial nu}{\partial t} + \frac{\partial}{\partial x}(nT + mnu^2) + eEn = 0 \tag{3.15}$$

$$\frac{\partial}{\partial t}(\frac{1}{2}nt + \frac{1}{2}mnu^2) + \frac{\partial}{\partial x}(\frac{3}{2}nuT + \frac{1}{2}mnu^3 + Q) + eEnu = 0, \tag{3.16}$$

where

$$Q = \frac{1}{2}m\int_{-\infty}^{\infty} v^3 f(v-u)dv \tag{3.17}$$

is the thermal flux. Substitution of (3.14) and (3.15) into (3.16) gives

$$\frac{\partial}{\partial t}(\frac{1}{2}nT) + \frac{\partial(D+Q)}{\partial x} - u\frac{\partial(nT)}{\partial x} = 0, \tag{3.18}$$

where $D = (3/2)nuT$ is the convective flux.

Considering a sinusoidal current driven sheath with a quasi-neutral region between the ion sheath edge and the electron sheath edge and an electron free region between the electron sheath edge and the electrode. In the quasi-neutral region it is assumed that all the current is carried by the electrons such that

$$-enu = \tilde{J}\sin(\omega t), \tag{3.19}$$

and in the electron free region the current is all displacement current. Integrating (3.18) in the quasi-neutral region (from x=0 to x=s(t) in figure 3.8)

gives

$$\int_0^s \frac{\partial \frac{1}{2} nT}{\partial t} \mathrm{d}x - \int_0^s u \frac{\partial nT}{\partial x} \mathrm{d}x + Q\Big|_0^s + D\Big|_0^s = 0, \tag{3.20}$$

It is assumed that the temperature is uniform across the sheath region and (3.20) becomes

$$\frac{1}{2}\frac{\mathrm{d}T}{\mathrm{d}t} \int_0^s n \mathrm{d}x - T \int_0^s u \frac{\partial n}{\partial x} \mathrm{d}x + Q\Big|_0^s + D\Big|_0^s = 0. \tag{3.21}$$

Using current conservation at the sheath edge $-enu = -en\frac{\mathrm{d}s}{\mathrm{d}t} = \tilde{J}\sin\omega t$, we find by integration that,

$$\int_0^s n \mathrm{d}x = \frac{\tilde{J}}{e\omega}(1 + \cos\omega t). \tag{3.22}$$

Here the boundary conditions have been chosen to agree with the definition of current phase i.e at time t=0 the sheath is at the electrode and then expands towards the plasma. Substituting u from (3.19) into (3.21) gives

$$\frac{1}{2}(1 + \cos\omega t)\frac{\tilde{J}}{e\omega}\frac{\mathrm{d}T}{\mathrm{d}t} + \frac{\tilde{J}T}{e}\ln(\frac{n_s}{n_0})\sin\omega t + Q\Big|_0^s + D\Big|_0^s. \tag{3.23}$$

The convective flux at the instantaneous sheath edge $D_s = 3/2 n_s u_s T$ is canceled by that at the ion sheath edge $D_0 = 3/2 n_0 u_0 T$ because of flux conservation. It is also noted that there can be no thermal flux to or from the electron free region and hence $Q_s = 0$. To calculate the thermal flux at the ion sheath edge the electron distribution is split into two populations, one entering the sheath with a density n_{in} and temperature T_{in}, and one leaving the sheath with density n_{out} and temperature T_{out}. The thermal flux at the ion sheath edge can then be written as

$$Q_0 = \frac{1}{2}(n_{in}\bar{v}_{in}T_{in} - n_{out}\bar{v}_{out}T_{out}), \tag{3.24}$$

where $\bar{v}_{in,out}$ are the respective average electron velocities. For consistency the following conditions are necessary:

$$n_{in} + n_{out} = n_0,$$

$$n_{in}T_{in} + n_{out}T_{out} = n_0 T,$$

$$n_{in}^2 T_{in} - n_{out}^2 T_{out} = 0, \tag{3.25}$$

where the first equation means that the sum of the electron densities entering and leaving the sheath must be equal to n_0 at the ion sheath edge. The second equation says that the temperature is identically T at the same point. Finally the third equation implies zero random particle flux at that point. Assuming that $T_{in} = T_b$, the constant temperature of the bulk plasma, Q_0 is uniquely determined to be

$$Q_0 = \frac{1}{2} n_0 \bar{v}_b T \left(1 - \frac{T}{T_b}\right) = Q_b \frac{T}{T_b}\left(1 - \frac{T}{T_b}\right), \tag{3.26}$$

where $Q_b = 1/2 n_0 \bar{v}_b T_b$ is the thermal flux arriving at the sheath edge from the bulk plasma. The pressure heating equation can thus be finally written as

$$(1 + \cos\theta)\frac{\mathrm{d}\tau}{\mathrm{d}\theta} + 2\tau \ln\left(\frac{n_s}{n_0}\right)\sin\theta + \frac{\bar{v}_b}{u_0}\tau(\tau - 1) = 0, \tag{3.27}$$

where $\omega t = \theta$, $u_0 = \bar{J}/en_0$ and $\tau = T/T_b$.

3.4.2 Approximate solution

The solution of (3.27) can be expressed as a power series in $\delta \equiv u_0/\bar{v}_b \ll 1$,

$$\tau = \tau^{(0)} + \delta\tau^{(1)} + \delta^2\tau^{(2)} + \ldots, \tag{3.28}$$

where the τ parameters are functions of θ. Retaining terms up to $O(\delta^2)$ in a binomial expansion and using the fact that coefficients of each order must vanish separately the following set of equations is obtained

$$\tau^{(0)} = 1,$$

$$\tau^{(1)} = -2\ln\left(\frac{n_s}{n_0}\right)\sin\theta,$$

$$\tau^{(2)} = 2(1+\cos\theta)\left[\cos\theta \ln\left(\frac{n_s}{n_0}\right) + \sin\theta \frac{1}{n_s}\frac{\mathrm{d}n_s}{\mathrm{d}\theta}\right]. \tag{3.29}$$

The average power $\bar{P}$ absorbed can now be calculated by noting that it is well approximated by the average thermal flux, at the ion sheath edge, $\bar{Q}_0$

$$\begin{aligned}\bar{P} &= -\bar{Q}_0 \\ &= \frac{1}{2} n_0 \bar{v}_b T_b \langle \delta\tau^{(1)} + \delta^2(\tau^{(2)} + \tau^{(1)^2})\rangle + O(\delta^3) \\ &= Q_b \langle \delta\tau^{(1)} + \delta^2(\tau^{(2)} + \tau^{(1)^2})\rangle + O(\delta^3).\end{aligned} \tag{3.30}$$

3.4.3 Power deposition for a specified sheath density profile

The average power deposited to the electrons through the pressure heating mechanism can be determined when an expression for the electron density profile in the sheath is available. As an example we consider the analytic sheath model provided by Lieberman [10]. The density at the sheath edge is given by

$$\frac{n_s}{n_0} = \left[1 - H\left(\frac{3}{8}\sin 2\phi - \frac{1}{4}\phi\cos 2\phi - \frac{1}{2}\phi\right)\right]^{-1}, \tag{3.31}$$

where $H = \bar{s}_0^2/(\pi\lambda_D^2$, $\bar{s}_0 = \tilde{J}/(e\omega n_0)$ is an effective oscillation amplitude of the sheath and λ_D is the electron Debye length. The phase ϕ is related to θ by $\phi = \theta + \pi$. This solution describes a phase symmetric sheath where the density at any expanding sheath phase is equal to the density at the same collapsing sheath phase. It is clear then that the first order term ($\tau^{(1)} = -2\ln(n_s/n_0)\sin\theta$ averages to zero and (3.30) becomes

$$\bar{P} = Q_b \delta^2 \langle \tau^{(2)} + \tau^{(1)^2}\rangle + O(\delta^3). \tag{3.32}$$

Using the expressions for $\tau^{(1)}$ and $\tau^{(2)}$ and Liebermans expression for n_s/n_0, it has been found that a good fit to (3.32) is

$$\bar{P} \approx Q_b \delta^2 \frac{35H}{60+H}, \tag{3.33}$$

where H lies between 1 and 50, covering all values that H can take for any realistic situation.

In reality the electron density profile is not phase symmetric, as suggested by Lieberman, and electron loss to the electrode must be considered. In this situation there is a finite contribution from the first order term in (3.30) and the second order terms can be ignored. The instantaneous power $P(t)$ becomes

$$\begin{aligned} P(t) &= \frac{1}{2} n_0 \bar{v}_b T_b \delta \tau^{(1)} \\ &= -n_0 \bar{v}_b T_b \delta \ln \frac{n_s}{n_0} \sin\theta \\ &= -n_0 \bar{v}_b T_b \delta \sin\theta \int_0^s \frac{1}{n} \frac{\mathrm{d}n}{\mathrm{d}x} \mathrm{d}x. \end{aligned} \tag{3.34}$$

In figure 3.1 a comparison between the PIC simulation and the analytic pressure heating solution is presented. In the PIC simulation the power per unit area in the sheath region has been calculated directly from

$$\bar{P} = \frac{1}{T} \int_0^{s_m} \int_0^T J_e E \mathrm{d}t \mathrm{d}x, \tag{3.35}$$

where E is the electric field and J_e is the electron current density. To look at the collisionless power absorption alone the electron loss component has been excluded. This can be understood by considering that an electron with sufficient energy to cross the instantaneous sheath potential barrier looses its energy to the electrode. An escaping electron removes $1/2 m_e u_i^2 - 1/2 m_e u_f^2$ of energy, where u_i is its velocity at the sheath edge and u_f is its velocity at the electrode. This power loss reduces the total electron power absorption. In the PIC simulation the energy lost by electrons escaping to the electrode has been calculated as a function of phase in the rf cycle to obtain the power loss $\overline{P_{loss}}(t)$. Ideally the comparison with the analytic model would involve the solution of (3.34) over a density profile obtained from a sheath model

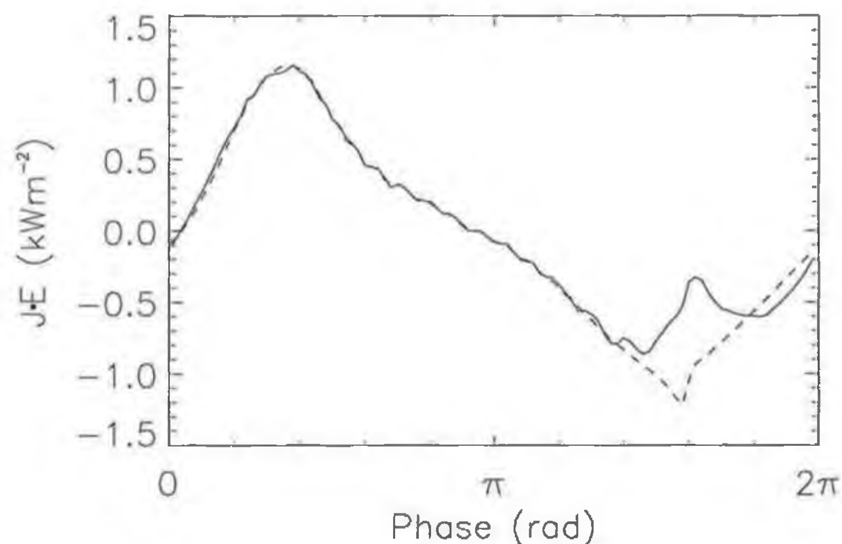

Figure 3.1: *Comparison between the instantaneous power, calculated at various times in the rf cycle, from the PIC simulation (solid line) and from the analytic model (dashed line). The analytic solution uses the density profile obtained from the PIC simulation (after [3]).*

that includes electron loss. However, a model where an analytic form of the density profile can be derived is not available. Therefore the comparison has been performed using the density profile from the PIC simulation. Excellent agreement was found everywhere except the region where electron loss is most important. The conclusion being that electron loss is a significant effect and must be accounted for to accurately model or measure collisionless electron heating.

3.5 Experimental test of the pressure heating model

As discussed in section 1.5 the PIC simulation used by Gozadinos *et al* models a single electrode in contact with a semi-infinite plasma. This allows the sheath region to be modeled in more detail than if a full capacitive discharge were used. The electrode sheath is effectively decoupled from the bulk plasma.

To achieve similar experimental conditions a large volume bulk plasma is ignited in an inductively coupled reactor. A small area electrode is mounted at the chamber wall opposite the source and excited with an rf bias separate from that used to sustain the discharge. Like the simulation the electrode is decoupled from the bulk plasma in the sense that the electrode bias does not control the bulk plasma conditions. The electrode is driven at a frequency of 10 MHz while the inductive source plasma is operated at 13.56 MHz in argon gas. The electrode rf bias is capacitively coupled through a blocking capacitor to allow the self bias to develop. Electrons escape to the electrode at the point in the rf cycle when the electrode potential approaches the plasma potential. An external dc bias is employed to inhibit this electron loss to investigate its effect on the rf power absorption. This method allows a comparison with the prediction that the electron loss component of the electrode current has an associated power loss and subsequently reduces the total electron power absorption. A schematic of the entire experimental configuration is given in figure 3.2. This schematic also shows the positioning of the Langmuir probe and the floating probe. The Langmuir probe is used to measure the plasma potential, electron density and electron temperature in the plasma near the sheath edge. The reason for these measurements are discussed in

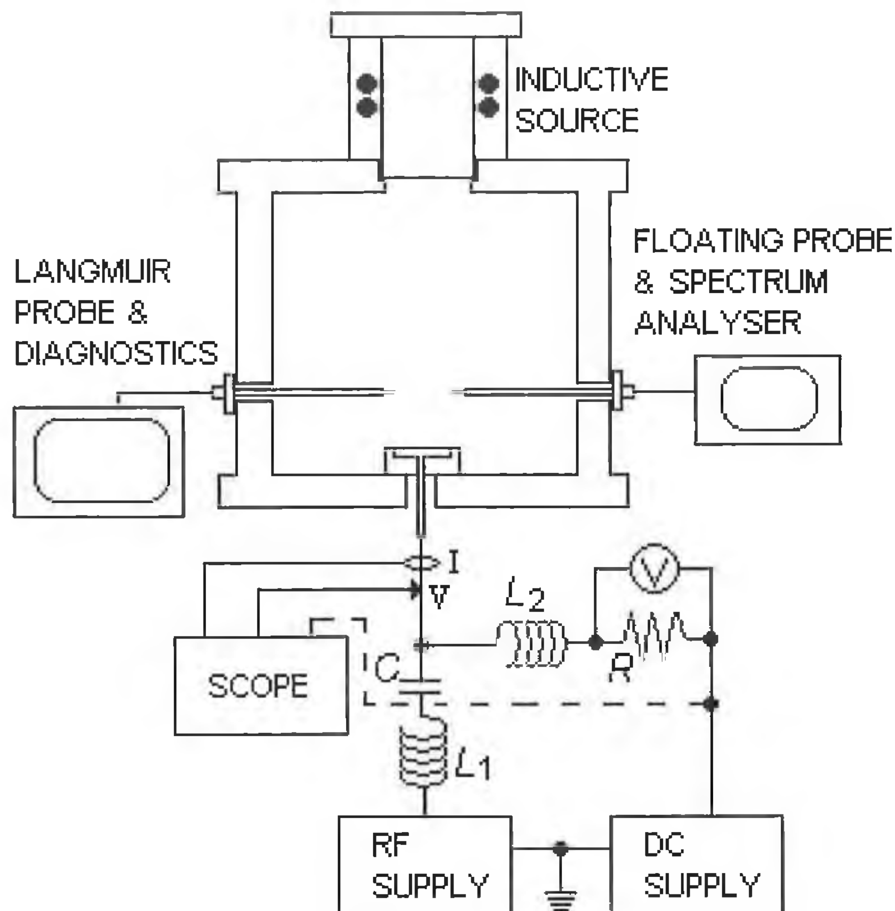

Figure 3.2: *Schematic of experimental apparatus showing the inductive source, the biased electrode and the electrical probe diagnostics.* L_1 *and* C *are used to step up the electrode voltage.* C *also ensures capacitive coupling of the rf supply.* L_2 *blocks rf signals from reaching the dc source and* R *is a* 10Ω *resistor used for sensing the net DC current.*

the following sections of this chapter. The results taken with the floating probe and spectrum analyzer are presented and discussed in chapter 4.

3.6 Electrical Measurements

3.6.1 Current and voltage waveforms

As described earlier the voltage on the front surface of the electrode $V_e(t)$ and the current flowing into the plasma $I_e(t)$ are calculated from $V_m(t)$ and $I_m(t)$ respectively using (2.7). Typical voltage and current waveforms are shown in figure 3.3 and figure 3.4 respectively.

The current signal is composed of both conduction current and displacement current. The conduction current is due to ions and electrons crossing the sheath to the electrode. Because the ions are relatively heavy and the bias frequency is greater than the ion plasma frequency (ω_i) in the vicinity of the biased electrode, the ion current is assumed constant through the rf cycle. The claim that $\omega > \omega_i$ is supported by Langmuir probe measurements near the sheath edge where the density was determined to be approximately $4 \times 10^{15} m^{-3}$ giving an ion plasma frequency of approximately 2 MHz. The electrons being much lighter respond to the instantaneous rf potential. With the electron temperature in the region of 4 eV most of the electron current arrives at the electrode at the point in the cycle when the rf potential approaches the plasma potential. With the plasma potential necessarily being the most positive potential within the system, the point at which electrons escape is at the most positive excursion of the rf electrode potential. When the applied bias is capacitively coupled no net current can flow and the ion current reaching the electrode over an rf cycle is balanced by the electron current. The displacement current represents a storage of charge in the ca-

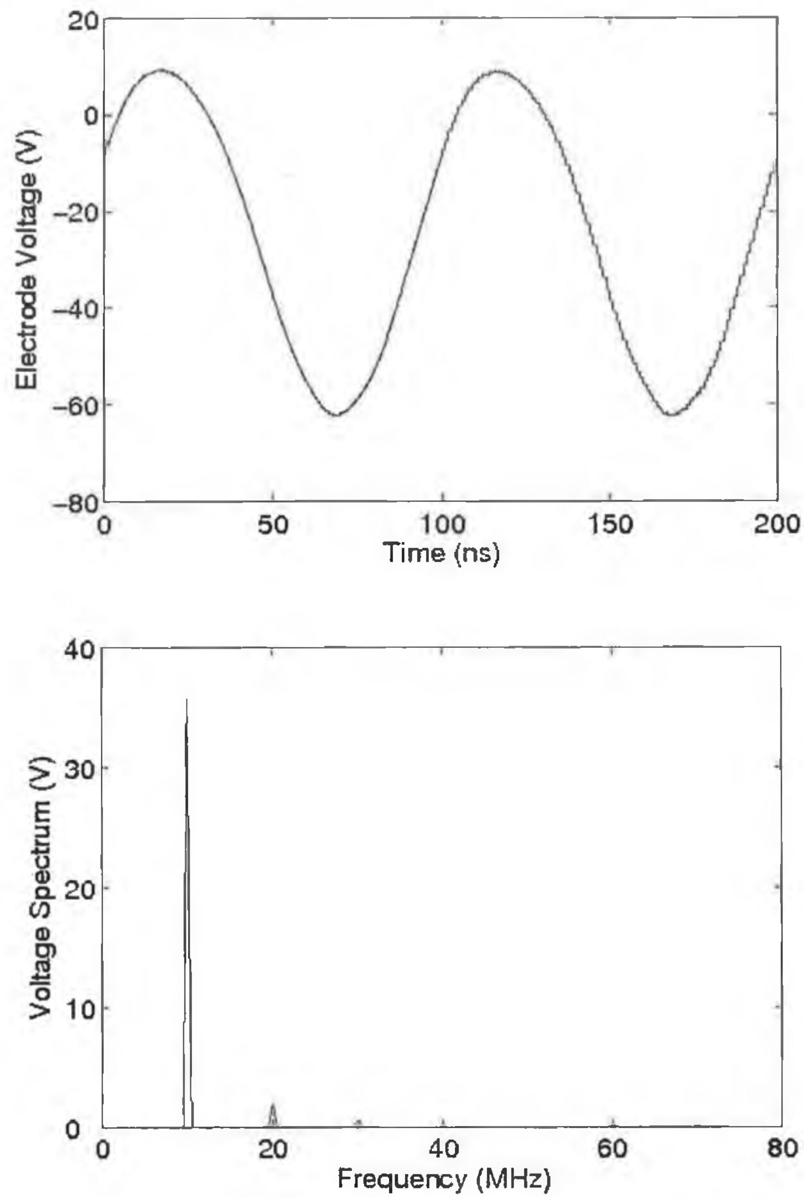

Figure 3.3: *Typical electrode voltage waveform and its frequency spectrum.*

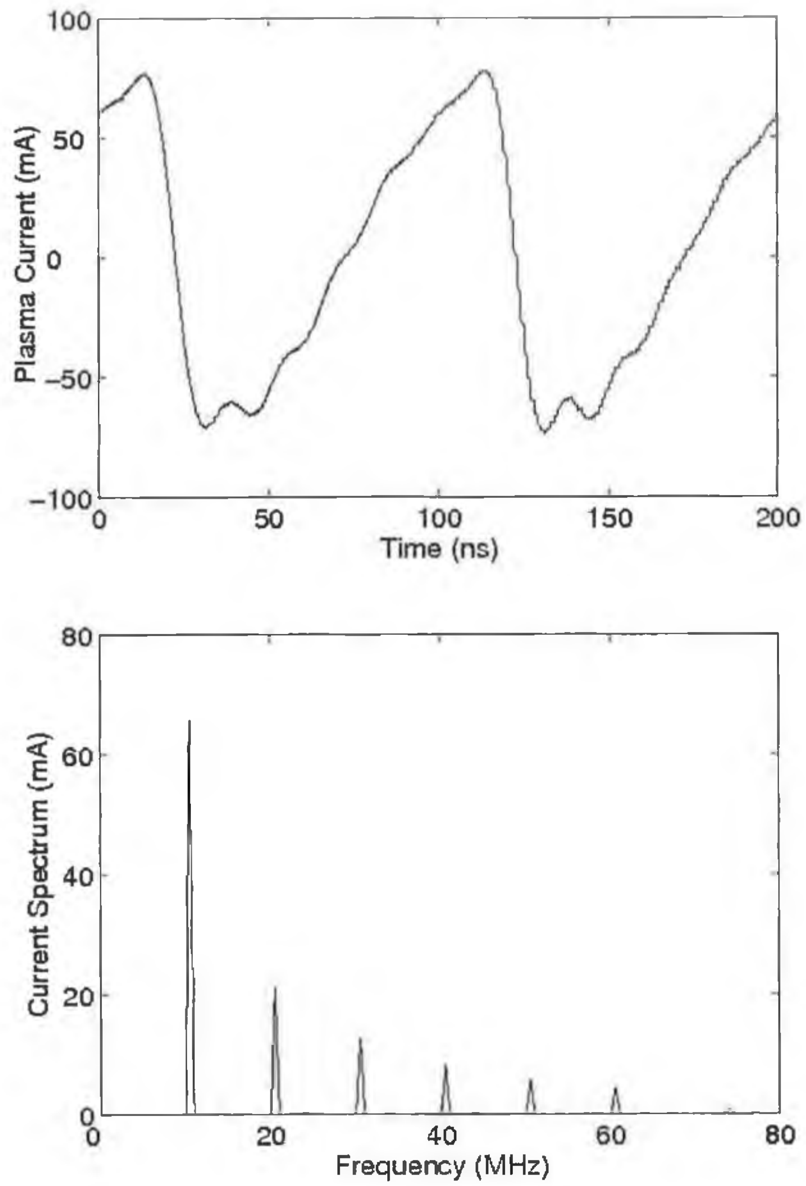

Figure 3.4: *Typical plasma current waveform and its frequency spectrum.*

pacitive element of the sheath impedance. Following normal convention - ions reaching the electrode are registered as negative current while electrons reaching the electrode are registered as positive current. The current monitor cannot distinguish between conduction and displacement currents but measures total current which is the sum of the two.

The voltage signal remains almost sinusoidal at the applied frequency of 10 MHz as expected because the source produces a sinusoidal voltage with negligible harmonic content. The negative dc level is a result of the blocking capacitor in the bias circuit. The current signal on the other hand has definite harmonic content caused by the non linear impedance characteristic of the plasma sheaths. Harmonics present in the measured electrode voltage waveform are thus caused by this current signal flowing through the 50Ω series output resistance of the source.

It is interesting to note that there is no signal components detected at the inductive source frequency or harmonics thereof. The reason for this is that the wall sheath impedance is very small compared to the rf biased electrode sheath impedance due to the large ground area of the chamber walls. Current injected by the inductive source preferentially returns to ground through the wall sheath. The current flowing into the plasma from the electrode has no significant component at the inductive source frequency. This means that power absorbed in the powered sheath contains components at 10 MHz and subsequent harmonics but not at the inductive source frequency 13.56 MHz or its harmonics.

All measurements in this thesis have been taken for the following plasma conditions: inductive source power at 500 W, gas pressure at 1.4 mTorr, inductive source frequency 13.56 MHz, and rf bias frequency 10 MHz.

As discussed in section 2 the pressure was set to obtain a collisionless

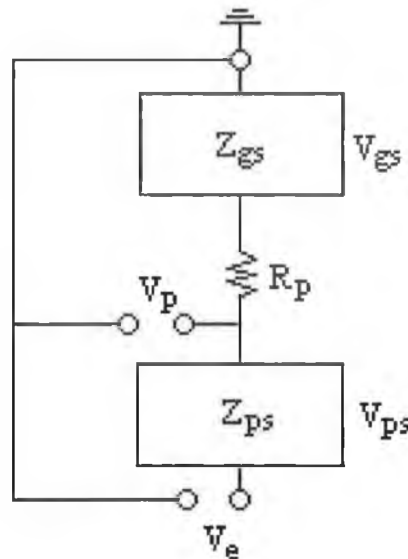

Figure 3.5: *Equivalent circuit model of the discharge. Z_{ps} and Z_{gs} are the power sheath and ground sheath impedances respectively with the accompanying voltage drops V_{ps} and V_{gs}. R_p is the plasma bulk resistance, V_p the plasma potential measured with the wire loop probe, and V_e the applied electrode voltage.*

sheath at the driven electrode. Measurements of the electron density and electron temperature in the sheath vicinity enable a calculation of the electron mean free path and found to be around 20 cm for the conditions used. The driven electrode is also calculated and found to be less than 5 mm for all bias conditions. For these reasons we can be sure that the driven sheath under investigation is indeed collisionless.

3.6.2 Bias voltage distribution

Our system, from the point of view of the rf biased electrode, can be modeled as three distinct regions as in figure 3.5 - the electrode sheath, the plasma bulk and the wall sheath. The applied rf electrode voltage should therefore

be distributed across these regions in proportion to their relative impedances. The plasma bulk which is controlled by the inductive source is conducting with a resistance approaching zero. The wall sheath impedance is also very small because of the large grounded area in contact with the plasma. On the other hand the driven sheath impedance at our low operating pressure is very large. It is therefore expected that the bias voltage would be almost entirely dropped across the driven sheath. This is confirmed by plasma potential measurements, shown in figure 3.6, where there is no component detected at the bias frequency. Other authors working with rf-biased, inductively coupled plasmas [55–58] have seen oscillations in the plasma potential at the bias frequency. The reason for this is related to the reactor configuration. The plasma in those reactors was confined to a relatively narrow column between the rf-biased electrode and the inductive source Faraday shield. The grounded surface (Faraday shield) seen by the plasma is therefore relatively small, creating a relatively large ground sheath impedance. A significant fraction of the rf-bias is dropped between the plasma and ground in that case and is detected in plasma potential oscillation measurements. The reactor configuration presented here is quite different. The high density source plasma diffuses to fill the entire chamber region. As mentioned above, the grounded area seen by the plasma is large and accompanied by a small ground sheath impedance. It is not surprising, therefore, that no rf-bias frequency is detected in the plasma potential measurement.

This also means that none of the applied bias is dropped on the ground sheath as the plasma potential measurement is actually the sum of the bulk plasma potential and the wall sheath potential [59]. There is a small oscillation (1.5 V amplitude) at the inductive source frequency and because the plasma has little resistance most of this signal appears on the wall sheath.

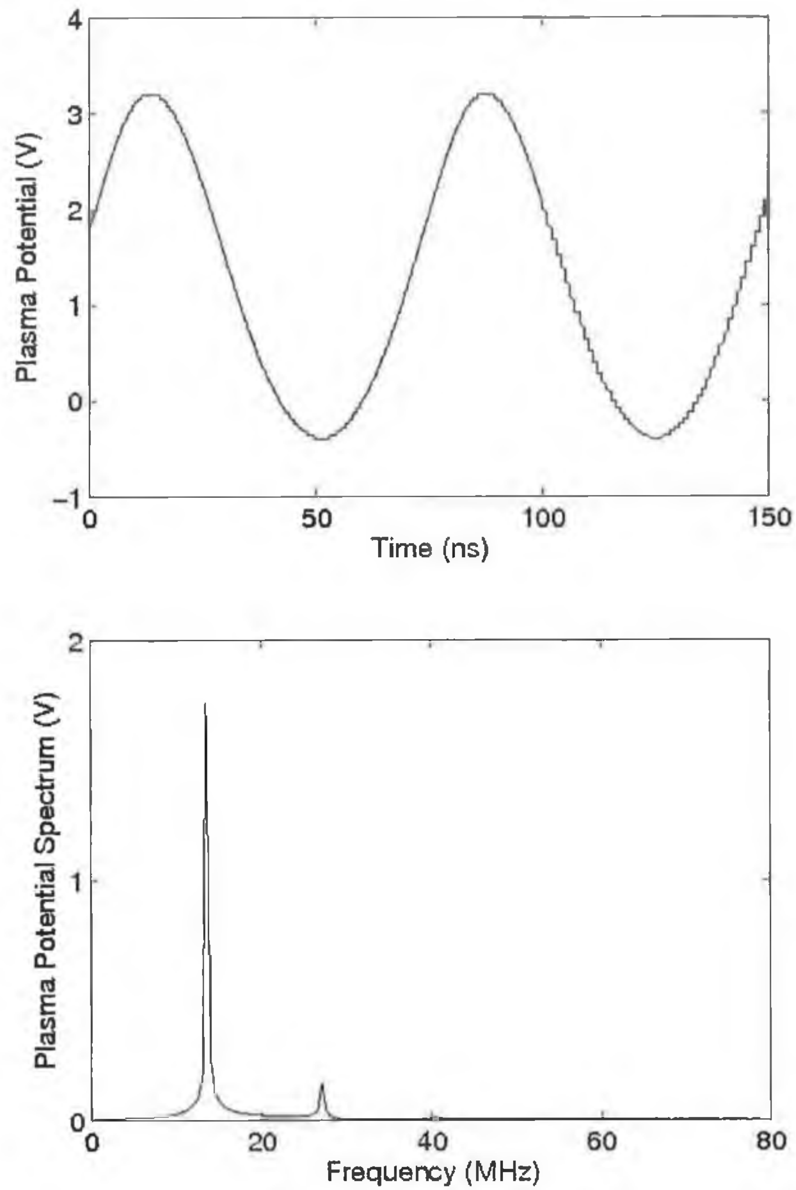

Figure 3.6: *Plasma potential waveform along with its frequency spectrum. Plasma conditions as described in the text.*

The plasma potential does have an appreciable dc component which again we assume is mostly dropped across the ground sheath. This acts in the same way as in the powered sheath, accelerating ions out to the wall while confining electrons in the bulk. Using the plasma circuit model in figure 3.5, with $R_p \approx 0$, the electrode voltage is

$$V_e(t) = V_{ps}(t) + V_{gs}(t) \qquad (3.36)$$

where $V_{ps}(t)$ is the potential across the powered sheath and $V_{gs}(t)$ is the potential across the ground sheath. These potentials have both a dc and a rf component. The powered sheath potential is then

$$V_{ps}(t) = V_e(t) - V_{gs}(t). \qquad (3.37)$$

3.6.3 Instantaneous power absorption

Generally absorbed rf power (P_{abs}) is calculated from the product of the rf current, voltage and cosine of their relative phase

$$P_{abs} = I_{rms} V_{rms} cos\phi \qquad (3.38)$$

where ϕ is the phase angle separating the current and voltage vectors. It is important to note that (3.38) is a linear approximation and is only valid for signals with little or no harmonic content. More importantly (3.38) does not include any power carried by dc components of the current and voltage. In the measurements reported here there is a number of significant harmonic components and dc levels associated with both waveforms, therefore the average absorbed power is more accurately calculated from the product of the instantaneous current ($I(t)$) and voltage ($V(t)$) waveforms integrated over an rf cycle

$$P_{abs} = \frac{1}{T} \int V(t) I(t) dt. \qquad (3.39)$$

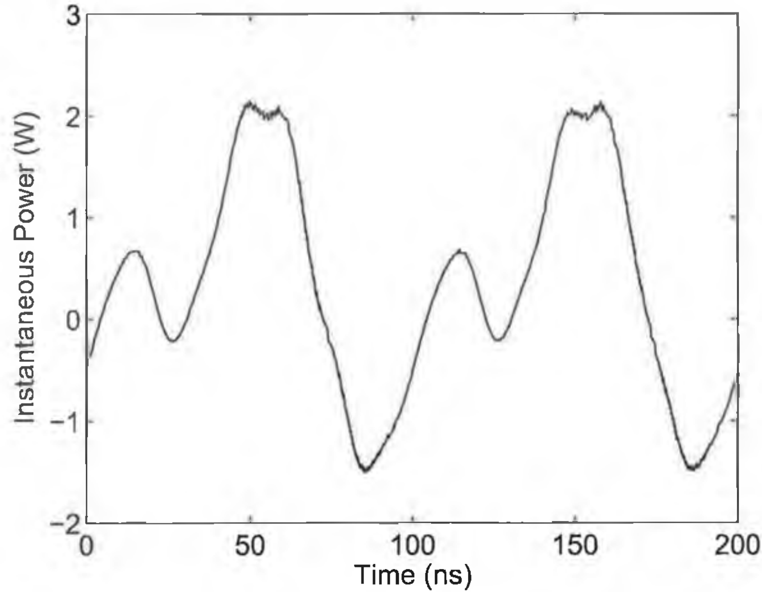

Figure 3.7: *Instantaneous power signal obtained from the product of the current and voltage waveforms in figure 3.*

A typical instantaneous power signal, the product of the instantaneous current and voltage signals, is shown in figure 3.7.

The negative excursions are mainly due to energy stored in the capacitive component of the sheath impedance which is given back to the circuitry in the second half of the rf cycle. In other words the instantaneous power signal contains a component (due to the displacement current) that has equal positive and negative elements that yield zero net power over the rf cycle. The actual absorbed power in this signal goes into two main channels. A constant positive power level exists due to the constant ion current being accelerated across the sheaths. A second power level which oscillates from positive, when the sheaths are expanding, to negative, when they are contracting is associated with electron heating. These two phases of the sheath motion alternately heat and cool the electron population in the sheath vicinity. Crucially for

capacitive discharges that operate at low pressure this power component averages to a net input and is capable of sustaining the discharge (although in this case the plasma is sustained by another independent mechanism - the inductive source).

Power can also be absorbed by secondary electrons released from the surface of the electrode which are then accelerated out of the sheath into the plasma. Secondary electrons can be generated by ion impact, electron impact, neutral impact or photon absorption at the surface of the electrode. It is assumed that the amount of electrons ejected from the surface by neutrals, photons and ions is constant over the applied rf cycle. Electrons released from the surface by electron impact will vary with rf phase. The secondary electron current is likely to be small under the present experimental conditions [4], where the ion and electron energy is relatively low, and can be ignored.

3.6.4 Average power absorption

The structure of the collisionless electrode sheath is given in figure 3.8. The instantaneous electron density equals the ion density on the plasma side of the oscillating sheath edge. It then drops to zero over some distance on the electrode side. Theoretical sheath models often assume that the electron density profile is phase symmetric i.e. the density at any expanding sheath phase is equal to the density at the same contracting sheath phase. This model of the electron density does not allow for electron loss at the point in phase when the rf sheath reaches the electrode. The accuracy of this model electron density profile in the sheath has been investigated indirectly using PIC simulations [8]. Power delivered to the electrons is calculated, as a function of phase in the rf cycle, both with and without electron loss to the

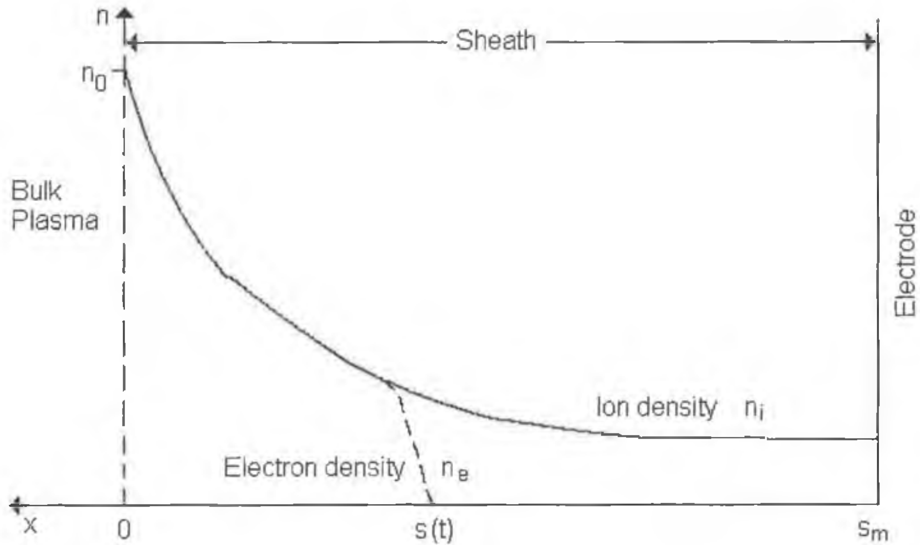

Figure 3.8: *A schematic of the sheath structure showing the ion density (solid) along with the electron density (dashed) at one time (s(t)) in the rf cycle. 0 is the ion sheath edge and s_m is at the electrode - the maximum sheath width.*

electrode. The results show significant differences in power absorption only at the electron loss phase of the rf cycle. The results also indicate that the power absorbed by the electrons, averaged over an rf cycle, is reduced in the calculation performed with electron loss permitted.

In order to investigate this result experimentally the system discussed in section 3.5 is used. In the absence of the dc power supply the capacitively coupled rf bias induces an electrode dc self bias. The electron density profile in this situation is undisturbed and electron loss occurs. This situation is also achieved with the external dc bias included by applying a dc voltage equal to the self bias. When the voltmeter in figure 3.2 reads zero there is no net current through the sheath, the same situation as when the rf bias is used alone. The average power absorbed in the driven sheath at this self bias is calculated using (3.39). Here $I(t)$ is the measured plasma current

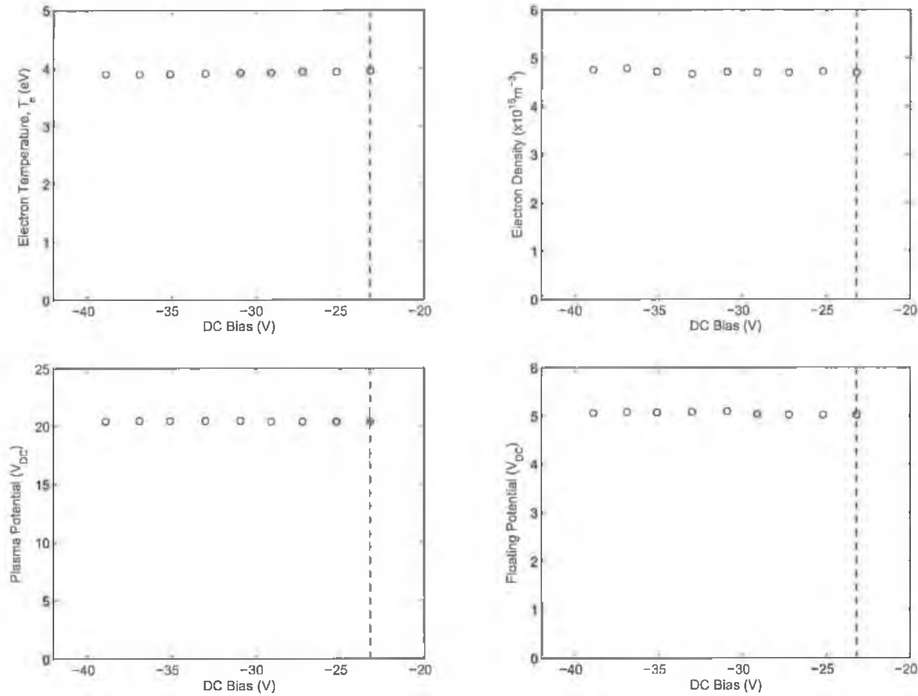

Figure 3.9: *Langmuir probe measurements taken $\approx$ 10 cm from the electrode. The electron density, electron temperature, plasma potential and floating potential remain approximately constant as a function of DC bias applied to the electrode. The vertical dashed line denotes the electrode self bias.*

waveform ($I_e(t)$) while $V(t)$ is the voltage dropped across the driven sheath $V_{ps}(t)$. The voltage dropped across the driven sheath $V_{ps}(t)$ is calculated from equation 3.37. The ground sheath potential $V_{gs}(t)$ is the dc plasma potential (as there is no rf component at the bias frequency) relative to ground and is determined with the compensated Langmuir probe. The dc bias voltage is then increased (made more negative) in order to retard electron loss and the absorbed power is calculated again. No significant change in the dc or rf components of plasma potential was seen (Langmuir probe data for various plasma parameters are given in figure 3.9). This is not surprising since

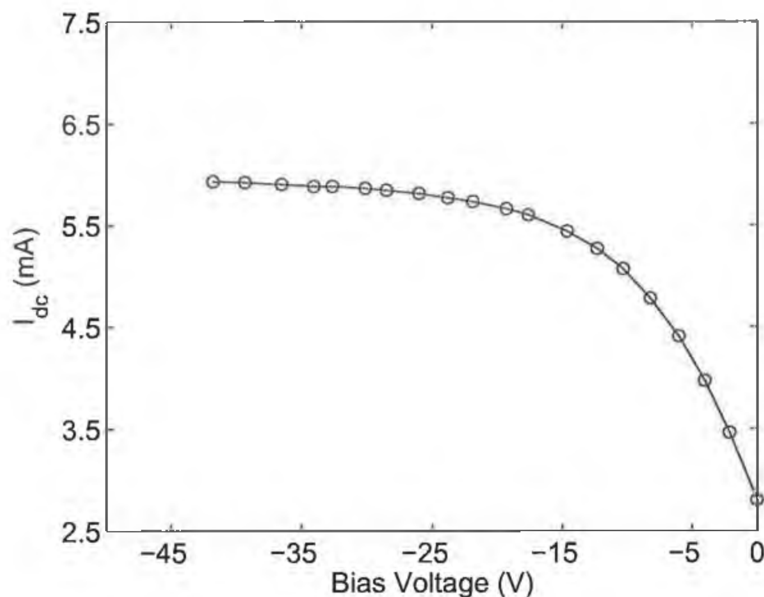

Figure 3.10: *The absolute value of dc current to the electrode as a function of dc bias imposed on the electrode for an inductive source power of 500W, with no rf bias applied.*

the power coupled to the discharge from the electrode is much less than the inductive source power. In order to ascertain the effect of the electron retardation on the electron power absorption the power absorbed by the ions crossing the sheath is removed. To calculate the power absorbed by the ions, the ion current reaching the electrode is determined. The electrode is biased, with the dc supply only, to a large negative dc level. The inductive source power is kept the same as when the rf bias is in operation. At large negative dc bias the plasma electrons are almost entirely repelled and the measured dc current saturates as in figure 3.10. The saturation current is taken to be the ion current at the electrode. The saturation ion current region has been observed in a similar experiment [58] at a biased electrode in an inductively coupled discharge. Experiments performed in parallel plate reactors, simul-

taneously driven with rf and dc power supplies do not show this dc saturation effect [60, 61]. In fact the measured dc current actually decreases in the saturation region. Of course biasing the electrodes of a parallel plate reactor changes the entire discharge impedance. The sheath width at both plates increases with increasing dc bias so both sheath impedance's increase also. This reduces the rf discharge current (for a fixed rf power input) sustaining the plasma. The decrease in rf current decreases the plasma density and hence causes the decrease in the dc current-voltage characteristic in the saturation region. Our system does not suffer from this affect since the plasma density is maintained predominantly by the inductive source.

The effect of increasing negative bias on the average power absorption is given in figure 3.11, where the total power absorbed has been separated into ion and electron power absorption components. The ion power is the product of the ion current (assumed to be independent of dc and rf bias) and the appropriate dc bias voltage drop across the driven sheath. The power absorbed by the electrons is the difference between total power and ion power. The driven sheath is assumed to be collisionless and therefore the power absorbed by the electrons in the sheath is due to both stochastic heating and electron loss to the electrode. An electron, with sufficient energy to cross the sheath electric field and reach the electrode, looses $\frac{1}{2}m_e{u_i}^2 - \frac{1}{2}m_e{u_f}^2$ of energy, where u_i is its velocity at the sheath edge and u_f is its velocity when it hits the electrode. As more and more electrons are prevented from reaching the electrode an accompanying increase in absorbed power is observed as these electrons can no longer remove energy from the system. The increased dc bias across the sheath leads to an increase in ion power which is obvious. The increase in power absorbed by the electrons is not so obvious. The electron conduction current crossing the sheath is registered

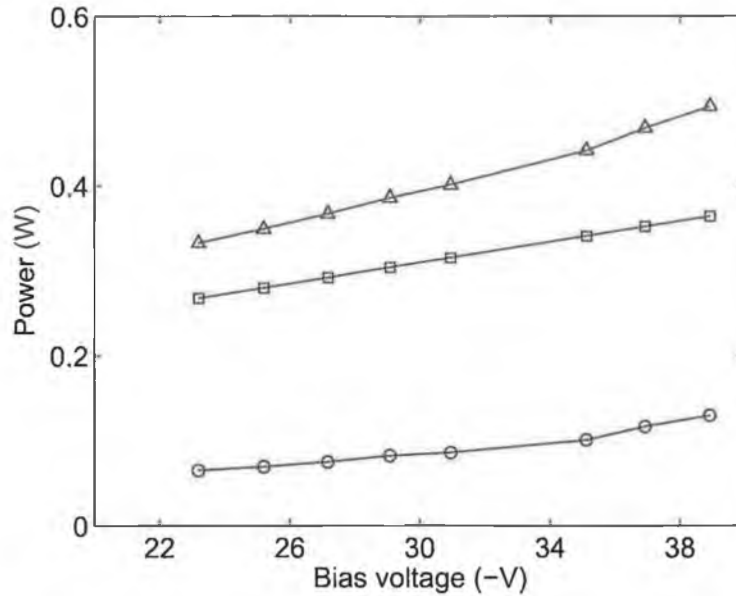

Figure 3.11: *Average power absorbed as a function of increasing negative dc bias. The first point on the graph corresponds to the self biased situation. Triangles represent the total power, while square and circle represent the ion and electron power respectively.*

as positive current as opposed to the ion current which is negative. The dc voltage across the sheath is also negative which explains the positive ion power. The electron loss power is therefore negative meaning that this power is given back to the generator. As the electrons are retarded from reaching the electrode the power lost is reduced i.e the negative power component decreases. Assuming then that the biasing of the electrode does not affect the collisionless power absorption component an increase in total electron power is expected as shown in figure 3.11. The assumption that biasing of the electrode does not change the collisionless power absorption is justified by comparing total current waveforms for a case with electron loss unperturbed and a case where electron loss is retarded. Waveforms of the total current for

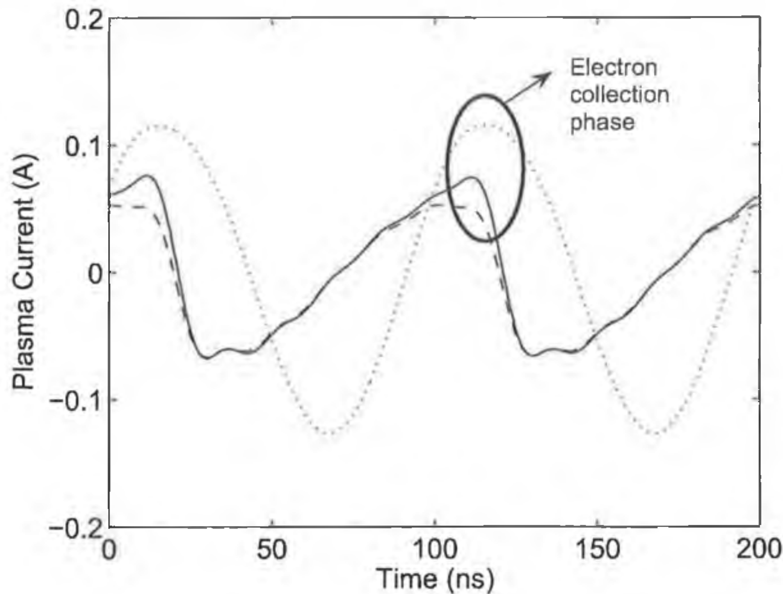

Figure 3.12: *Comparison of the current waveform at self bias (solid) with the current signal at the last point on figure 9 (dashed). A scaled down image of the electrode voltage is superimposed (dot) in the background to highlight the electron collection phase of the rf cycle.*

two points on figure 3.11 are given in figure 3.12 along with the rf component of the electrode voltage. The only notable effect on the current waveform is at the phase where electron loss occurs - the positive peak of the electrode voltage.

3.7 Summary

An experimental setup has been designed to allow the investigation of power coupling through capacitively coupled rf sheaths. The motivation being to investigate theoretical predictions that the electron loss component of the sheath current is important for stochastic electron heating models. Control

over electron loss at the end of the rf cycle, when the sheath edge reaches the electrode, is achieved by imposing an external negative dc bias on the electrode. The low operating pressure (1.4 mTorr) ensures that the capacitive sheath is collisionless. As the electrons are gradually removed from the total current an accompanying increase in power coupled through the sheath is noted. Comparing the current signals for the case with electron loss permitted and that with electrons most retarded it is clear that the increase in power is associated with the electron loss phase of the rf cycle only. This result clearly shows that the power increase is due to the removal of the electron collection as predicted by the PIC simulations of the same phenomenon. This result clearly indicates that electron loss in capacitively coupled plasma sheaths is not negligible as assumed in certain theoretical models. In order to obtain an accurate model for the collisionless heating phenomenon electron loss must be incorporated.

The experimental design presented is not limited to the measurements made here. It can be used for general electrical characterization of capacitive rf sheaths, both collisional and collisionless. Its non-perturbing nature, on the bulk plasma conditions, allows direct comparison with simulations performed in the same manner. The justification of this is presented in figure 3.9 where various bulk plasma parameters have been monitored throughout the biasing of the electrode and found to remain constant. This is not surprising since the power coupled to the plasma by the inductive source is 500 W while that coupled from the electrode is a fraction of 1 W. Finally we can assume that we have created a very planar sheath at the biased electrode since the sheath width (5 mm) is small compared to the electrode diameter (60 mm) which is again essential for direct comparison with simulation results that model a perfectly planar sheath.

CHAPTER 4

Electrical analysis of the sheath: A comparison with PIC simulations

4.1 Introduction

In chapter 4 measurements of the power dissipated to the electrons in the capacitive rf sheath are presented. In this chapter we look in more detail at the effect of the external dc bias on the rf sheath current and voltage waveforms. A PIC model developed to simulate a Langmuir probe in contact with a plasma discharge [35] has been used to make comparisons with the experimental measurements of current, voltage and power absorption and good agreement is found.

Another interesting phenomenon associated with low pressure capacitive sheaths is the presence of high frequency oscillations in the sheath potential [11, 62]. They are thought to be caused by an unstable electron en-

ergy distribution function (EEDF) with two maxima. One maximum for the heated electrons being pushed away by the sheath and one due to the cooler electrons that had drifted into the ion sheath during the time of collapse. These oscillations cause a modulation in the collisionless electron heating during the rf cycle.

These high frequency sheath potential harmonics are measured in the experiment with a floating probe positioned near the sheath, connected to a spectrum analyzer. The effect of dc bias control on the amplitude of these oscillations is examined. The PIC model also shows these high harmonic oscillations in the sheath potential and the effect of the dc biasing is consistent with the experimental results.

4.2 The particle-in-cell model

A one dimensional particle-in-cell (PIC) model is used to study the interaction of a planar electrode with an argon plasma discharge. The purpose of the model is to emulate the experimental setup and to explore the effects of the dc bias on the rf electrode. A PIC model is based on first principles and allows the researcher to study the plasma behavior by diagnosing discharge parameters which are inaccessible to the experimentalist. This technique is also known as computational experiment.

The model solves the Poisson equation in a one-dimensional grid which measures the distance of the planar electrode to the plasma. A space length of 5 cm from the electrode to the plasma bulk is modeled. The electrode is biased with a radio-frequency sinusoidal voltage at 10 MHz plus a dc voltage. The rf voltage is set as the voltage amplitude measured on the electrode by the current-voltage probe when the electrode is self-biased. The plasma

potential is set to 0 V while the self-bias of the electrode is determined by the cycle average electron and ion currents, i.e. it is set to the bias for which these currents are equal in value but with opposite sign. The model is run for various values of the dc bias to record its effect on the electrode currents and the plasma.

The electrons and ions are represented by particles while the neutrals are taken as a uniform background. Each computational particle (super-particle) represents thousands of real particles. It is necessary to set the super-particles due to the large number of real particles in a typical low temperature plasma. About sixty thousand particles were used on the simulation runs; it is important to set a large number of particles in order to reduce noise and produce more accurate results [63]. The particles position and charge determine the charge density which, combined with the boundary conditions, are used to solve the Poisson equation. The electric field is calculated from the potential and the particles are moved using a leap-frog scheme. The updated particles positions change the charge density and the cycle repeats. The basics of PIC modelling are presented in [22]. The background neutral gas pressure is set as in the experiment 1.4 mTorr. A certain number of particles experience a collision with the background gas each time step; Monte Carlo Collisions (MCC) [64]. Elastic and inelastic collision cross sections are used for both species to set the probability of each type of collision. The probability of a collision is also dependent of the particle energy and the background gas pressure. Particle-particle collisions are not included in the model used.

Electrons and ions are injected at the plasma bulk boundary. The particles velocities are randomly selected to be distributed according to a Maxwell-Boltzman distribution. The electron temperature and density are set to the values measured by the Langmuir probe. The ion temperature is set to

300 K. The electron and ion flux at the plasma boundary is regulated by the quasi-neutrality condition. The ion and electron flux are determined by the species temperature and plasma density but this alone does not ensure quasi-neutrality and therefore an additional flux on the species is added. This additional flux is determined by the potential over the last two grid cells at the plasma boundary; details of this approach can be found in ref [35] for a cylindrical geometry.

Note that in the work presented here one of the model boundaries is set as the plasma and that the plasma density, species temperatures and electron energy distribution are fixed at this boundary. This is to decouple the effect of the electrode on the plasma parameters, at the plasma boundary, in a similar way to that achieved in the experiment. Previous works have modeled a full capacitive discharge sustained by two electrodes [11, 17, 22, 32]. Gozadinos et al [3] developed a model to simulate a capacitive sheath in contact with a plasma. In this model two electron densities where imposed on the model, one to allow electron collection by the electrode and another to prevent it. Our approach is to allow the electrode self-bias, permitting electron collection, and subsequently setting different dc bias to gradually remove the electron current.

4.3 Cycle averaged ion and electron conduction currents

In section 3.6.4 the ion current to the electrode is determined from the dc electrode saturation current in the absence of the rf bias signal. The discharge is sustained under the usual conditions and the electrode is biased negatively. The negative bias is increased until the measured dc current no

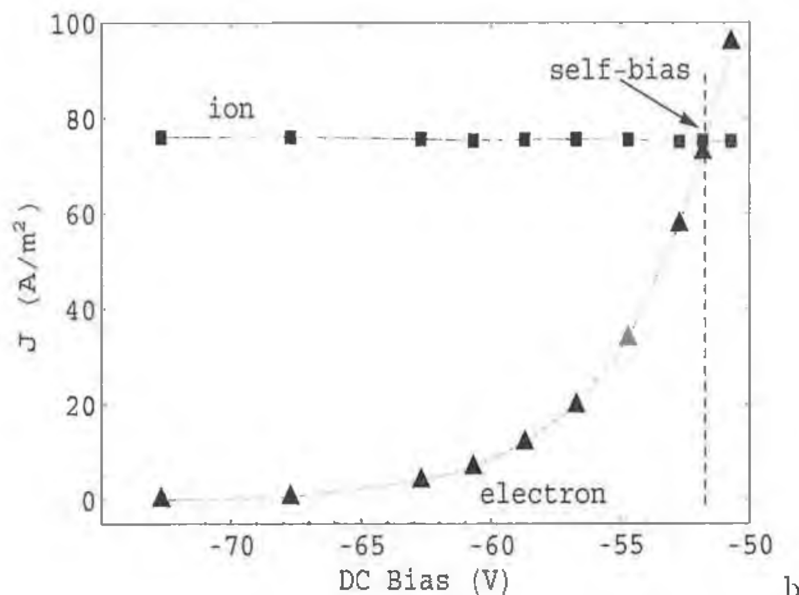

Figure 4.1: *Electron (absolute value) and ion cycle average current density (A/m^2) as a function of DC bias.*

longer increases but maintains a constant value - the dc saturation current. See figure 3.10 for a typical saturation current plot. The ion current to the electrode does not increase because the collection area does not increase with dc bias. The reason for the increase in current is that more and more electrons are repelled as the bias is increased. As the electrons are removed from the net current more and more of the constant ion current is revealed. The PIC model is used to verify this in figure 4.1. It is possible to measure quantities in such models that are not accessible in real experiments. Here the net current has been split into its individual ion and electron components. The ion current is constant while the electron current is removed with increasing dc bias steps. It shows two the self bias case where the magnitude of the ion and electron currents are equal given zero net current as they have opposite sign.

4.4 Phase resolved electron conduction current

The phase resolved conduction current (ion plus electron current) to the electrode has been estimated previously [38]. This estimation was based on Fourier analysis of the current waveform. The current waveform was separated into two components: one containing Fourier components with even symmetry about the peak of the sheath voltage, and the other with odd symmetry about the peak of the sheath voltage. Arguments presented by the author show that the even symmetry components sum to approximate the conduction current while the odd symmetry components sum to approximate the displacement current. The shape of the calculated conduction current is as expected with a constant dc level for the ions and a narrow spike for the electrons, which peaks at the most positive value of the sheath potential.

Our experimental setup allows an approximate measurement of the electron component of the conduction current. The rf bias is applied to the electrode and the dc bias is increased (negatively) to the point where there is zero net current through the resistor in figure 3.2. This corresponds to the normal self bias situation that would exist in the absence of a dc supply. The negative bias is then further increased until saturation of the net dc current is reached. The dc saturation means that the electron current has been removed. The current waveforms for both situations are recorded and the difference approximates the electron conduction current. A typical measurement is shown in figure 4.2. Again this is only an approximation as the increased dc bias on the electrode causes an increase in sheath width, which in turn causes a reduction in the displacement current. This is evident in figure 4.2 where the approximate electron current shows slight oscillation

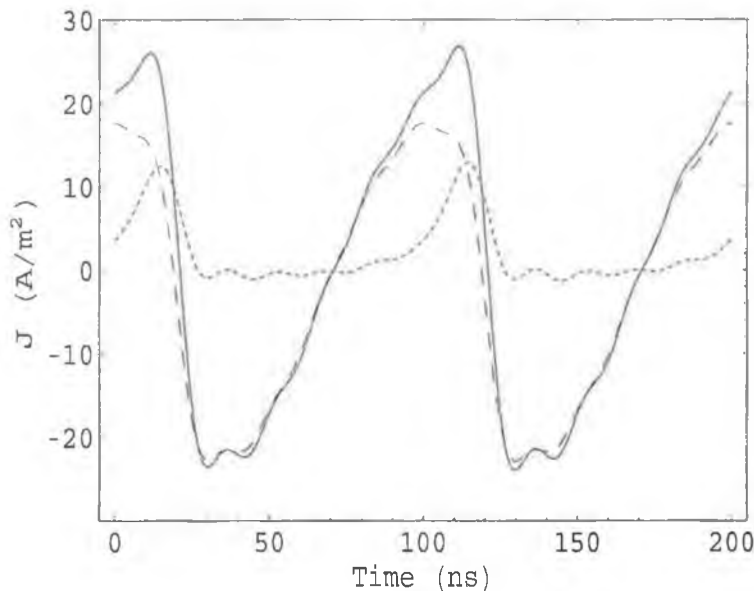

Figure 4.2: *Current waveform for the self biased case (solid), large negative bias case (large dash) and the approximate self biased electron current (small dash).*

about the zero line.

The simulated current waveforms show good agreement with those measured in the experiment. In figure 4.3 waveforms are given for a) the self bias case and b) the case when a large negative bias is imposed to repel electrons. The main difference is that the simulation shows a high frequency oscillation that is not detected in the experiment. There are a number of reasons why this high frequency component is not detected in the experiment. Firstly the bandwidth of the current probe/oscilloscope combination is such that the frequency response falls off rapidly above 60 MHz. The high frequency component visible in figure 4.3 is greater than 100 MHz and will therefore be attenuated by the measurement device. The second reason is that the very high frequency currents see a relatively easy path to ground from the electrode to the chamber wall and very little passes back down the rf line for

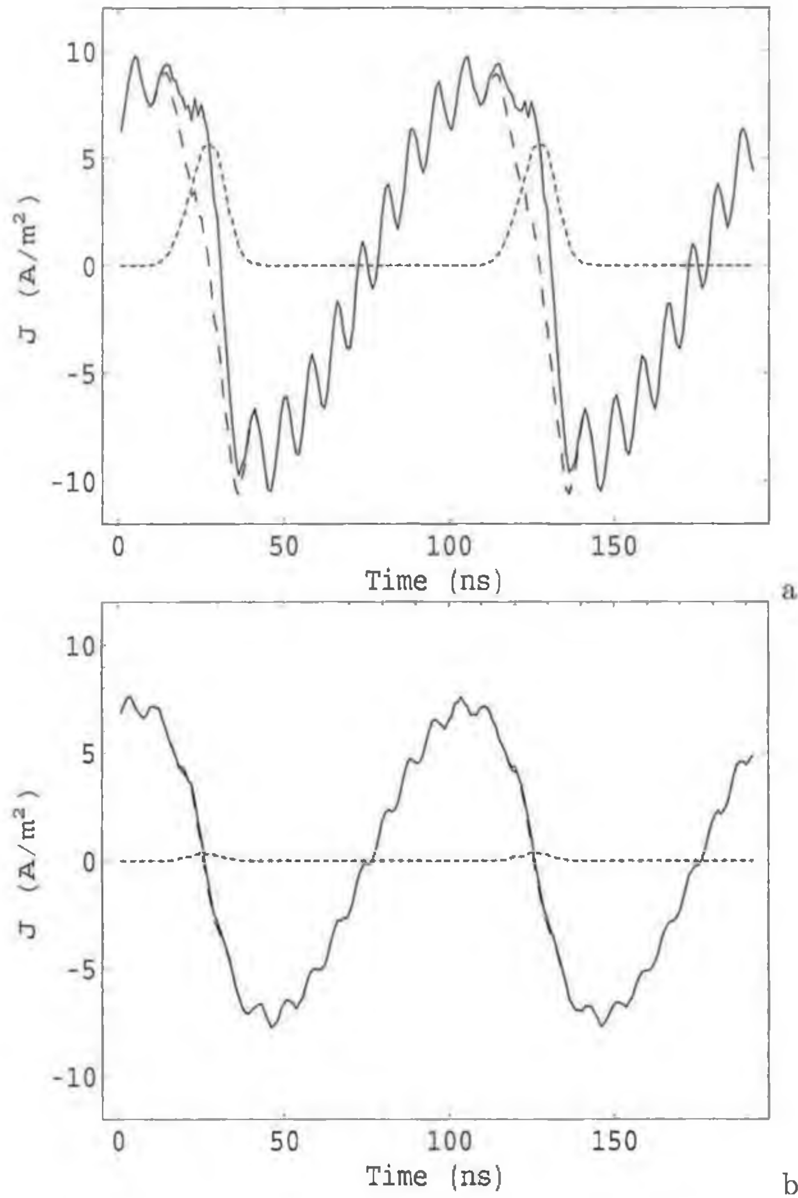

Figure 4.3: *Electron and displacement current density (A/m^2) at the electrode for a self biased electrode (a) and a negatively biased electrode (b); profiles shown over two periods.*

detection.

Ignoring the high frequency oscillation it is clear that the measured and simulated waveforms are very similar. The electron conduction current waveform is also very similar, occurring at the same phase and having similar magnitude relative to the total waveform. In figure 4.4 the electron current waveforms are plotted as a function of dc bias from both the experiment and simulation. In the experiment these waveforms are obtained by subtracting the total current waveform at the largest negative bias from each of the other waveforms at the other dc bias levels. The reason for this is that the waveform at the largest negative dc bias is the waveform with the total electron current removed. In other words this waveform is the displacement current plus the ion current. The only difference between this waveform and the others is the amount of electron current collected at each bias and hence the subtraction to find the electron currents. The results of the simulation for similar conditions again compare very favorably.

4.5 Power absorption

The total power absorbed in the sheath is split between the ions and electrons. The ions absorb power as they are accelerated to the electrode by the time average sheath potential. The electrons that interact stochastically with the instantaneous sheath potential also absorb power. Some electrons arriving from the bulk plasma have sufficient energy to cross the sheath potential barrier and loose power. The power absorbed by the ions, P_{ion}, is calculated from

$$P_{ion} = V_{dc} I_0, \tag{4.1}$$

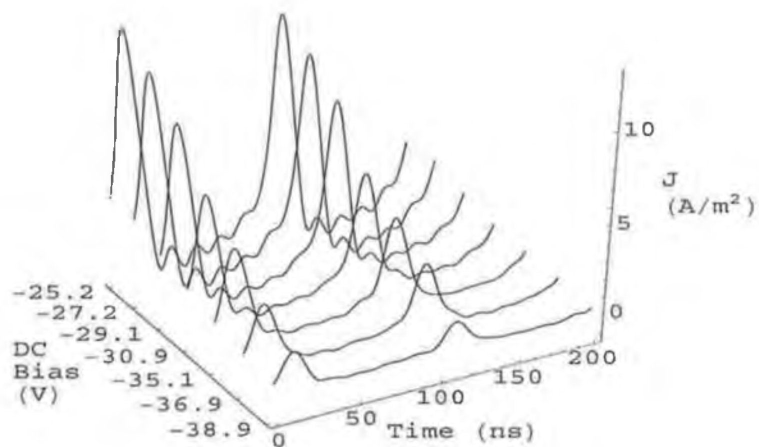

a

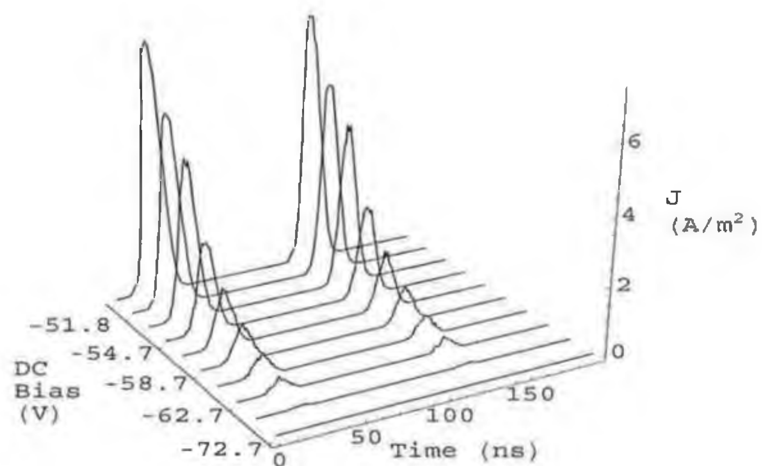

b

Figure 4.4: *Electron conduction current waveforms as a function of DC bias from a) the experiment and b) the PIC simulation.*

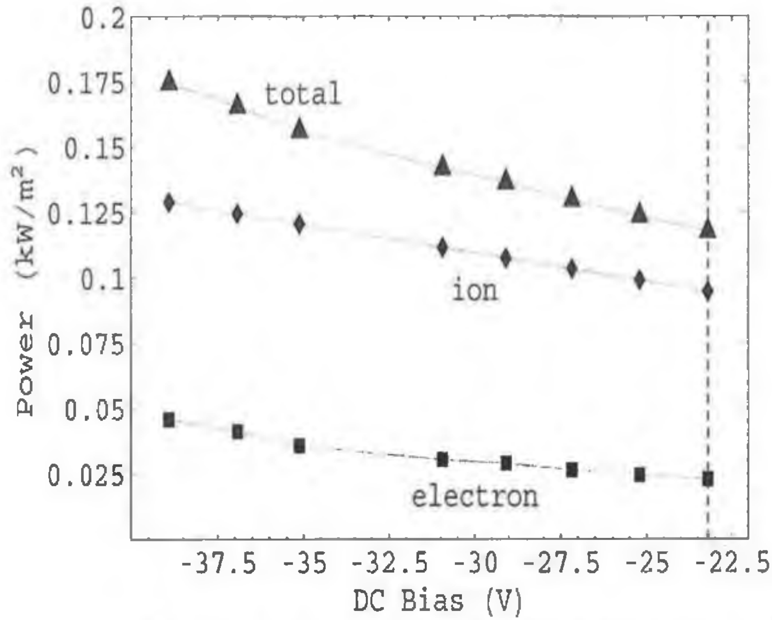

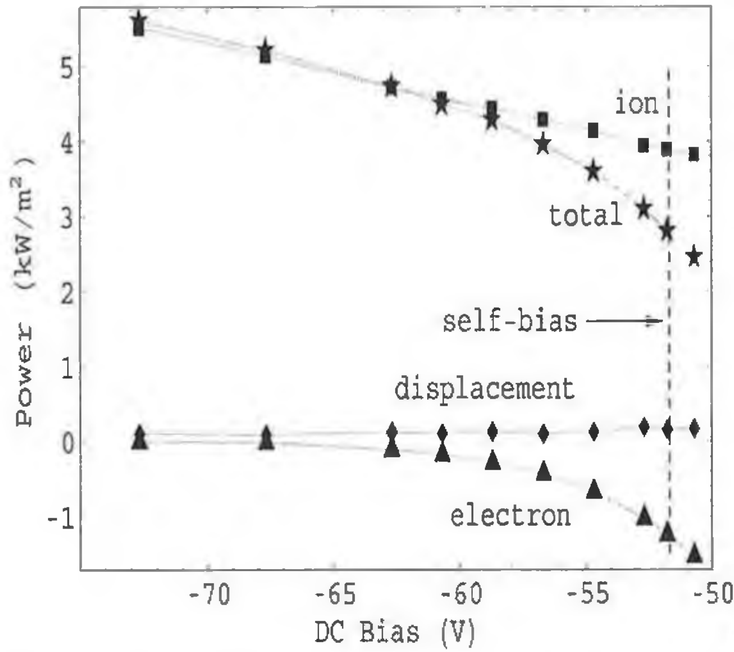

Figure 4.5: *a) Total power dissipated in the sheath (triangle) as a function of DC bias, separated into the ion power (diamond) and the total electron power (square). b) Cycle average power absorption (kW/m^2) associated with the electron, ion, displacement and total current as a function of DC bias.*

where V_{dc} is the dc component of $V_{ps}(t)$. The total power absorbed by the electrons, $P_{electron}$, is simply the difference between total and ion power

$$P_{electron} = P_{total} - P_{ion}. \tag{4.2}$$

The electron power can also be split into two components, that dissipated through stochastic heating and that associated with electron loss to the electrode. It is generally assumed that the electron loss component is negligible as the electrons only reach the electrode when the electrode potential is close to that of the plasma. To investigate this an experiment has been designed to allow gradual removal of the electron loss to the electrode. The electron power is calculated, starting at the electrode self bias and then at various additional dc bias steps towards ion saturation. The power absorbed by the ions increases as expected. The ion current does not increase but the bias voltage does - hence the ion power increase. The electron power also increases but for a different reason. As the bias is increased the electrons that previously had sufficient energy to cross the sheath to the electrode are now gradually repelled. If these electrons no longer reach the electrode they can no longer remove their energy from the system. As previously reported [65] the stochastic heating component of the electron power does not seem to be significantly effected by the additional biasing. The increase in total electron power is therefore better explained as a decrease in the electron loss component of the total electron power. In figure 4.5 the power absorption from both the experiment and PIC simulation are compared. In figure 4.5a the labels total, ion, and electron refer to the cycle average total power, ion power and total electron power respectively. Total electron power means the combination of electron loss power and collisionless heating power. The use of the PIC simulation allows a more detailed analysis of the individual power components. In figure 4.5b the labels total, ion, electron, and displacement

mean the cycle averaged total power, ion power, the electron loss power, and the power dissipated by the displacement current (the collissionless heating power) respectively. Both simulation and experiment show the same trends, the total, ion and electron power increase with increasing dc bias. An interesting point to note from the PIC results is that the collisionless electron power component remains more or less constant at all bias levels. This reinforces our earlier suggestion that the total electron power increases because electron loss decreases rather than because collisionless heating increases.

Even though quantitatively the PIC values are somewhat different, qualitatively the trends are very similar. The reasons for discrepancies between model and experiment are twofold: 1) The model simulates a perfectly one-dimensional sheath whereas there are likely to be edge effects in the experiment making the sheath deviate somewhat from the one-dimensional case. 2) In the simulation the electrode bias does not effect the plasma parameters and plays no role in sustaining the plasma, however in the experiment the plasma in the immediate vicinity of the electrode sheath will be influenced by the electrode bias. The second reason seems to explain the apparent total power loss by the electrons at the self bias point in figure 4.5b. The electron power loss is larger than the collisionless heating power. However in the experiment we see clear net power gain by the electrons as is the case in normal capacitive discharges at low pressure.

4.6 High frequency sheath potential oscillations

High frequency oscillations are known to exist in the time varying sheath potential at low pressures [11, 62]. These oscillations occur near the instan-

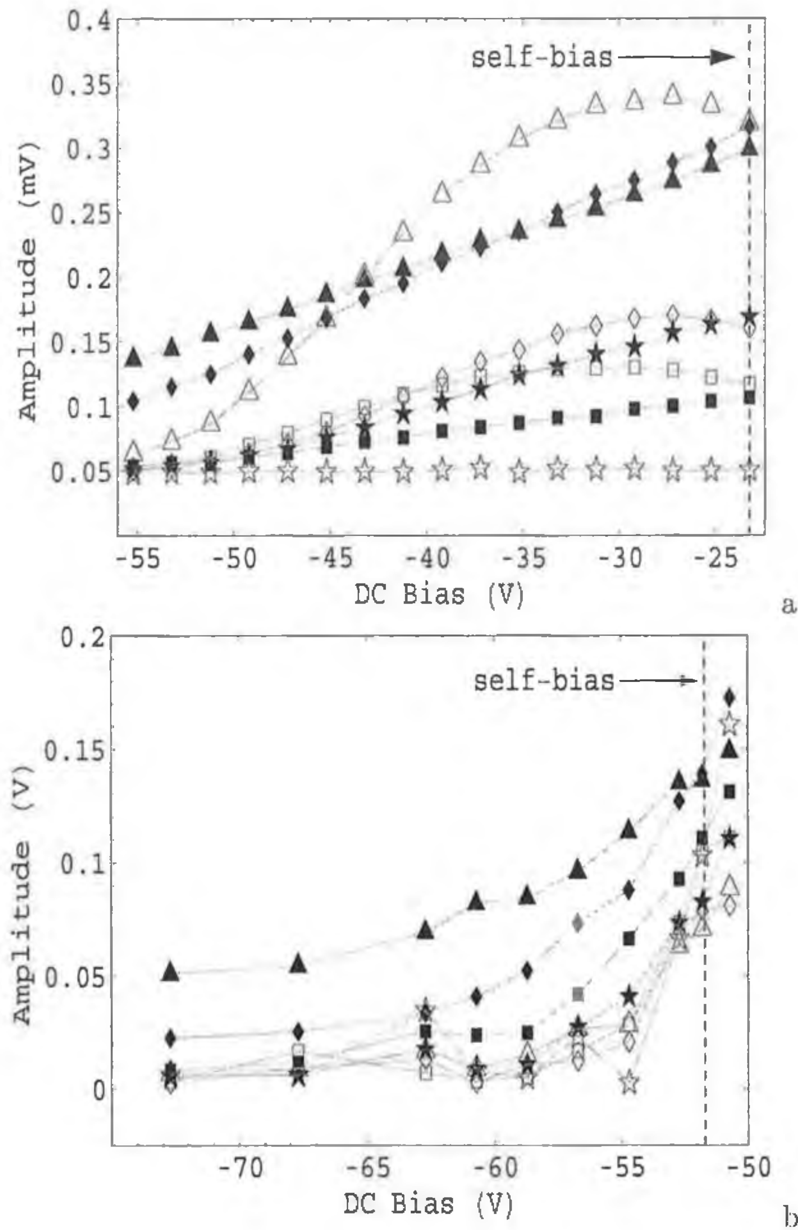

Figure 4.6: *Voltage amplitude of harmonics of the space potential in the sheath as a function of DC bias from a) the experiment and b) the simulation. Filled triangle, diamond, box and star corresponding to second, third, fourth and fifth harmonics respectively and unfilled triangle, diamond, box and star corresponding to sixth, seventh, eight and ninth harmonics respectively.*

taneous sheath edge and can in principle impart energy to the electrons. These oscillations have been monitored in the present experiment using a floating probe mounted close to the ion sheath edge. The probe output is connected directly to a spectrum analyzer. Only harmonics of the bias frequency (10 MHz) are investigated. The relative amplitudes of the second through ninth harmonics are determined as a function of dc bias applied to the electrode. A plot of the amplitude variation of these harmonics as a function of bias is given in figure 4.6. The general trend is that the harmonic amplitudes decrease with increasing negative bias. If these high frequency oscillations contribute to the stochastic electron power absorption this result would indicate that the imposed dc bias reduces the stochastic component of the total electron power absorption. However a previous PIC simulation [3] suggests that, even though there is clear instantaneous power dissipation associated with these oscillations, the power dissipated in an average sense is not significant. This finding is in agreement with the result presented in figure 4.5. If the stochastic component of the total electron power absorption is decreasing with applied bias its effect is much less significant than the electron loss power. The prevention of electron loss is accompanied with an increase in total electron power. This indicates that any decrease in stochastic power absorption is small compared to the total electron power gain (due to the removal of electron loss). It is difficult to isolate the stochastic power component from the electron loss power component in the experiment. The PIC model is therefore used to look at the these two power components separately. As discussed in the previous section the collisionless power component remains fairly constant as a function of dc bias. This reiterates the idea that the high frequency oscillations do not greatly effect the power absorption in an average sense.

In figure 4.7 and figure 4.8 the sheath electron density profile and sheath potential profile are given for both the self bias case and the large negative bias case. The main interesting feature of the two density profiles is the change from collecting electrons when the sheath has minimum width in the self biases case to no electron collection for minimum sheath width in the large bias case. There is also a slight density modulation in the density profile but it is quite small and difficult to see in these figures. The high frequency oscillations are clearly visible in the sheath potential profiles. The main difference between the two potential profiles is the damping of the oscillations at large dc bias. Finally the power absorption as a function of phase is plotted in figure 4.9. Dark areas denote power absorption and light areas denote power loss by the electrons. The instantaneous electron power absorption associated with the higher harmonics is clearly visible in both but heavily damped in the large negative bias situation.

4.7 Summary

A detailed comparison has been made between experimental measurements and PIC simulations of the electrical characteristics of the capacitive rf sheath. The cycle average ion and electron currents as a function of dc bias from the simulation show clearly how the experimentally determined ion saturation curve develops. It is not due to an increase in ion current as the bias is increased, it is due to the gradual removal of the electron current as the bias increases. The total ion current is independent of bias and remains constant in the dc bias range investigated.

An approximate measurement of the electron conduction current has been obtained from the experimental results and compares well with the same

current obtained from the simulation. The electron current waveform shows a spike at the most positive value of the sheath potential as expected. It shows the expected exponential rise and decay at either side of the peak of the sheath potential. This waveform could potentially be used as a diagnostic to obtain the electron temperature in the plasma but more work is required to verify this prediction. The electron current waveforms have been calculated for various dc bias and compared with the PIC and show the amount of electron current removed at each step. Again excellent qualitative agreement is found.

The instantaneous power absorbed by both ions and electrons measured in the experiment have been compared with similar results from the PIC. The prediction from chapter 4 is that the increase in total electron power is actually caused by a decrease in electron loss power. This is confirmed by the simulation where it has been seen that the electron loss power does in fact decrease with increasing dc bias while the collisionless heating power remains constant, leading to the total electron power gain.

The high frequency sheath potential oscillation reported by other authors have been investigated using a floating probe mounted close to the sheath edge. The second through ninth harmonic amplitudes have been recorded as a function of dc bias. These harmonic amplitudes are significantly reduced with increasing dc bias. The same trend was observed in the PIC model. These high frequency oscillations does not appear to greatly effect the collisionless heating as predicted in previous work. This observation is made by noticing that the collisionless power remains constant over the range of applied dc bias even though the high frequency oscillation are significantly reduced.

The PIC simulation is run using the experimentally determined plasma parameters as inputs. The electrode rf bias is set to the value applied in

the experiment also. It can be seen, by comparing figures 4.2 and 4.3, that the total rf current obtained from the PIC is a factor of two greater than in the experiment and has a knock on affect on the other results compared. The experiment and simulation provide a good basis for the comparisons made yet the factor of two in rf current exists. This may indicate that the experimentally determined plasma parameters, used as inputs to the simulation, cause the discrepancy. It could also indicate that the one dimensional, planar, simulation is too far from reality to make quantitative comparisons with the experiment. However, there is now the possibility of tuning the experiment and simulation to give good quantitative agreement. This would serve as a very powerful tool for validating sheath models.

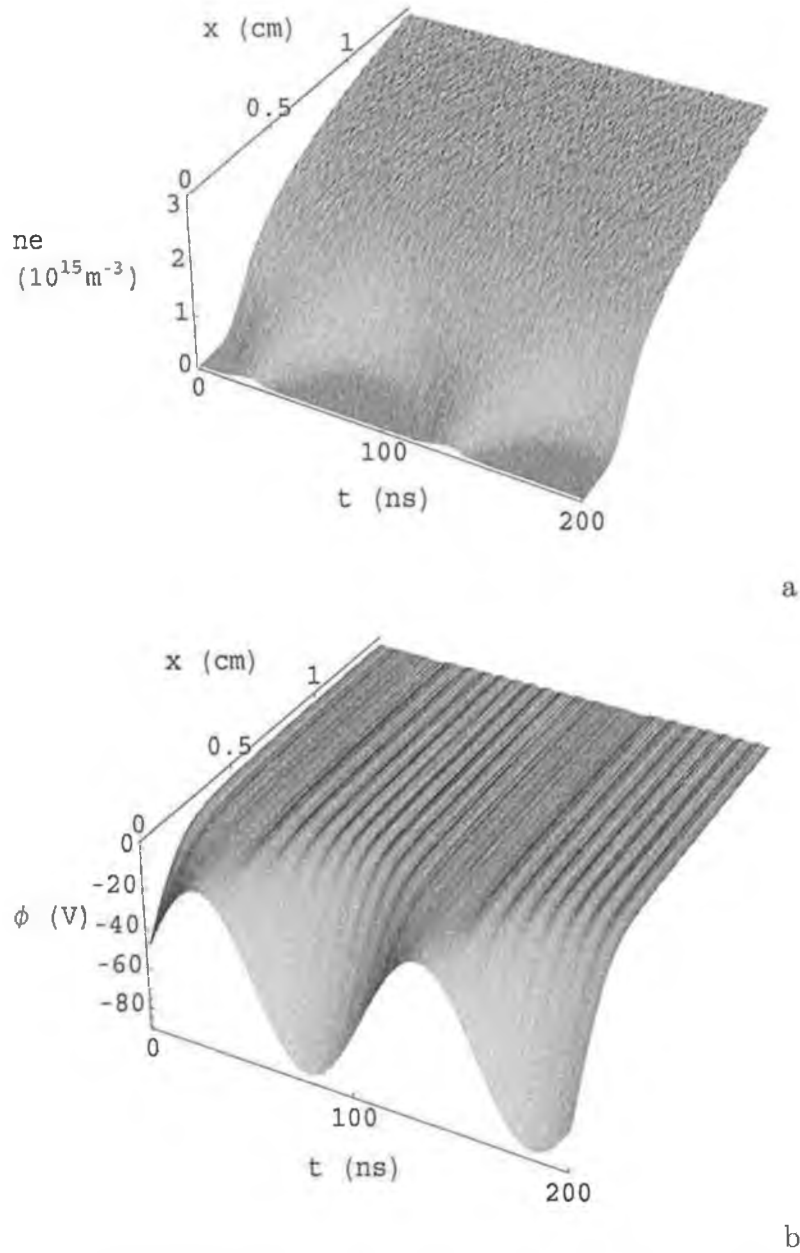

Figure 4.7: *Electron density (a) and space potential (b) for a self biased electrode; profiles shown over two periods.*

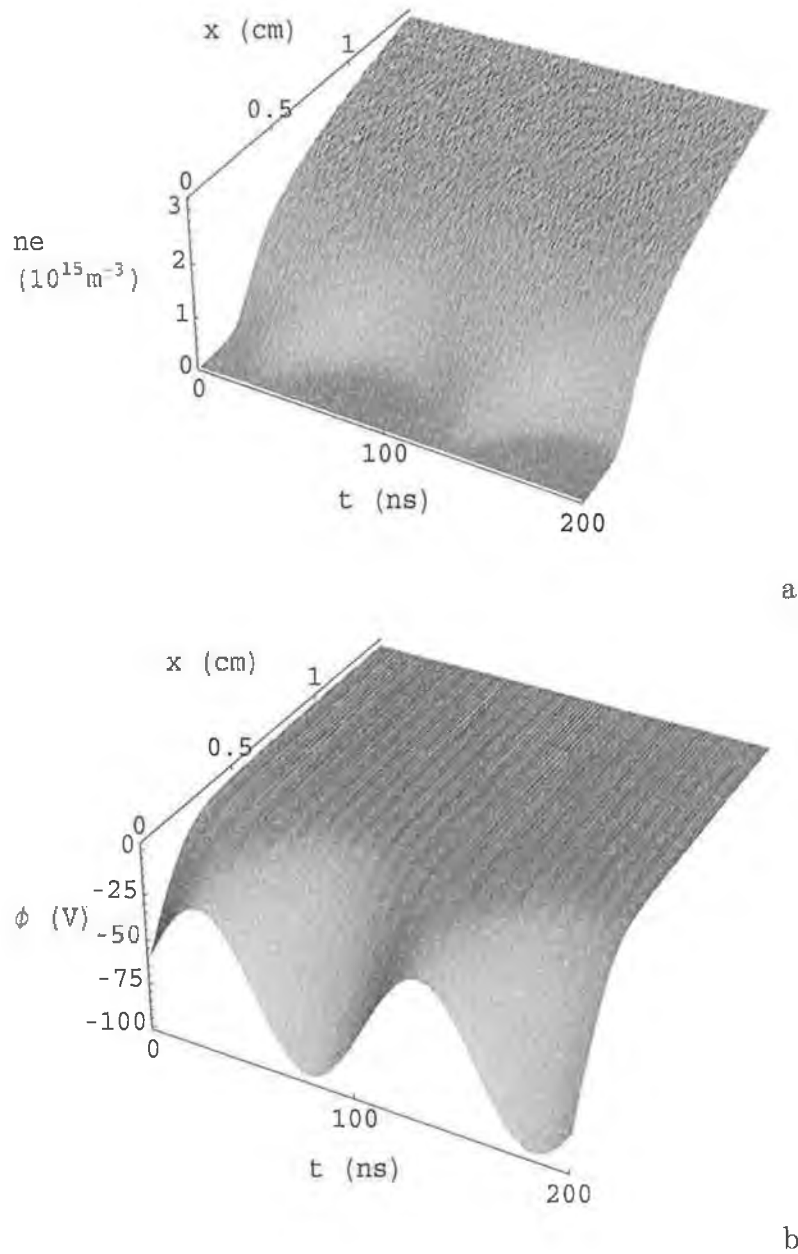

Figure 4.8: *Electron density (a) and space potential (b) for a negatively biased electrode; profiles shown over two periods.*

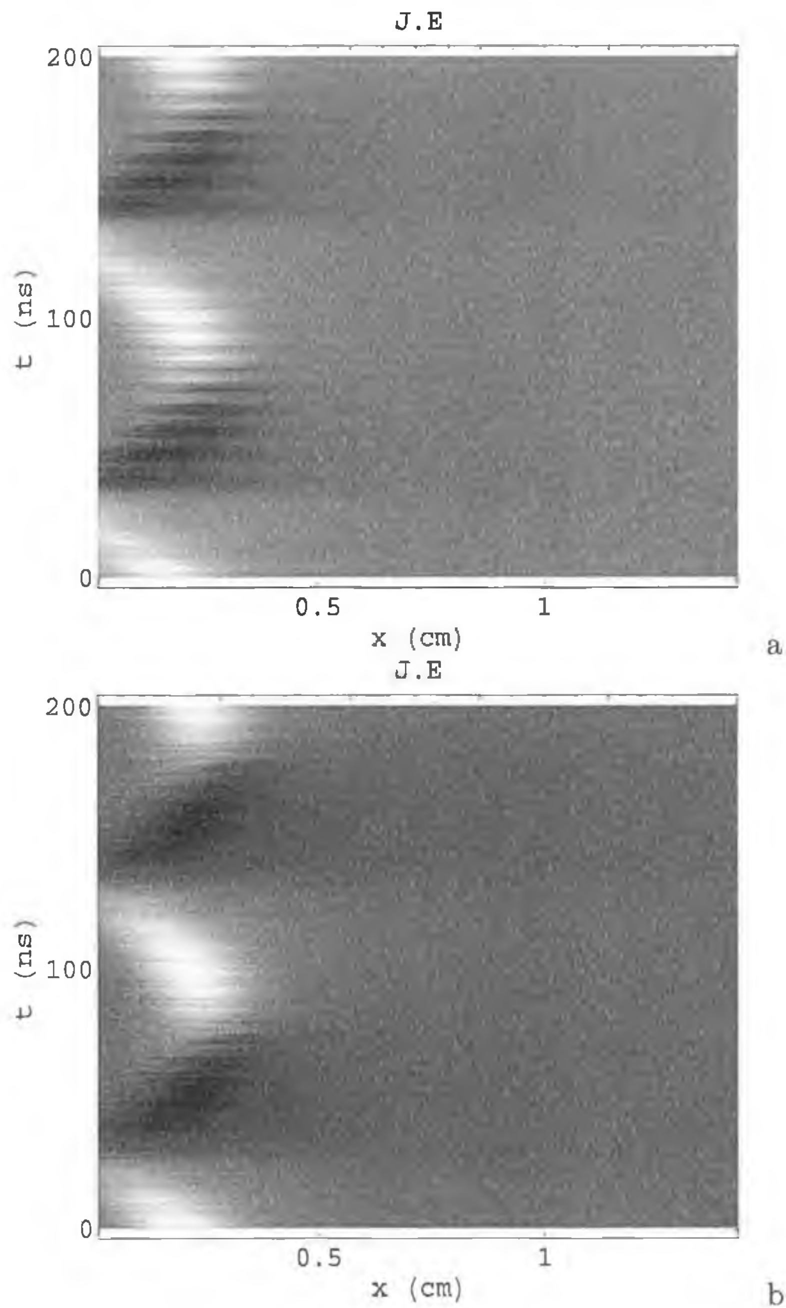

Figure 4.9: *$J \cdot E$ product density plot for a self biased electrode (a) and for a negatively biased electrode (b); profiles shown over two periods. Dark areas denote power absorption by the electrons, light areas denote power loss.*

CHAPTER 5

A novel wide-band rf power sensor

5.1 Plasma discharge power measurement

In general, rf power is not supplied directly to a plasma discharge because of the mismatch between source and load. For this reason a matching unit is placed between the source and discharge and tuned such that the load impedance equals the source impedance - the condition for maximum power transfer efficiency. Conventionally the power absorbed (P_{abs}) by the discharge is measured using an inline directional power meters positioned between the source and the matching network. The power meter determines the forward and reflected power (P_f and P_r respectively) with the difference equal to P_{abs}. It is not always possible to operate in a perfectly matched situation and the performance of these directional devices deteriorates because of directivity and load mismatch issues [66].

Another common method for discharge power measurement uses *in situ* current and voltage (*I-V*) probes. They are mounted as close as possible to the capacitive electrode [36, 37, 39, 67] or inductive coil of the [40, 68] discharge, and power delivered is calculated from the product of rf current, voltage, and cosine of the relative phase (θ) between them

$$P_{abs} = IV \cos\theta. \tag{5.1}$$

The use of proprietary [37, 39] and homemade derivative probes [36, 40] have been reported with varying degrees of success. Very precise determination of θ is necessary due to the highly reactive ($\approx \frac{\pi}{2}$) impedance of most discharges. It has been shown [67] that for a realistic case where $cos\theta = 0.05$ and with a phase resolution of 2° the uncertainty in the power calculation is 70%. Phase resolution of 2° is common when calculating relative phase by comparing zero crossing points in the time domain. This limited resolution arises from noise and harmonic distortion of the waveforms being analyzed. Phase resolution can be enhanced with the use of fast Fourier transforms (FFT's) which can isolate the phase at the fundamental frequency and a resolution of 0.05^o has been reported [67]. A thorough description of how to achieve accurate current, voltage and phase measurement can be found in the literature by Godyak, Piejak, and Alexandrovich [20, 67, 69].

5.2 Standard directional power meter

The most common method used to measure the rf power delivered to a plasma discharge uses non intrusive directional couplers mounted in the transmission line between the generator and the matching unit. These devices are designed with characteristic impedance (Z_0) equal to that of the transmission cable

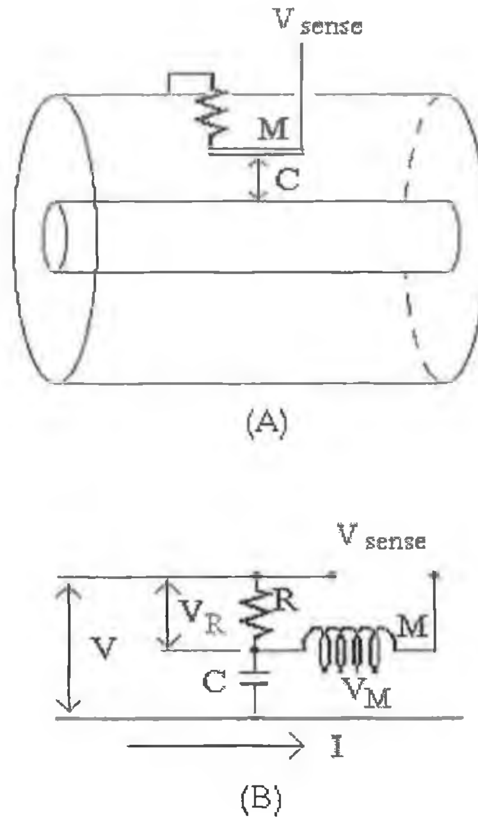

Figure 5.1: *Schematic of a standard power meter structure with its equivalent sensing circuit.*

(50Ω in most cases) and sample separately the power traveling toward and reflected from the discharge.

This type of sensor [70] has a co-axial structure with the power flowing through the inner conductor and the sampling circuit mounted in the grounded shielding. Designs generally consist of either a rotatable sensing element which can be orientated to sample signals in either direction, or two sensing elements in series to sample both directions simultaneously. A schematic with its equivalent sensing circuit is shown in figure 5.1.

It consists of a mutual inductance (M), between the loop and the inner

conductor, to sample the line current (I) and a voltage divider (C and R) to sample the line voltage (V). The sensing circuit can be rotated to give positive or negative M with respect to the direction of current flow in the through line. The output (V_{out}) is the sum of two signals, V_R and V_M

$$V_R = j\omega RCV \tag{5.2}$$

and

$$V_M = j\omega I(\pm M). \tag{5.3}$$

Component values are chosen such that $R \ll C$ and

$$CR = \frac{M}{Z_0}. \tag{5.4}$$

Summing (5.2) and (5.3) and substituting (5.4) gives the output

$$V_{out} = (V_R + V_M) = j\omega M \left(\frac{V}{Z_0} \pm I\right) \tag{5.5}$$

At any point on the transmission line the voltage is the sum of the forward and reflected voltages (V_f and V_r respectively) while the current is the difference between the forward and reflected currents (I_f and I_r respectively). Thus for positive M, (5.5) becomes

$$V_{out} = j\omega M \left(\frac{V_f + V_r}{Z_0} + \frac{V_f - V_r}{Z_0}\right) \tag{5.6}$$

Finally (5.6) can be written as

$$V_{out} = \frac{j\omega M}{Z_0}(2V_f) \tag{5.7}$$

showing that the sensed output is directional and proportional to the forward voltage on the line. Similarly it can be shown that for the opposite direction when M is negative the output is written as

$$V_{out} = \frac{j\omega M}{Z_0}(2V_r). \tag{5.8}$$

In a commercial system the output signals are filtered, rectified and displayed on a meter calibrated in rf watts.

5.3 Associated errors

As discussed in the previous section, a directional device is required to separate the forward and reflected signals on a transmission line carrying rf power to and from a particular load. The accuracy of these measurements is limited by both the directional device and the system in which it is applied. Two main sources of error have been identified for such devices.

5.3.1 Error due to directivity

All directional devices have an error associated with the inability to completely isolate a signal in a particular direction from that in the opposing direction and is defined as the device's directivity.[1]

Considering a directional device whose output is terminated with an ideal Z_0. Therefore, all of the transmitted energy is absorbed in Z_0 and none is reflected back through the device. However there will be an output at the reflected measurement port reduced by X dB from a full reflection where X dB is the directivity of the particular device. The directivity signal arises from deviations from the ideal within the device. In other words it is impossible to remove all contributions from the undesired signal direction to the measured signal. Higher directivity in a device means less contribution from the undesired signal.

[1]Directivity is defined as the difference in dB of the power output at a coupled port, when power is transmitted in the desired direction, to the power output at the same coupled port when the same amount of power is transmitted in the opposite direction.

5.3.2 Error due to test port mismatch

The second measurement error arises from the test port mismatch at the measuring port. The measuring port is the output port of the directional coupler to which the load is connected and the mismatch is caused by connectors having slightly different characteristic impedance than Z_0. Assuming an ideal open or short circuit termination, all the power incident at which is entirely reflected, a reference signal is registered at the reflected-measurement port. Some of the actual reflected power has however been re-reflected due to the test port mismatch. This reflected power returns to the open or short where it is fully reflected again. This signal also contributes to the measured output and depending on its relative phase can increase or decrease the initial signal. Test port mismatch can result in a calibration error which could be significant unless care is taken to minimize the mismatch level.

5.4 A new design

Our sensor design [71] combines ideas from directional coupler theory and $I - V$ probe techniques, with the advantage that it can be used as either an in-line directional power meter or a current and voltage sensor. It is designed to have a wide band response and is suitable for fundamental and harmonic power measurements. Instead of making the measurements directional we sample the total rf current and voltage signals along with their relative phase at a particular point on a transmission line.

5.4.1 Mechanical design

The sensor design is illustrated in figure 5.2. It has a 50Ω co-axial through line structure with two sensing elements used to sample the signals on the

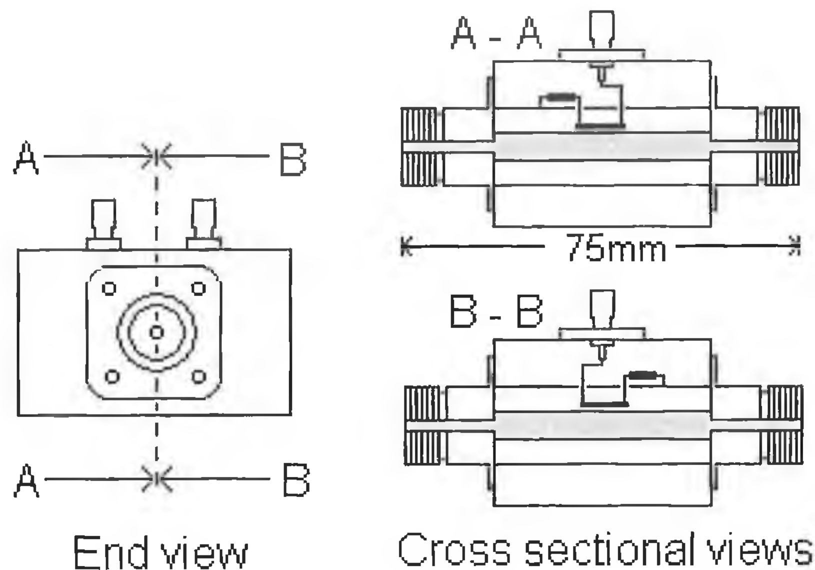

Figure 5.2: *Schematic of sensor construction. The rf connectors are female N-type and the output connectors are female SMA.*

inner conductor. The ratio of the diameters of the inner conductor (d), grounded shielding (D), and the dielectric constant (k) of the spacer (air in this case) defines the sensor's characteristic impedance (Z_0)

$$Z_0 = \frac{138}{\sqrt{k}} \left(log \frac{D}{d} \right). \tag{5.9}$$

The sensing elements' equivalent circuits are shown in figure 5.3. They are mounted side by side at the same position on the through line. They consist of a resistive-capacitive voltage divider to sample the local rf voltage and an inductive loop to sample the local rf current. The capacitive pickup forms the bottom edge of the rectangular loop, and therefore current and voltage measurements are made at exactly the same position, which is essential if accurate phase measurements are to be made.

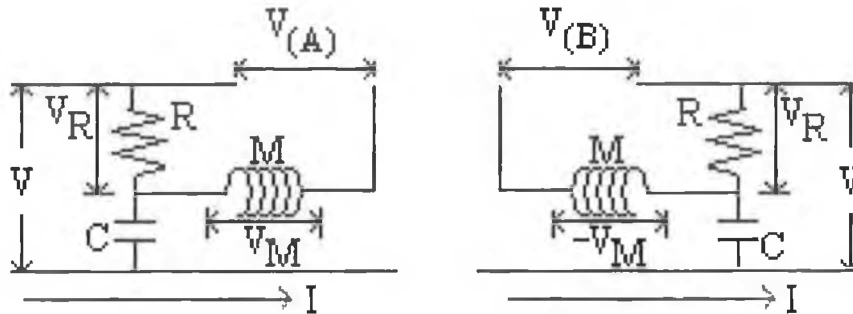

Figure 5.3: *The sensing elements' equivalent circuit showing the opposite orientation of the two mutual inductances (loops).*

5.4.2 Theory of operation

The difference between the two sensing elements in our device is in the orientation of the inductive loops with respect to the direction of current flow on the main line. One is set to generate a positive voltage and the other a negative voltage due to the same magnetic field threading both loops. It was shown in section 5.2 that the output signal $V_{(A)}$ is equal to $V_R + V_M$ which is proportional to $V + I$ and that $V_{(B)}$ is equal to $V_R - V_M$ proportional to $V - I$. Addition and subtraction of these two measured signals yields current and voltage signals proportional to the actual current and voltage on the through line. A complexity arises due to the inherent difficulty in physically constructing identical inductive loops (M) and capacitive pickups (C) for both circuits, resulting in different voltage and current scaling factors for each sensing element. The sensed signals are therefore more accurately defined as

$$V_A \propto (V + I) \tag{5.10}$$

and

$$V_B \propto (\alpha V - \beta I), \tag{5.11}$$

where α accounts for the difference in sensed voltage and β the difference in sensed current due to unequal C and M, respectively. The constants α and β are independent of frequency as the ratios of inductive and capacitive reactance remains constant for all frequencies, i.e., C and M (although slightly different) are fixed in both elements.

To determine α the current signal contribution is removed using an open-circuit termination at the output end of the sensor. A plot of $V_{(A)}$ vs $V_{(B)}$ yields a straight line whose slope is α. Similarly to find β the voltage contribution is removed using a short-circuit termination and the same procedure is applied. Solving (5.10) and (5.11) simultaneously yields signals proportional to the line voltage and current

$$V \propto \left(\frac{\beta V_{(A)} + V_{(B)}}{\alpha + \beta} \right) \tag{5.12}$$

$$I \propto \left(\frac{\alpha V_{(A)} - V_{(B)}}{\alpha + \beta} \right) \tag{5.13}$$

Before implementing this calculation to find scaling factors for the sensed V and I signals, propagation delays introduced by cables used to convey the signals to the measurement device need to be accounted for.

5.5 Sensor calibration

5.5.1 Propagation delay

Propagation delays associated with cable lengths cause a phase error between the signal at the measurement point and that at the measurement device. A cable time delay Δt will shift the phase of a signal at frequency f by an amount $\Delta\theta$, where $\Delta\theta = (360^o) f \Delta t$. The experimental setup used to calibrate for phase delays is shown in figure 5.4. An oscilloscope/attenuating voltage

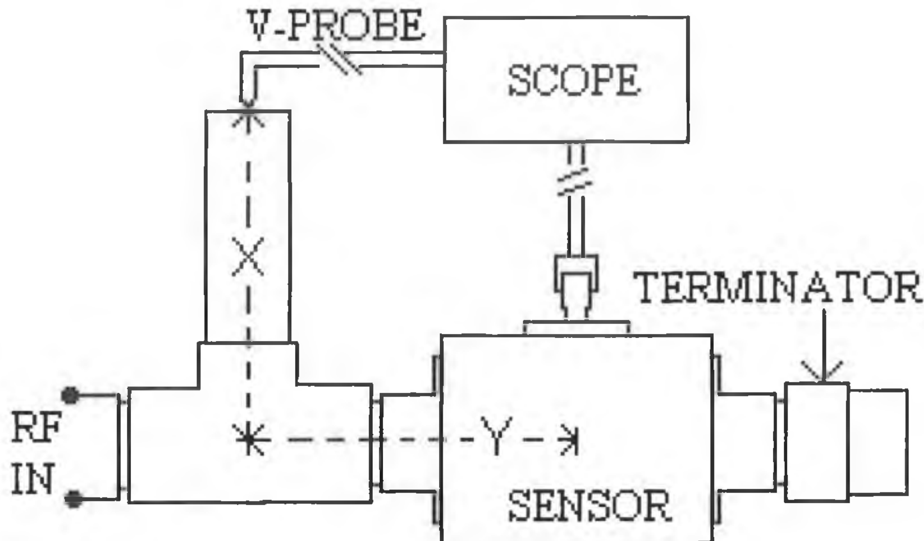

Figure 5.4: *Setup for phase calibration showing the use of the "dummy line" to find the phase at the sensing element location*

probe combination with a bandwidth of 300 MHz and an accurate 50Ω (dc to 3 GHz) terminator are used in the calibration for a desired frequency range of 10 – 70 MHz. The attenuating voltage probe was pre-calibrated for propagation delays using the method prescribed by Sobolewski. The phase error of the probe is measured by connecting the probe tip directly to one channel of an oscilloscope and connecting the output to a second channel. By applying sinusoidal signals at varying frequencies to the probe tip and measuring the phase difference between the two oscilloscope channels a plot of phase error as a function of frequency can be made. The time delay is then obtained from the slope. The rf sensor output signal phases are referenced to this probe. The reference voltage probe phase error is shown in figure 5.5. The phase error is linear with frequency and for this case the time delay is found to be 6.02 ns. The linear nature of the graph implies that this

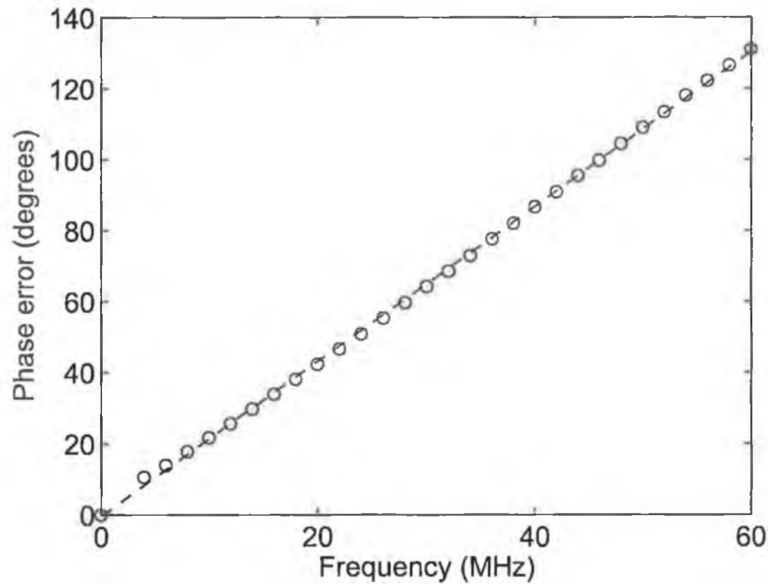

Figure 5.5: *Reference voltage probe phase calibration*

particular voltage probe is dispersionless i.e. the time delay introduced by the probe does not vary with frequency.

The physical construction of the sensor does not permit mounting of the voltage probe directly beneath the sensing elements. To overcome this issue a 50Ω T-junction connector was used at the input of the sensor and a length od 50Ω cable was inserted perpendicular to the main line such that length X equals length Y as shown in figure 5.4. The phase measured at the end of this "dummy line" equals the phase at the sensing element location.

The 50Ω termination provides the convenient situation that the through-line current and voltage are in phase. The voltage dropped across the resistor ($RCdV/dt$) and the voltage generated in the loop (MdI/dt, where M is the mutual inductance between the loop and the through-line) are both derivative signals, and although being 90° out of phase with the reference signals their

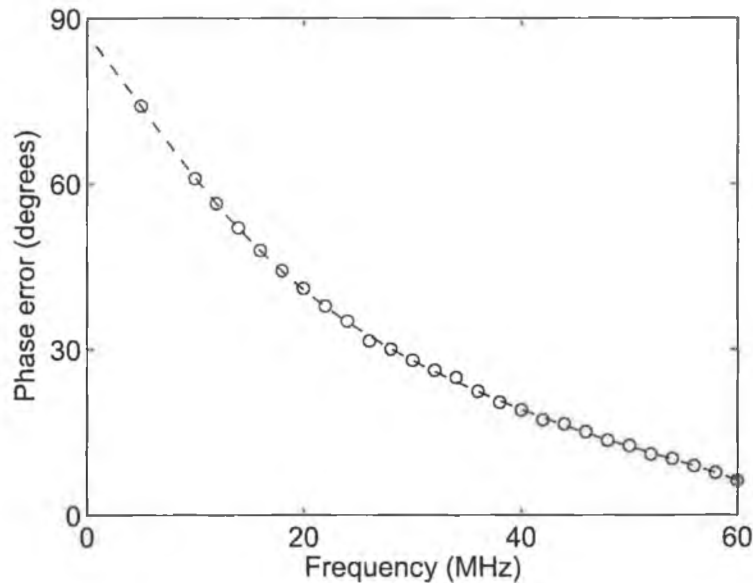

Figure 5.6: *Phase errors associated with sensor cabling and oscilloscope input impedance. Circles represent the measured data while the dashed line is a* 6_{th} *order polynomial fit.*

relative phase is equal to that of the reference signals. Consequently, the sensed signals $V_{(A)}$ and $V_{(B)}$ must be in phase when the 50Ω terminator is used. This provides an accurate operating point for phase calibration.

The sensor output signals are digitized by the oscilloscope and transferred to a personal computer (PC), where a suite of programs have been designed to extract accurate phase and amplitude information. The phase delay as a function of frequency for both sensed signals is obtained using the voltage probe as the reference phase measurement. The phase error introduced by one of the cables is shown in figure 5.6. The data is fitted with a 6th order polynomial equation which accurately calculates the phase at any frequency in the given range. The fact that the data can be described by a single equation facilitates ease of implementation in the phase error correction program.

A fast Fourier transform (FFT) algorithm transforms the data to the frequency domain where the relevant components are corrected for these phase errors.

In figure 5.5 the phase error introduced by the cable increases with increasing frequency as expected. The opposite effect is evident in figure 5.6 where the phase error decreases with increasing frequency. The reason for this is due to the sensing circuit and the oscilloscope input impedance. The reference voltage probe, with phase error corrected, measures the through line voltage and current phase (both are in phase as the 50 Ω terminator is used) directly beneath the sensing element. The output signals, as discussed above, are 90° out of phase with the through line signals, assuming a purely resistive termination at the oscilloscope. This would be approximately true if the 50 Ω termination option at the oscilloscope was used. In that situation the parallel input capacitance of the scope would be negligible, at least for the frequency range of interest. However for the results presented here the 1 MΩ scope input has been used. The main reason for this is to achieve a larger output signal when working at low power levels. The larger the terminating resistance the larger the measured signal as with any voltage dividing circuit. When using the 1 MΩ input of the scope the input capacitance to ground ($\approx$ 13 pF) becomes important. The termination becomes dominated by the capacitance with increasing frequency, explaining the reduction in phase error.

5.5.2 Signal amplitude scaling

Calibration of the variation in sensed output signals as a function of the through line signals is also necessary. The through line voltage amplitude is determined by the voltage probe, while the through line current is the sensed

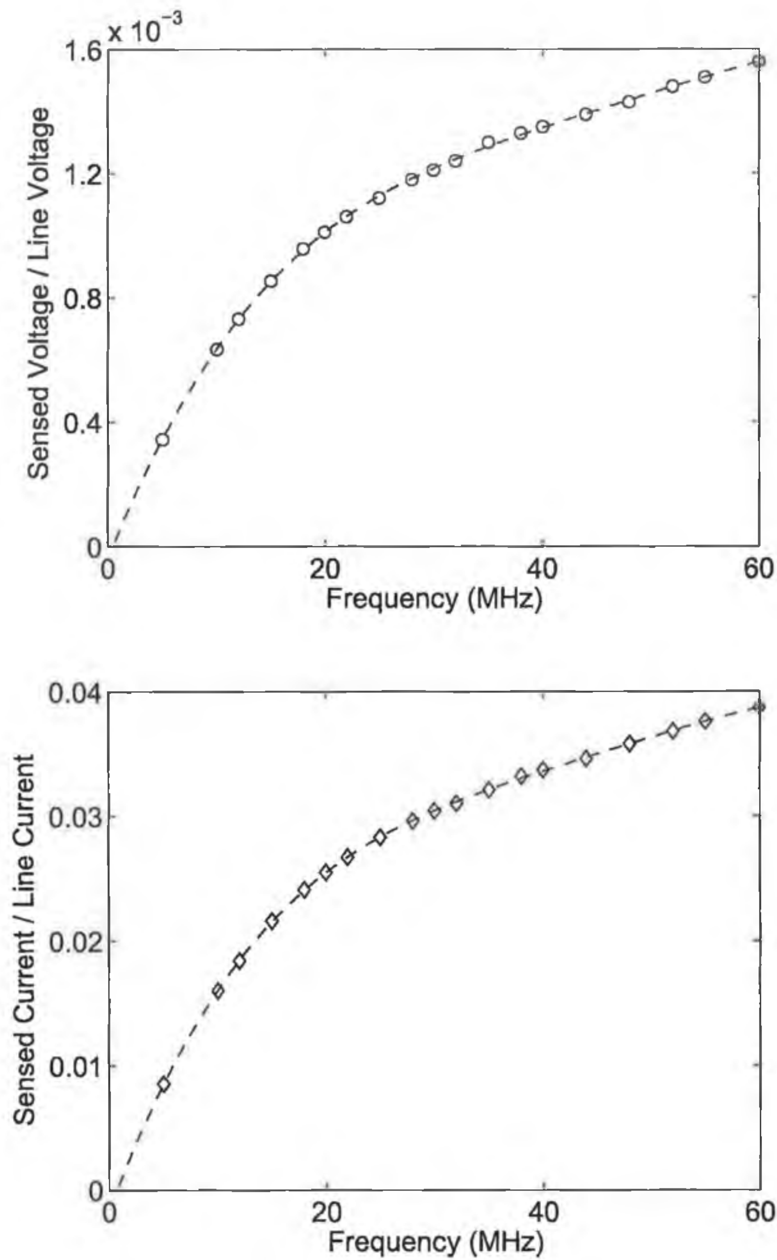

Figure 5.7: *Sensor output signals as a function of frequency. Circles and triangles represent measured data, while dashed lines represent* 4th *polynomial fits to the data.*

voltage divided by 50 Ω. Applying (5.12) and (5.13) to the phase corrected sensor output signals yields two new signals, one proportional the through line voltage and one proportional to the through line current. The amplitude of these calculated signals also vary with frequency. The reason for this is that the impedance of both the capacitive element of the voltage pickup and inductive element of the current pickup vary with frequency. The impedance of the terminating elements also vary with frequency due to the input capacitance of the scope. A plot of the variation of the output voltage and current signals as a function of frequency is shown in figure 5.7. Both data sets are well fitted with a 4th order polynomial equation over the frequency range of interest. As with the phase calibration, the FFT algorithm is used to scale the relevant frequency components to the appropriate amplitude.

5.6 Sensor accuracy

Once the sensor has been calibrated to accurately determine the current, voltage and relative phase the forward and reflected voltage signals can also be determined.

At any point on a transmission line the voltage signal is the sum of the forward and reflected voltages

$$V = V_f + V_r \tag{5.14}$$

and the current is the difference between the forward and reflected currents

$$I = I_f - I_r. \tag{5.15}$$

Following the same derivation described in section 5.2, (5.15) can be written as

$$I = \frac{V_f}{Z_0} - \frac{V_r}{Z_0}. \tag{5.16}$$

Solving (5.14) and (5.16) simultaneously gives the forward and reflected voltages in terms of the local current and voltage on the through line

$$V_f = \frac{V + 50I}{2}, \tag{5.17}$$

$$V_r = \frac{V - 50I}{2}, \tag{5.18}$$

where 50 has been substituted for Z_0 - the characteristic impedance of the sensor through line. This provides an accurate means of calculating directional line signals without the need for electrical circuitry to isolate signals in a particular direction. Directivity and load mismatch issues are therefore eliminated as the accuracy of our directional signals are only dependant on the current, voltage and phase measurements.

A test of the accuracy of the phase calibration of the sensor is performed using a high quality (Q) factor capacitive load at the output end of the sensor. In the $10-20$ MHz range the impedance phase measurements (phase of the voltage relative to the current) reads between -88° and -89°, where the deviation from the ideal (-90°) is more likely caused by the resistance of the capacitor's connecting wires than by error in the phase calibration. At higher frequencies the departure from -90° is more severe as expected.

Measurement errors associated with this type of sensor depend on the accuracy of the devices used in the calibration procedure. Here we have used an oscilloscope/attenuating voltage probe combination with 2% accuracy and a 50 Ω terminator with 1% accuracy. Based on repeated comparisons with the actual through line signals from the voltage probe, we estimate the absolute accuracy of the sensor voltage and current measurements to be $\pm 2\%$. Observation of fluctuations in the phase measurement suggest an accuracy of $\pm 0.2^o$.

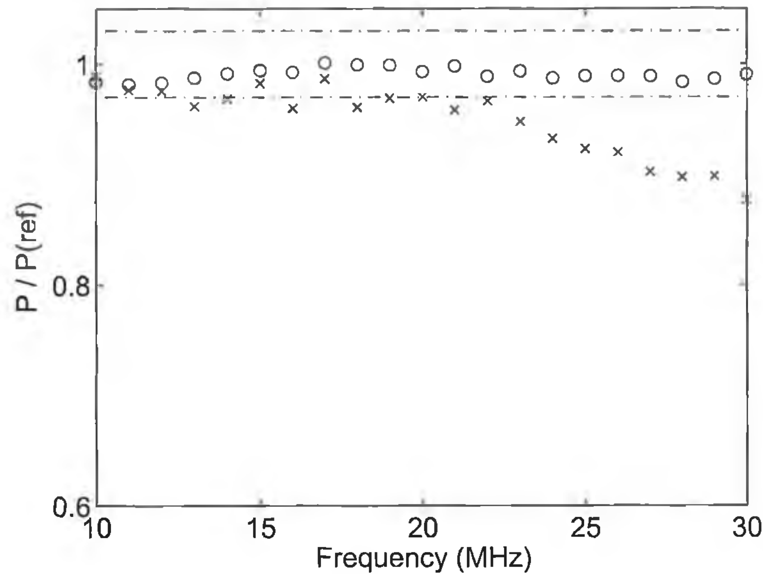

Figure 5.8: *Normalized frequency response of our sensor compared to an industrial standard wattmeter, over the frequency range specified for the wattmeter.*

5.7 Comparison with standard wattmeter

In figure 5.8 a comparison between our rf sensor and an industrial standard wattmeter (Bird Model 43) is made. Power measurements are made into a 50 Ω dummy load using both devices and compared against a more accurate reference power level achieved by measuring the voltage directly across the resistor. The reference level is normalized and the horizontal dashed lines indicate the error bounds. The particular wattmeter sensing element available for testing has a quoted frequency range of 2 – 30 MHz, but a deterioration in accuracy is clearly seen at ≈ 22 MHz. Our sensor lies within the reference level tolerances over this frequency range and up to the calibrated limit of 70 MHz. In figure 5.9 a dummy load termination of 50 Ω is used in parallel with a 376 pF high quality factor capacitor. The load reflection coefficient

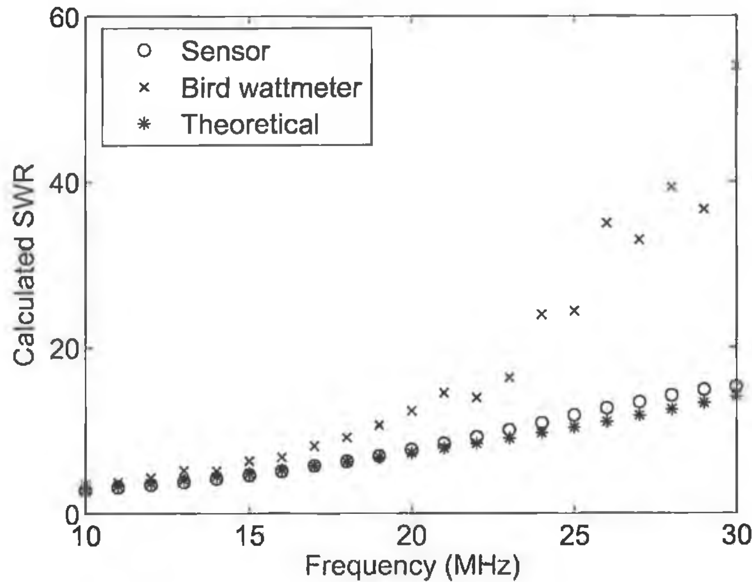

Figure 5.9: *Comparison of load SWR measurements for a fixed dummy load of* 50 Ω *in parallel with a* 376 pF *capacitor for varying frequency*

(Γ) is calculated for the wattmeter using

$$|\Gamma| = \frac{\sqrt{P_r}}{\sqrt{P_f}} \tag{5.19}$$

and for our rf sensor using

$$|\Gamma| = \frac{V_r}{V_f}. \tag{5.20}$$

Subsequently the load standing-wave ratio (SWR) is obtained from

$$SWR = \frac{1+|\Gamma|}{1-|\Gamma|}. \tag{5.21}$$

The theoretical value can also be calculated once the load resistance and reactance is known

$$|\Gamma| = \sqrt{\frac{(R_{load} - Z_0)^2 + X_{load}^2}{(R_{load} + Z_0)^2 + X_{load}^2}} \tag{5.22}$$

Using the fixed load the SWR is varied by varying the frequency in the bandwidth range specified for the wattmeter. The rapid deviation of the wattmeter from the theoretical value above 20 MHz and an SWR of ≈ 10 illustrates the limited accuracy of this devise at higher frequencies and increasing load mismatch.

Our device is close to the theoretical value over the entire range investigated. The deviation at higher frequencies is expected as parasitic impedances associated with the load connections become significant.

5.8 Summary

A rf power sensor has been designed with 50Ω characteristic impedance to measure power dissipated in a plasma load. The sensor design is based on ideas taken from directional coupler theory as well as standard current/voltage probe power measurement techniques. The characteristic impedance is set by the ratio of the diameters of the inner conductor and the outer ground shielding. The sensing element is then mounted in a slot cut into the ground shielding. The sensing element consists of capacitive pickups to sample the rf voltage and inductive loops to sample the rf current.

The accuracy of the sensor is found to be very dependent on accurate measurement of the phase between the current and voltage signals. The complete phase calibration procedure is outlined in detail over the required frequency range. At present the sensor has been calibrated for a frequency range of 10-70 MHz. The entire calibration relies on a wide band high accuracy voltage probe, an accurate 50Ω dummy load and a dummy line to obtain the exact phase at the point in the sensor where the sensing element is located.

The calibrated power sensor is compared with an industrial standard power meter. The industrial meter with a specified bandwidth of 2-30 MHz is found to degrade much lower than the 30 MHz limit for a fixed power level into a 50Ω dummy load whereas our sensor remains within the error limits over the entire range. Finally when the SWR measurements of an unmatched load from both sensors are compared over the same frequency range the limited accuracy of the industrial meter is more apparent. Our sensor on the other hand remains close to the theoretical value over the entire range investigated.

With rf power absorption being an important control parameter for ensuring reproducible plasma conditions, improved measurement accuracy is desirable. The more accurate the measurement the more confident one can be that the processing conditions are close to that of previous runs. Another important feature of this sensor is its ability to measure power at the fundamental frequency and harmonics of the source power. This would be very useful in some discharges where a significant fraction of the absorbed power is known to be contained in the harmonics. At present the rf power measurement accuracy is about 3% and only limited to that by the equipment used in the calibration procedure. In the future, with the use of more accurate equipment, we anticipate improving the accuracy, at both the fundamental and its harmonics, to better than 1%.

CHAPTER 6

Conclusion

In conclusion to this thesis, the main results presented are summarized and where possible some suggestions for further work are made. The motivation behind this work was to extend the understanding of phenomena associated with capacitive rf sheaths and in particular to test aspects of theoretical collisionless electron heating mechanisms. Collisionless heating is important as it is the mechanism that sustains capacitive discharges at low operating pressures. The investigation of the electron heating in the sheath has been performed using a novel experimental technique specifically designed for this task. In addition a novel rf power sensor has been designed to measure power absorbed in plasma discharges. The advantage of this sensor over standard industrial products is that it can be used either pre or post matching unit while retaining its overall accuracy.

6.1 The experimental technique

An experimental technique has been designed to enable an electrical characterization of a capacitive rf sheath in terms of sheath potential, sheath current, and sheath power absorption. In particular this method makes it possible to test collisionless heating mechanisms associated with these capacitive sheaths. This experimental design serves to somewhat replicate the situation simulated by Gozadinos discussed in detail in the previous chapters. That simulation modeled a planar electrode in contact with a semi infinite plasma. This means that at one side of the simulation region lies a infinite bulk plasma and at the other side a perfectly absorbing planar electrode. The advantage of this technique is that the sheath is not directly coupled to the bulk processes since the plasma is not sustained by the electrode. Our experiment serves to replicate this model with a large volume plasma in contact with an approximately planar electrode. The plasma bulk is sustained independently and thus decouples the electrode sheath, which is biased separately, from the bulk processes as in the simulation.

The important features of this experimental design are twofold. Firstly the use of the inductive source to sustain the discharge makes the decoupling of the electrode sheath possible. Therefore sheath conditions can be altered while maintaining the same plasma parameters by changing bias conditions of the electrode. Secondly the use of an external dc bias while rf biasing the electrode makes it possible to control charged particle (electrons in this case) fluxes arriving at the electrode. In particular this has enabled us to investigate the effect of electron conduction current on the rf power absorption in the sheath.

The application of this technique is not limited solely to phenomena discussed in this thesis but could also be used as a plasma diagnostic. The

electrode is basically a planar Langmuir probe designed to be simultaneously dc and rf biased. The fact that this can be used to extract the electron conduction current opens the possibility for a novel plasma diagnostic. The electron conduction current $I_e(t)$ has an exponential dependance on the ratio of the sheath potential $V_s(t)$ to the electron temperature T_e

$$I_e(t) = I_{e0} exp\left[\frac{-V_s(t)}{T_e}\right]. \tag{6.1}$$

Therefore a plot of $V_s(t)$ versus $\ln I_e(t)$ has a slope of T_e. However a more accurate determination of the electron conduction current waveform to those presented here is necessary to get accurate results.

6.2 Collisionless electron power absorption

The main subject of this thesis was to examine electron power absorption in the sheath through so called collisionless heating. An interesting, secondary, prediction of a recent theoretical model is that electron loss to the electrode is significant and should be accounted for in such models. Electrons crossing the sheath to the electrode loose energy which reduces the overall power delivered to the electrons. To accurately measure the power dissipated through the collisionless mechanism alone the electron loss must be accounted for.

In previous attempts to measure the power dissipated through collissionless heating in capacitive discharges electron loss has been ignored. The reasons for this are a) it is generally thought that electron loss is negligible and b) it is very difficult to measure the effect of electron loss under normal circumstances. Here we have developed a method to experimentally observe the effect of electron loss on the total electron power absorption in the sheath.

In chapter 3 we investigate the power coupling to both ions and electrons as a function of increasing negative dc bias starting at the electrode self bias.

One of the key findings is that power coupled to the electrons increases with increasing dc bias. This shows that reducing the electron loss enhances the power absorption. The total rf current signals were compared for two situations 1) at the self bias where electron loss is permitted and 2) at a large negative bias where the electron loss is effectively removed. This comparison highlights that the only significant effect on the current signal is at the electron loss phase of the rf cycle again reinforcing the claim that the removal of electron loss is responsible for the observed increase in power.

In chapter 4 the experimental results are compared with a PIC simulation of the same situation. The PIC results give more insight into the different channels that power can be dissipated. It allows the separation of the electron loss and collisionless heating components of the electron power, reiterating that the increase in electron power is due to the reduction of electron loss. It also enabled a comparison between the various current and voltage components from the experiment and good agreement was found.

The effect of dc bias on the high frequency sheath potential oscillations was determined using an unbiased 50Ω probe mounted close to the sheath region. It was found that their amplitudes decreased with increased bias, and the same trend was obtained from the PIC simulation. The simulation enabled investigation of the claim that the high frequency oscillations in sheath potential enhance the collisionless heating of electrons. It was found that even thought the oscillations were damped considerably by the dc bias the collisionless heating remained constant suggesting that they don't in fact contribute to this phenomenon.

It seems that an experimental verification of the exact mechanism by which collisionless heating occurs is by no means a trivial task. The development of the present technique may be of use in future experiments to do

so. At present it is unclear as to how this verification might be performed.

6.3 Discharge power measurement

Power dissipated in rf discharges is one of the most important measurable parameters to ensure reproducible plasma parameters on a particular processing plasma tool. Our investigation into to the different methods available to measure this quantity lead to the conception of a novel rf power sensor. This sensor is based on ideas from directional coupler theory - forward and reflected voltage signals on a transmission line are calibrated to give forward and reflected power, and from current/voltage/phase measurement theory - current and voltage are measured at the same point and their relative phase is accurately calibrated for known loads.

The main features of our design is that it has 50Ω characteristic impedance so as to be non intrusive when inserted on transmission lines with the same characteristic impedance. The sensing element has been designed to measure the current and voltage at exactly the same point. Previous designs sample the current and voltage at separate points and assume the separation is negligible to the phase calibration. At lower frequencies this is a good approximation, however at higher frequencies it introduces a significant error in the phase calibration. The design and construction of the sensor and the calibration of the current, voltage and phase measurements are presented in chapter 5.

The errors associated with directional couplers based on similar ideas are avoided thus increasing the accuracy of the power measurement. Power measurements taken with this sensor have been compared with a standard directional power meter (using a more accurate reference power measure-

ment). The performance of our sensor is shown to be superior at both higher frequencies and increased load mismatch conditions. Another advantage of this type of design is that it can be mounted at the discharge side of the matching unit and still give accurate results. There and many possibilities to further enhance the accuracy of this design and to reduce the complexity of the calibration procedure presented. The main simplification of the design would be to replace the double sensing strip structure with a single strip. The same information can still be obtained and the asymmetry between sensing strip sizes would be avoided. Increased accuracy in discharge power measurements is very desirable since it would allow better control over processing conditions.

Bibliography

[1] O. A. Popov and V. A. Godyak. Power dissipated in low-pressure radio-frequency discharge plasmas. *J. Appl. Phys.*, 57(1):53–58, January 1985.

[2] V. A. Godyak, R. B. Piejak, and B. M. Alexandrovich. Measurements of electron energy distribution in low pressure rf discharges. *Plasma Sources Sci. Technol.*, 1:36–58, January 1992.

[3] G. Gozadinos. *Collisionless heating and particle dynamics in radio-frequency capacitive plasma sheaths.* PhD thesis, Physical Science, Dublin City University, 2001.

[4] M. A. Lieberman and A. J. Lichtenberg. *Principles of Plasma Discharges and Materials Processing.* Wiley, New York, 1994.

[5] B. Chapman. *Glow Discharge Processes.* Wiley, New York, 1980.

[6] V. A. Godyak. *Soviet Radio Frequency Discharge Research.* Delphic Associates, Inc., Falls Church, VA, 1986.

[7] M. A. Lieberman and V. A. Godyak. From Fermi Acceleration to Collisionless Discharge Heating. *IEEE Trans. Plasma Sci.*, 26(3):955–986, June 1998.

[8] G. Gozadinos, M.M. Turner, and D. Vender. On the pressure heating of electrons by capacitive rf sheaths. *Phys. Rev. Lett.*, 87(13), 2001.

[9] Y. P. Raizer, M. N. Shneider, and N. A. Yatsenko. *Radio-frequency capacitive discharges.* CRC Press, Boca Raton, 1995.

[10] M. A. Lieberman. Analytical solution for capacitive rf sheath. *IEEE Trans. Plasma Sci.*, 16(6):638–644, December 1988.

[11] D. Vender and R. W. Boswell. Electron-sheath interaction in capacitive radio-frequency plasmas. *J. Vac. Sci. Technol. A*, 10(4):1331–1338, Jul/Aug 1992.

[12] V. A. Godyak. Statistical heating of electrons at an oscillating plasma boundary. *Sov. Phys. - Tech. Phys.*, 16(7):1073–1076, January 1972.

[13] V. A. Godyak. Steady-state low-pressure rf discharge. *Sov. J. Plasma Phys.*, 2(1):78–84, 1976.

[14] V. A. Godyak, O. A. Popov, and A. H. Khanna. Effective electron collision frequency in rf discharge. *Sov. J. Plasma Phys.*, 2:560–561, 1976.

[15] E. Fermi. On the Origin of the Cosmic Radiation. *Phys. Rev.*, 75(8): 1169–1174, April 1949.

[16] M. Surendra and D. B. Graves. Electron accoustic waves in capacitively coupled, low-pressure rf glow discharges. *Phys. Rev. Lett.*, 66(11):1469–1472, November 1991.

[17] M. M. Turner. Pressure heating of electrons in capacitively-coupled rf discharges. *Phys. Rev. Lett.*, 75(7):1312–1315, August 1995.

[18] I. D. Kaganovich. Anomalous capacitive sheath with deep radio-frequency electric-field penetration. *Phys. Rev. Lett.*, 89(26), 2002.

[19] V. A. Godyak and O. A. Popov. Experimental study of resonant rf discharge. *Sov. J. Plasma Phys.*, 5:227–221, 1979.

[20] V. A. Godyak, R. B. Piejak, and B. M. Alexandrovich. Electircal Characteristics of Parallel-Plate RF Discharges in Argon. *IEEE Trans. Plasma Sci.*, 19(4):660–676, August 1991.

[21] V. A. Godyak and R. B. Piejak. Abnormally low electron temperature and heating-mode transition in a low-pressure rf discharge at 13.56 MHz. *Phys. Rev. Lett.*, 65(8):996–999, August 1990.

[22] C. K. Birdsall and A. B.Langdon. *Plasma physics via computer simulation.* Adam Hilger, 1991.

[23] M. J. Kushner. Monte-carlo simulation of electron properties in rf parallel plate capacitively coupled discharges. *J. Appl. Phys.*, 54(9):4958–4965, September 1983.

[24] M. Surendra, D.B. Graves, and I.J. Morey. Electron heating in low-pressure rf glow discharges. *Appl. Phys. Lett.*, 56(11):1022–1024, 1990.

[25] M. Surendra and D. B. Graves. Particle simulations of radio-frequency glow discharges. *IEEE Trans. Plasma Sci.*, 19(2):144–157, April 1991.

[26] A. E. Wendt and W. N. G. Hitchon. Electron heating by sheaths in radio frequency discharges. *J. Appl. Phys.*, 71(10):4718–4726, May 1992.

[27] M. Surendra and D. Vender. Collisionless electron heating by radio-frequency plasma sheaths. *Appl. Phys. Lett.*, 65(2):153–155, July 1994.

[28] U. Kortshagen U. Buddemeier and I. Pukropski. On the efficiency of the electron sheath heating in capacitively coupled radio frequency discharges in the weakly collisional regime. *Appl. Phys. Lett.*, 67(2):191–193, 1995.

[29] T. E. Nitschke and D. B. Graves. A comparison of particle in cell and fluid model simulations of low-pressure radio frequency discharges. *J. Appl. Phys.*, 76(10):5646–5660, November 1994.

[30] V. Vahedi, C. K. Birdsall, M. A. Lieberman, G. DiPeso, and T. D. Rognlien. Capacitive RF discharges modelled by particle-in-cell Monte Carlo simulation. II. Comparison with laboratory measurements of electron energy distribution functions. *Plasma Sources Sci. Technol.*, 2:273–278, 1993.

[31] M. Surendra and M. Dalvie. Moment analysis of rf parallel-plate-discharge simulations using the particle-in-cell with monte carlo collisions technique. *Phy. Rev. E*, 48(5):3914–3924, November 1993.

[32] D. Vender and R. W. Boswell. Numerical modeling of low-pressure RF plasmas. *IEEE Trans. Plasma Sci.*, 18(4):725–732, August 1990.

[33] M. Surendra. Radiofrequency discharge benchmark model comparison. *Plasma Sources Sci. Technol.*, 4:56–73, 1995.

[34] M. Surendra. *Numerical Simulations of Glow Discharges.* PhD thesis, Chemical Engineering, University of California, Berkeley, 1991.

[35] F. Sobéron. *Plasma Transport and Development of Plasma Kinetics in ARIS.* PhD thesis, Physical Science, Dublin City University, 2005.

[36] P. J. Hargis, K. E. Greenberg, P. A. Miller, J. B. Gerardo, J. R. Torczynski, M. E. Riley, G. A. Hebner, J. R. Roberts, J. K. Olthoff, J. R. Whetstone, R. J. Van Brunt, M. A. Sobolewski, H. M. Anderson, M. P. Splichal, J. L. Mock, P. Bletzinger, A. Garscadden, R. A. Gottcho, G. Selweyn, M. Dalvie, J. E. Heidenreich, J. W. Butterbaugh, M. L. Blake, M. L. Passow, J. Pender, A. Lujan, M. E. Elta, D. B. Graves, H. H. Sawin, M. J. Kushner, J. T. Verdeyen, R. Horwath, and T. R. Turner. The gaseous electronics conference radio-frequency reference cell: A defined parallel-plate radio-frequency system for experimental and theoretical studies of plasma-processing discharges. *Rev. Sci. Instrum.*, 65:140–154, 1994.

[37] M. A. Sobolewski. Electrical characterization of radio-frequency discharges in the gaseous electronics conference reference cell. *J. Vac. Sci. Technol. A*, 10(6):3550–3562, 1992.

[38] M. A. Sobolewski. Electrical characteristics of argon radio frequency glow discharges in an assymetric cell. *IEEE Trans. Plasma Sci.*, 23(6): 1006–1022, December 1995.

[39] N. Spiliopoulos, D. Mataras, and D. E. Rapakoulias. Power dissipation and impedance measurements in radio-frequency discharges. *J. Vac. Sci. Technol. A*, 14(5):2757–2765, 1996.

[40] C. M. O. Mahony, P. D. Maguire, and W. G. Graham. Electrical characterization of radio frequency discharges. *Plasma Sources Sci. Technol.*, 14:S60–S67, May 2005.

[41] F. F. Chen. Electric probes. In R.H. Huddlestone and S. L. Leonard, editors, *Plasma Diagnostic Techniques*, volume 21 of *Pure and Applied physics*. Academic Press, New York, 1965.

[42] V. A. Godyak and R. B. Piejak. Probe measurements of the space potential in a radio frequency discharge. *J. Appl. Phys.*, 68(7):3157-3162, October 1990.

[43] A. J. Lichtenberg and M. A. Lieberman. *Regular and Chaotic Dynamics*. Springer-Verlag, New York, 1992.

[44] G. M. Zaslavskii and B. V. Chirikov. Mechanism for fermi acceleration in a one-dimensional case. *Sov. Phys. Dokl.*, 9(11):989–992, July 1965.

[45] M. A. Lieberman and A. J. Lichtenberg. Stochastic and adiabatic behavior of particles accelerated by periodic forces. *Phy. Rev. A*, 5:1852–1866, 1972.

[46] A. J. Lichtenberg, M. A. Lieberman, and R. H. Cohen. Fermi acceleration revisited. *Physica*, 1D:291–305, 1980.

[47] A. J. Lichtenberg. Application of mapping dynamics to analysis of a capacitive rf discharge. In Uwe Kortshagen and Lev D. Tsendin, editors, *Electron Kinetics and Applications of Glow Discharges*, volume 367 of *NATO ASI Series B*, pages 227–240. Plenum Press, New York, 1998.

[48] M. A. Lieberman. The dynamics of fermi acceleration. In Uwe Kortshagen and Lev D. Tsendin, editors, *Electron Kinetics and Applications of Glow Discharges*, volume 367 of *NATO ASI Series B*, pages 215–226. Plenum Press, New York, 1998.

[49] D. Gabor, E. A. Ash, and D. Dracott. Langmuir paradox. *Nature*, 176 (4489):916–919, 1955.

[50] J. Pavkovich and G. S. Kino. R.F. theory of the plasma sheath. In *Proceedings of the VIth International Conference on Ionization Phenomena in Gases*, page 39, 1964.

[51] A. I. Akhiezer and A.S. Bakai. Stochastic plasma heating by rf fields. *Sov. J. Plasma Phys.*, 2(4):359–361, July-August 1976.

[52] C. G. Goedde, A. J. Lichtenberg, and M. A. Lieberman. Self-consistent stochastic electron heating in radio frequency discharges. *J. Appl. Phys.*, 64(9):4375–4383, November 1988.

[53] G. Gozadinos, D. Vender, M.M. Turner, and M.A. Lieberman. Collisionless electron heating by capacitive radio-frequency plasma sheaths. *Plasma Sources Sci. Technol.*, 10:117–124, 2001.

[54] M. M. Turner. Collisionless heating in capacitively-coupled radio frequency discharges. In Uwe Kortshagen and Lev D. Tsendin, editors, *Electron Kinetics and Applications of Glow Discharges*, volume 367 of *NATO ASI Series B*, pages 313–328. Plenum Press, New York, 1998.

[55] P. A. Miller and M. E. Riley. Dynamics of collisionless rf plasma sheaths. *J. Appl. Phys.*, 82(8):3689, October 1997.

[56] J. R. Woodworth, I. C. Abraham, M. E. Riley, P. A. Miller, T. W. Hamilton, B. P. Aragon, R. J. Schull, and C. G. Wilson. Ion energy distributions at rf-biased wafer surfaces. *J. Vac. Sci. Technol. A*, 20(3): 873, May 2002.

[57] M. A. Sobolewski, J. K. Olthoff, and Y. Wang. Ion energy distributions and sheath voltages in a radio-frequency-biased, inductively coupled, high-density plasma reactor. *J. Appl. Phys.*, 85(8):3966, April 1999.

[58] M. A. Sobolewski. Experimental test of models of high-plasma-density, radio-frequency sheaths. *Phy. Rev. E*, 59(1):1059, January 1999.

[59] K. Kohler, J. W. Coburn, D. E. Horne, and E. Kay. Plasma potentials of 13.56-mhz rf argon glow discharges in a planar system. *J. Appl. Phys.*, 57(1):59–66, January 1985.

[60] M. A. Sobolewski. Experimental test of models of radio-frequency plasma sheaths. *Appl. Phys. Lett.*, 70(8):1049, February 1997.

[61] V. A. Godyak, R. B. Piejak, and B. M. Alexandrovich. Ion flux and ion power losses at the electrode sheaths in a symmetrical rf discharge. *J. Appl. Phys.*, 69(6):3455, March 1991.

[62] B. P. Wood, M. A. Lieberman, and A. J. Lichtenberg. Sheath motion in a capacitively coupled radio frequency discharge. *IEEE Trans. Plasma Sci.*, 19(4):619–627, August 1991.

[63] Hyun Chul Kim, Oleg Manuilenko, and Jae Koo Lee. Particle-in-cell monte-carlo simulation of capacitive rf discharges: Comparison with experimental data. *Jpn. J. Appl. Phys.*, 44(4A):1957–1958, 2005.

[64] C. K. Birdsall. Particle-in-cell charged-particle simulations, plus monte carlo collisions with neutral atoms, pic-mcc. *IEEE Trans. Plasma Sci.*, 19(2):65–85, 1991.

[65] D. Gahan and M. B. Hopkins. Collisionless electron power absorption in capacitive radio-frequency plasma sheaths, submitted for publication.

[66] Anritsu Company. Application note: Reflectometer measurements - revisited. Technical report, 2004.

[67] V. A. Godyak and R. B. Piejak. In situ simultaneous radio frequency discharge power measurements. *J. Vac. Sci. Technol. A*, 8(5):3833–3837, 1990.

[68] V. A. Godyak, R. B. Piejak, and B. M. Alexandrovich. Experimental setup and electrical characterization of an inductively coupled plasma. *J. Appl. Phys.*, 85(2):703–712, January 1999.

[69] V. A. Godyak, R. B. Piejak, and B. M. Alexandrovich. An experimental system for symmetric capacitive rf discharge studies. *Rev. Sci. Instrum.*, 61(6):2401–2406, 1990.

[70] Bird Electronics Corporation. Catalog gc-92. Technical report, 1992.

[71] D. Gahan and M. B. Hopkins. In-line sensor for accurate rf power measurements. *Rev. Sci. Instrum.*, 76, 2005.